MASTERARBEIT / MASTER'S THESIS

Titel der Masterarbeit / Title of the Master's Thesis

„RESPONSE OF TILT AND GRAVITY ON ENVIRONMENTAL PROCESSES AT CONRAD OBSERVATORY, AUSTRIA"

verfasst von / submitted by

Serafeia Mangou

angestrebter akademischer Grad / in partial fulfilment of the requirements for the degree of

Master of Science (MSc)

Wien, 2019 / Vienna, 2019

Studienkennzahl lt. Studienblatt / degree programme code as it appears on the student record sheet:	A 066 680
Studienrichtung lt. Studienblatt / degree programme as it appears on the student record sheet:	Joint-Masterstudium Physics of the Earth (Geophysics)
Betreut von / Supervisor:	Univ.-Prof. Dr. Bruno Meurers

I hereby declare I wrote this thesis by myself, only with the help of referenced literature, under the careful supervision of my thesis supervisor.

…………………………

Serafeia Mangou

ACKNOWLEDGMENT

First of all I would like to thank my supervisor, prof. Bruno Meurers, for his valuable help and advice, the interesting discussions we had during our research and on general his support, belief on me and guidance during my thesis. Secondly, I would like to thank also Mr. Gabor Papp for his suggestions, his detailed instructions about the instruments and about processing scheme of the data.

Furthermore, I would like to thank my friend and physicist, Ioannis, for his big help, his love and support on finishing my thesis. Finally, a big 'thank you' to all my friends and of course my family for encouraging me not to give-up and follow through the whole master program.

Table of Contents

1. Introduction

1.1 History of the recent scientific geodynamic research

For many years until today geophysicists make measurements in underground observatories worldwide, in order to observe the tilting of the Earth's surface which is caused by the Earth and ocean tides. The instruments which are mostly underground installed, for avoiding the influence of temperature variations, are tilt meters and strain meters designed to measure the deformation of the Earth. Most geodynamic observatories, worldwide, are also dedicated to studies of temporal deformations of the earth's crust and variations of the gravity field. The Earth is changing with time periodically due to the tides. The tidal acceleration is the resultant of the gravitational acceleration of an extraterrestrial body (Sun, Moon or other celestial bodies), and the centrifugal acceleration due to the motion around the common center of mass. The earth itself does not behave as a rigid body but deforms globally due to these tidal forces and these phenomena are called Earth Tides. Except for the Earth tides, the deformation of the Earth is mainly strongly associated with mass transports caused by hydrological disturbances such us precipitation, soil moisture variations, water flow in aquifers, and snow cover. Gravity signals can again detect these mass transports which change the mass distribution around the Earth.

Observations of the gravity field of the Earth are thus carried out, in order to obtain a better understanding of the dynamics of the Earth. The instruments used are the gravimeters, responsible for measuring temporal changes in the vertical component of the Earth's gravity field. The most accurate gravimeters until now are the Superconducting gravimeters (SG) for long-term stationary continuous observations. The gravity measurements are affected by environmental influences, not only hydrological influences, by the water mass transport but also atmospheric influences. Many investigations about the water transport and contribution of the local and global hydrology have been performed in many hydrological studies worldwide and also in observatories like the geodynamic observatory in Moxa, Germany [1], in the Strasbourg observatory [2], in the geodetic observatory in Wettzell, Germany [3] etc. In all studies the results have shown that although gravity measurements are difficult to interpret, they can provide us data for further hydrological research and can help us to improve the understanding of hydrological processes occurring in the vicinity of the observatories. In many studies it was also revealed, that there is accumulation of water below the base plate of the observatory building and that leads the geophysicists to a possible scenario known as the 'base plate model'. For example in the geodetic

observatory in Wettzell (Germany) the water underground followed also my soil moisture and snow storage changes contribute to the gravity signal and maybe can support this scenario [4].

Information about the geodynamical processes on Earth are obtained not only from gravimeters measuring the gravity variations but also from instruments like tiltmeters and which measure tilt variations of the Earth. Strain and tilt measurements have been performed in the last few decades throughout the world and the deformation of the Earth's crust has been studied in many tectonically active parts of the Earth. Studies performed in many seismically active areas reveal, that the hydrologic induced signals have similar signatures as pre- and post-seismic signals and that is one of the main problems in the deformation studies which aim to the study and detection of tectonic movements [5]. There are many examples studied in the past describing the subsurface deformation induced by the rainfall and the atmospheric pressure and reporting the pre-, co- and post-seismic deformation in different areas of the world. One of them is the Friuli (NE-Italy) seismic area, where tilt and strain measurements are performed in a cave at a depth of 60 meters [6]. The results showed that the barometrical deformation gave evidence on the existence of weak structures connected probably with the fault tectonic system of the Alps and that some of the hydrologically induced deformation can be attributed to rock discontinuities affected by the water variations. Measurements of crustal deformation have also been performed since 2003 in the United States in the Plate Boundary Observatory (PBO) [7], where long base strain and tilt meters were used in order to understand the deformation processes of the Earth. Two low drift tiltmeters were also installed in Vosges Mountains to study the hydrological loading [8] where results confirmed that hydrological models can provide a good estimation of water stock variations and also give us more information for stored water modelling. More recently, observation of the Earth tides and studies of the local tectonic processes starts to be in progress in the Vyhne Slovak Tidal station where data since 2001 are collected and analyzed [9]. After analysis of the data, received by extensometers, it was revealed that the anomalies in the deformations were due to the high heat flows in the vicinity of the Vyhne station, due to the surface extension. The rocks are deforming in the surrounding of the observatory due to the variation of temperature and air-pressure and these variations influence the instruments. Since November 2005 an ASKANIA-type tiltmeter of high resolution is recording near a fault zone in Mizunami of Japan [10]. The experiment reveals that the tilt signals are caused by pore pressure induced

deformation but in order to reveal more the hydrological processes of the fracture system, a finite element method in addition is for sure needed.

It is well known, that the presence of a cavity in a medium affects the stress and strain in its surroundings [11]. A spherical tunnel can be deformed by horizontal strain and then tiltmeters can record these anomalous tilts due to this deformation, as it was first realized by King and Bilham [12]. "So, there is in general a strain-induced tilt inside the cavity which varies rapidly from place to place, not typical of the surrounding rock" [11]. This is called the "cavity effect". One of the reasons that can possibly explain why there are many inconsistencies in tidal tilt observations, is the cavities and surface inhomogeneities. The latter distort all the true strains and tilts produced by stresses in the Earth and hence, the observed data deviate from the theoretical data of the calculated simple Earth models, like the DDW-H, DDW-NHi, and WDZ models [13]. The anomalous ξ factors, derived from tidal data analysis, can give us a clear hint of the cavity effect. Finite element modelling techniques have been employed to solve the problem of the cavity effect, as it was first reported by Harrison (1976) and Itsueli et al. (1975) using the first-order approximation (FEM) [14]. Such techniques have been applied in many cases where underground inhomogeneities are so intense and helped to interpret complex geophysical phenomena occurring in many areas of the Earth [15]. Brimich and Hvozdara (1997) used the boundary element method in order to determine also this effect [16].

Measurements with long-baseline tiltmeters have brought as well new information on water storage dynamics in karst systems [17]. 'Karst systems or else epi-karstic systems are complex hydrological systems due to their structural heterogeneity' [17]. The deformation which is induced by the water pressure after some precipitation changes the fractures and is responsible for the observed tilt. It is the infiltration of water which modifies the pore-pressure and induces the deformation of the medium. The Fontaine de Vaucluse in France is one of the most famous karst systems. The area has been a lot of times under research, and tiltmeters were installed to study the local dynamics of the water infiltration of the system [18]. The studies try to explain the field deformation and search for complementary information that can further constrain the geometry of deformation of the medium. The results showed that that there is a significant correlation with the hydrological observations and a few only meters of water are sufficient to provoke the observed deformation. Estimation of the epi-karstic water storage has also been performed recently by applying gravity measurements at different depths on three karst systems in southern France [19]. The general outcome of this study

was that gravity observations have to be better combined with other geophysical methods for a more accurate evaluation of the water underground storage. Water infiltration and recharge processes in karst systems are complex and thus sometimes is difficult to study them using conventional hydrological methods. Imaging the groundwater infiltration dynamics through long term-ERT monitoring (Electrical Resistivity Tomography) is one of the new methods which gives more insight into a karst landscape and improves strongly the karst hydrological knowledge. The strength of this method results from its ability to track changes in the electrical properties of the subsurface indicating thus variations in the temperature, moisture and chemical properties [20]. The first studies performed by ERT monitoring were able to differentiate three distinct layers in the karst vadose zone with different resistivity variations and these results confirm the previous knowledge of hydrological processes occurring in the karst environments [21], [22]. Geoelectrical (ERT) resistivity measurements of hydrological processes have also been performed in the Moxa geodynamical observatory (Germany) to study the temporal deformations of the Earth's crust [23]. Results indicate that the variations in resistivity of the soil moisture are related with subsurface flow induced by water from rain and snow-melt events.

Other modern methods used recently, like GPS measurements can give insight as well in the study of hydrologically induced karst deformation [24]. After this study in the eastern Southern Alps and northern Dinarides, it was concluded that the ground displacement in both vertical and horizontal component was driven by changes of surface hydrological loads and that there was a high correlation with the cumulated precipitation. In the future, studies are going to include more GPS stations for the more accurate measurements of deformation signals and, therefore, for the progress of more precise hydrological models.

One other example, showing a very good correlation between hydrology and tilts observed for deep aquifers is the study case of the Plateau de Calern in Alpes, near France [25]. Two long baseline tiltmeters were installed in the geodetic observatory, OCA, to study the deformation of the area and the measurements revealed a really significant correlation between the precipitation and the variations of the tilts. The exact mechanism of the karst system is still unknown and more information has to be brought by using finite-element modelling.

Finishing this historical retrospection to the geophysics' past, we become aware of the fact that many techniques and methods have been exposed in order to solve the problem of identifying and modelling the hydrological effects based on deformation and gravity

observations. In the paragraphs following, I proceed to my own study of research. I focus to the recent geophysical research performed in Vienna in Austria and I describe the outline and goals of this thesis.

1.2 The Conrad Observatory, Austria

Observations and analysis of global geodynamical signals are also performed in Vienna of Austria in the Conrad Observatory (Fig. 1.1).

Figure 1.1. Entrance of the Conrad Observatory [26].

This observatory is located on top of the Trafelberg, next to Muggendorf, approximately 45 km southwest of Vienna, in Lower Austria [27]. It is a geophysical research facility of the Central Institute for Meteorology and Geodynamics (ZAMG) and its task is monitoring continuously meteorological, seismic, gravimetric and geomagnetic data [26]. The observatory is located almost underground consisting of a seismic-gravimetric tunnel, 145m length, and a magnetic tunnel-system with length bigger than 1 km (Fig. 1.2). In the observatory there is a superconducting gravimeter (SG), the GWR C025, established in November 2017, which measures variations of the Earth's gravitational field caused by the tides and other geodynamic processes.

Since two years a project started in Hungary aiming to detect the pre- and post-seismic motion along the Mur-Mürz tectonic fault system, which probably exists between Hungary and Vienna (Papp, Meurers, Benedek, Leonhardt, Ruotsalainen, pers. Comm.). For this reason two tilt meters were installed in the Conrad observatory to monitor changes in tilt continuously. Inside the tunnel (Fig.1.3), these two tiltmeters are located 100m apart from the gravimeter - a 5.5m long interferometric hydrostatic tiltmeter, iWT, built by the Finnish Geodetic Institute (FGI) and a Lippmann- type 2D

(pendulum) tiltmeter, LTS. The iWT measures East-West tilts and the LTS both East-West and North-South tilts. The iWT was installed in 2014 and the LTS in 2015 and since spring 2016 they monitor continuously.

Figure 1.2. Magnetic tunnel in Conrad Observatory [28]

As it will be discussed in more detail later, the hydrological signals observed from our sensors around the area of the Conrad Observatory are so intense and thus, they have to be isolated and removed in order to 'catch' clearly the true signals of deformation due to the fault. If it is going to be accomplished, then the results of this study maybe can be used to remove the time dependent hydrological signals enhancing thus possible geodynamic signals. Meteorological sensors as well are installed in Conrad Observatory aiming to precipitation estimates in high temporal resolution.
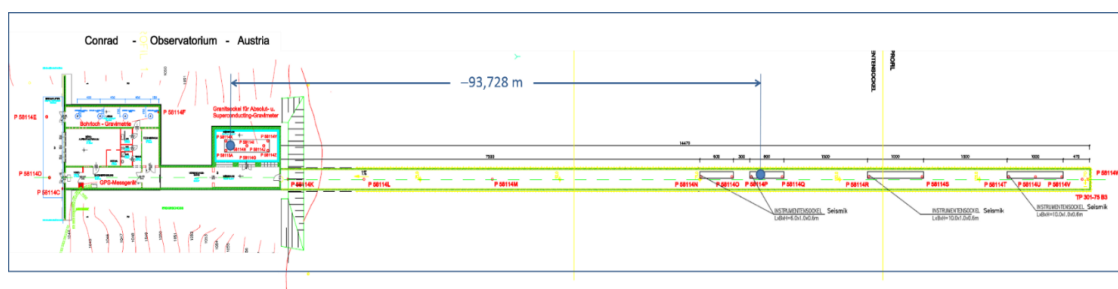

Figure 1.3. Plot of the Conrad Observatory (Meurers pers. Comm)

1.3 Geological structure of Trafelberg and Tectonics

The Trafelberg is located at the northern limestone Alps. It is supposed that the area is hydrologically characterized by epi-karstic phenomena [29], because there are no creeks or springs on the Trafelberg Mountain itself. The topography image of Trafelberg derived from Airborne Laser Scanner (ALS) data (Fig. 1.4) shows at least

on larger sinkhole. Under the 'eye' of the ALS, geophysicists are able to scan the topography around Trafelberg and it is obvious, that there are some clear structures associated with sediments filled with basins around the Conrad Observatory [29].
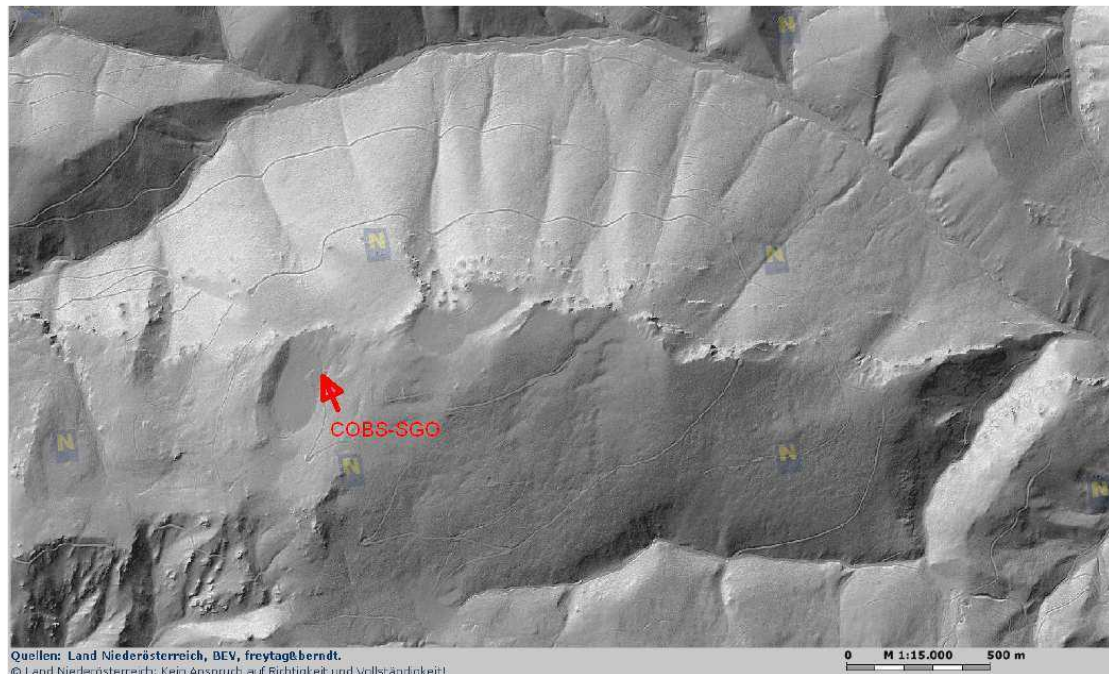

Figure 1.4. Laser scan plot of Trafelberg under the 'eye' of the ALS. The red arrow shows the location of the Conrad observatory [29]

1.4 Instrumentation at Conrad Observatory

1.4.1 The Superconducting Gravimeter (SG)

As it is already mentioned before, the Superconducting Gravimeter, SG, is a very good tool for investigating temporal gravity variations caused by geophysical processes such as the earth tides. It observes continuously very small changes in gravity acceleration with high accuracy and longtime stability (Fig. 1.5). It is an ideal instrument for high precise observation of signals in a wide frequency band, including the long-period component [30]. The instrument consists of a superconducting coil system (liquid Helium), a sensor mass and the measurement and control device. The function of the instrument, generally, is based on a constant magnetic field, produced by two vertical superconducting coils which cause electrical currents and the sphere is displaced by variations on gravity. For example, some relative motion between the ground and the sphere can move the sphere from its equilibrium position. Temporal gravity changes

11

cause vertical sphere displacement and consequently an AC signal at the center ring plate.

Figure 1.5. GWR SG CT-025 and Scintrex CG-5 at the Conrad Observatory [31]

1.4.2 The Lippmann Tiltmeter Sensor (LTS)

The Lippmann Tiltmeter Sensor (LTS) is designed to measure very small changes with respect to the most stable reference, means the vertical gravity vector. These instruments have a vertical reference which points along the direction of gravity, so they also measure the horizontal acceleration. In an external frame (the vertical axis defined by the gravity vector) one measures tilts *around* the Y axis, or equivalently, *along* the X axis. In the Conrad observatory the instrument is adjusted to monitor in the following directions: Positive tilt in X = tilt to East and Positive tilt in Y = tilt to South (Fig.1.6).
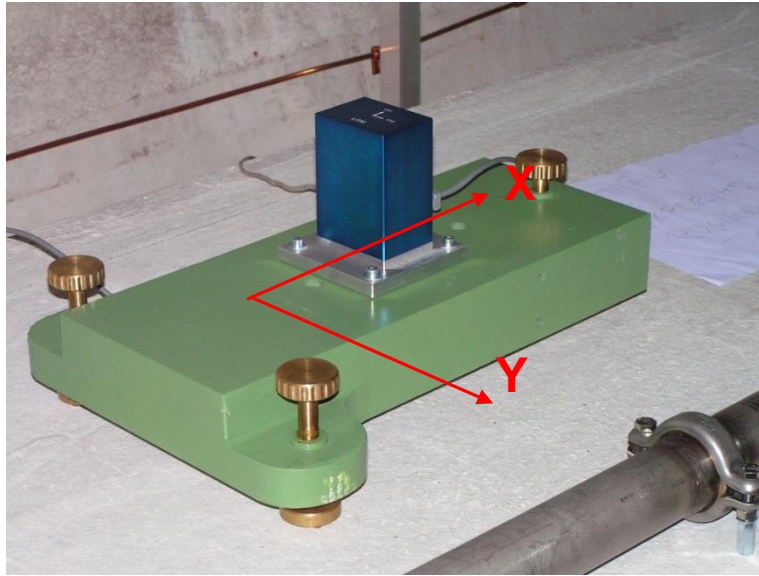
Figure 1.6. The LTS at the Conrad Observatory

1.4.3 The Interferometric Water (hydrostatic) Tiltmeter (iWT)

The Interferometric Water level Tiltmeter (iWT) has been in operation at the seismological tunnel of Conrad observatory since 2014 (Fig. 1.7).
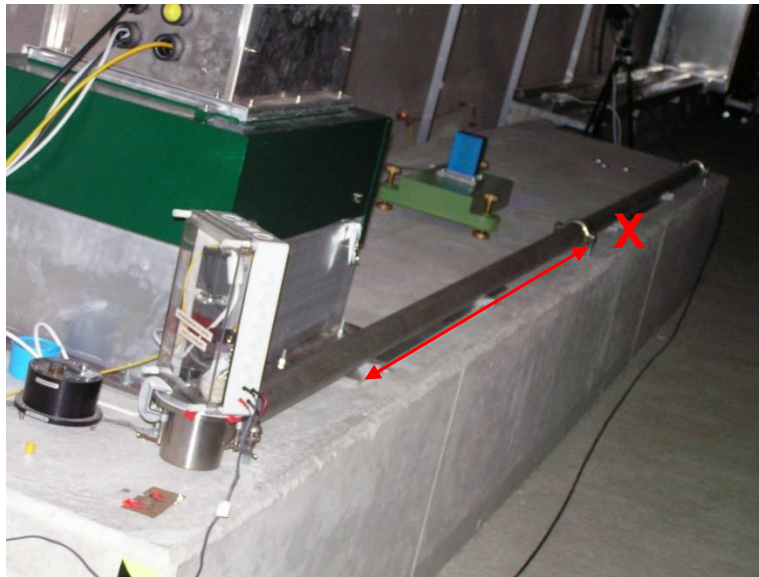

Figure 1.7. The iWT sensor at the Conrad Observatory

The instrument records a broad band of geophysical tilt signals with 15 Hz sampling rate, means, microseisms, free oscillation of the Earth surface, Earth tide tilt, ocean loading, atmospheric loading and secular land tilting [32]. The iWT can be applied in various kinds of geodynamic and geophysical research. It has absolute scale and is able to do high precision tilt measurements. It is a Fizeau-type interferometer with a tube length of 5.5 meters. It was built by the Finnish Geodetic Institute and bought by the

13

geodetic and Geophysical Institute of the MTA CSFK, Hungary. It consists of a He-Ne Laser with fiber optics, a convex plane lens and a digital camera, the images of which can be accessed through a remote fiber-optic fire-wire connection by a computer [33]. In the Conrad observatory the instrument is adjusted to monitor the x-tilt component (East-West direction), so such in the case of the LTS, the tilt is positive towards East.

1.5 Meteorological sensors

1.5.1 The Laser Precipitation Monitor

The Laser Precipitation Monitor serves as measuring value transmitter, and is well-suited for the measurement and detection of different types of precipitation, such as drizzle, rain, hail, snow, and mixed precipitation [34]. The principle operation of this sensor is based on a laser optical beaming source, which produces a non-visible parallel beam (λ=785nm), as it is shown in the following figure (Fig. 1.8).
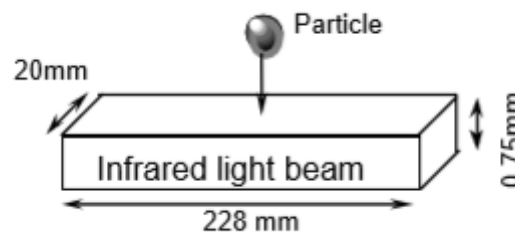

Figure 1.8. Operation of the Laser Precipitation Monitor [34]

The optical intensity measured by a lens, is transformed into an electrical signal, and the signal is reduced when a precipitation particle fall through the light-beam. The diameter and the vertical speed of the precipitation particle is derived from the amplitude reduction and the duration of the signal respectively. Given the diameter and the velocity of the particle, the intensity, quantity and type of precipitation are determined (drizzle, rain, soft hail, snow etc.) as well as the mixed precipitation [34]. In order to improve the identification of the type, also the temperature and humidity are included.

1.5.2 The rain gauge PAAR-AP23 sensor

The rain gauge PAAR-AP23 sensor monitors the amount of precipitation. The way they operate is 'getting' the falling rain in a funnel-shaped collector, which is attached to a measuring tube. The collection area is 500 cm^2. The receiving funnel leads to one of two small buckets with resolution 0.1 mm (amount of precipitation for one tip of bucket). The liquid finally goes to the outer shell of the gauge triggering the second

bucket to take its place and the process is repeating itself [35]. The range of measure is 0 to 720mm per hour.

1.6 Outline of this thesis

Zooming in my case study, in the Conrad observatory of Vienna, the observation of particular residual signatures through the operation of the SG sensor which has recently started, is analyzed. After the installation of the tiltmeters in the Conrad observatory, the observed tilt signatures are related and compared to the signatures of the SG sensor. In this thesis it is evaluated which particular methods, already analyzed and described in the introduction, can or cannot be applied in the frame of this thesis, based on the already known fact, that the data are based only on observations from two tilt meters, LTS and iWT and one gravimeter, the SG. No other geophysical methods like GPS measurements, ERT monitoring or numerical (Finite Element Modelling) are adopted. In the second chapter I describe the way the final gravity and tilt residuals are retrieved and the editing process of the annual data sample is outlined. The comparison between these residuals is discussed in the third chapter and it is examined if the tilt signals correlate with the gravity signals. In this chapter I proceed to my main research by comparing the tilt residuals with the atmospheric and hydrological processes. In the first part I search for variations in the air-pressure and try to find the air-pressure admittance factor, dependent on the frequency. The air-pressure effect is found, means how barometric variations influence the tilt and correlations between the air-pressure and tilt residuals are performed. In the second part the tilt and gravity residuals from both the tiltmeters are compared and the superconducting gravimeter with the precipitation and try to find some reasonable explanation about the behavior of the signals and the physics behind. The precipitation data, from the meteorological sensors, are analyzed and search follows if there is any correlation between the rain and snow events and the tilt and gravity residuals. After quantifying the data and furthermore making the correlation analysis between the signals, I try to make some speculations about the 'nature' which is hidden behind and there is an attempt to create some scenarios about the possible sources that could be responsible for the tilt residual drops. The cavity scenario, as a possible scenario, is in detail examined. In the conclusion, after the cautious observation and analysis of signatures derived from all these three sensors, all possible scenarios for interpretation of gravity and tilt signals are re-evaluated. Concluding, my study focuses on the investigation of the geological area of Trafelberg aiming to find the 'true' scenario which describes the underground hydrological mass transport.

2. Data Processing

2.1 Gravity data processing

Before starting the analysis of the data it is necessary to describe the editing process, performed in order to obtain the final gravity residuals. Data from the SG sensor, in the range from 29.04.2016 until 01.08.2017, are obtained. The processing scheme for the gravity raw time-series follows as it was done by B. Meurers (Meurers pers. Comm.):

1) Filtering and decimation of the original 1 sec. data to 1 min. data by applying the Chebyshev filter G1S1M [36]

2) Degapping and despiking of the 1 min. data and correcting for offset (Correction of the 1 min. data from steps and spikes, which means disturbances from earthquakes and other kinds of noise). Here, big disturbances from earthquakes were removed and also corrections for two known steps were made, caused by a power supply interruption and also the exchange of the gravity card. [37]

3) Decimation of the 1 min. data to 1 hour data by applying the filter G1M1H [36].

4) Analysis of the 1 hour data by the ETEERNA - 3.40 software package [38] and formation of a tidal model for the diurnals semi- and ter-diurnals.

5) Prediction of tides based on the model derived (D, SD, TD and higher frequencies) and subtraction from the observed gravity.

6) Removal of the air-pressure effect applying the Atmacs [39] correction [40]

7) Additional removal of the polar motion effect using the International Earth Reference System- IERS [41]

2.2 Tilt data processing

A similar editing process scheme is performed for the tilt measurements. The same data (from 29.04.2016 until 01.08.2017) are obtained from the two tilt sensors, the LTS and iWT. In total there are three time-series: the East-West component (x-tilt) of the iWT and both East-West and North-South components (x-tilt and y-tilt, respectively) of the LTS. Here is a short description of the pre-processing scheme of the raw tilt data (LTS: 1 Hz, iWT: 15Hz) as it was made by Papp and Meurers (Papp, Meurers pers. Comm.)

1) Decimation of 15 Hz iWT data into a 5Hz time series. Linear interpolation was made of the 15 Hz data on a 5 Hz time frame converting native recording format to TSOFT TSF format [42]. Therefore, a slight smoothing was obtained with a fast algorithm (Papp pers. Comm.)

2) Filtering and decimation to 1 min. data: Decimation of 5 Hz iWT data to 1 Hz data using a Gaussian 1 min long operator containing 61 coefficients and decimation of 1 Hz iWT and LTS data to 1 min data using g1s1md filter coefficients (Papp pers. Comm.)

3) Correction of steps, mainly for iWT data, by using the TSOFT software. The iWT sometimes suffers from cycle-slip. So the correct interpretation of the interference image fails if the phase change between two consecutive samples are larger than the wavelength of the laser light (λ~508 nm). Something like that may occur during large earthquakes.

4) Corrections had to be applied to the data in order to remove first the spikes (which occur mainly due to the earthquakes), and secondly the steps. After removing noisy data, interpolation is performed again in order to reconnect all created gaps and obtain again a continuous time-series. The next figure (Fig. 2.1) presents a part of the x-tilt residual of the LTS which displays the noisy nature of the data. By using TSOFT all the spikes were removed, as it is depicted in the second panel of the figure 2.1.
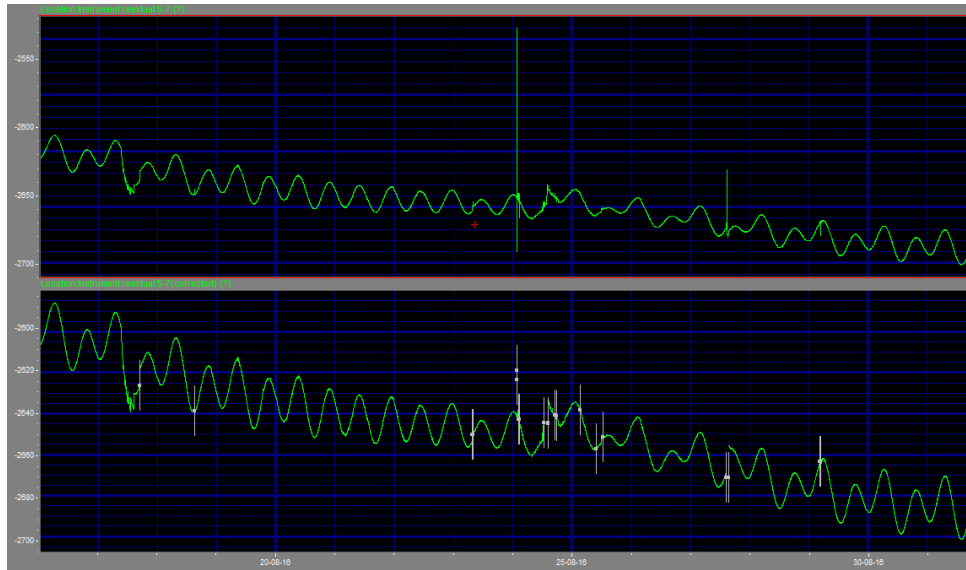

Figure 2.1. TSOFT Correction of steps in the x-tilt residual. First panel shows a part of the noise existed in the x-tilt residual. Second panel is the same after subtraction of the noise through creation of gaps.

Gaps are created in the places where spikes existed and then linear interpolation was made to retrieve the residuals. The x-tilt residuals were much noisier than the y-tilt residual. In addition, thermal corrections have been applied to the data (Fig. 2.2). The temperature inside the tunnel changes due to the light emissions. Before August 2017 a simple visit of the personnel in the tunnel of the Conrad Observatory triggers the

17

increase in temperature at about 0.02 to 0.05 degrees Celsius. Since then, both systems are insulated so that short visits there do not disturb the records anymore and this kind of correction is not needed any longer in the future. Therefore, using the TSOFT software the disturbances were removed and the thermally corrected residuals were obtained (Papp pers. Comm).
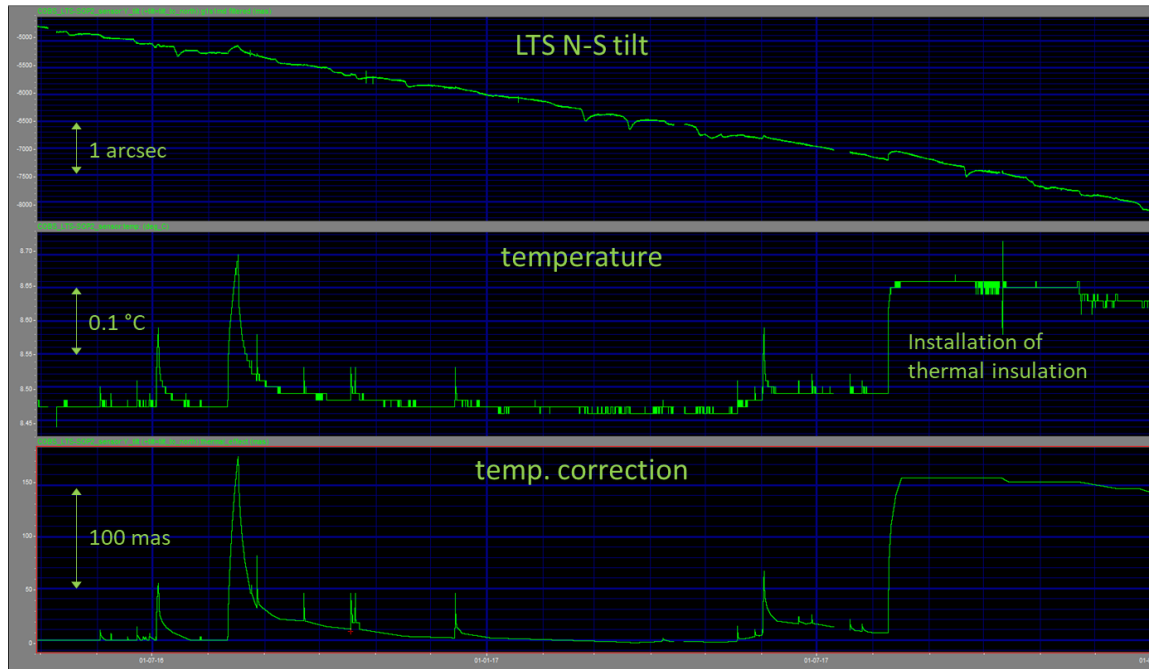

Figure 2.2 Temperature correction based on linear and nonlinear models dependent on the thermal event. Necessity of thermal insulation (Papp pers. Comm)

5) Filtering (G1s1m FIR filter) and decimation to 1 hour data (Meurers pers. Comm.)

6) Prediction of the theoretical tides based on the model derived from tidal analysis (Meurers, pers. Comm.). Subtraction from the observed tilt in order to get the residuals. Then, correction of the air-pressure effect was applied and the admittance factors were obtained by the tidal analysis. The results from the tidal analysis are shown in the next table (Table 2.1).

Darwin	γ (WD)	N-S LTS-Y amp [mas]	N-S LTS-Y γ σ(γ)	N-S LTS-Y φ σ(φ)	E-W LTS-X amp [mas]	E-W LTS-X γ σ(γ)	E-W LTS-X φ σ(φ)	E-W iwt-X γ σ(γ)	E-W iwt-X φ σ(φ)	LTS/iwt
Q1	0.6940	0.1235	2.9289 / 1.3921	-17.218 / 12.022	0.9257	0.6976 / 0.0490	1.776 / 4.042	0.6937 / 0.0851	-13.136 / 7.011	1.0056
O1	0.6944	0.6449	**1.2940** / 0.1533	12.022 / 9.648	4.8347	**0.7105** / 0.0104	-7.020 / 0.838	**0.6783** / 0.0170	-12.356 / 1.434	1.0475
K1	0.7362	0.9070	**1.2184** / 0.1536	10.551 / 7.200	6.7995	**0.7808** / 0.0073	-8.045 / 0.462	**0.7346** / 0.0108	-11.556 / 0.839	1.0629
N2	0.6911	1.5053	**0.6744** / 0.0306	-4.524 / 2.590	2.0279	**0.7516** / 0.0889	-2.863 / 0.676	**0.7200** / 0.0115	-4.697 / 0.918	1.0439
M2	**0.6911**	7.8622	**0.6574** / 0.0060	-2.313 / 0.522	10.5916	**0.7404** / 0.0019	-3.853 / 0.147	**0.6827** / 0.0023	-5.559 / 0.192	1.0845
S2	0.6911	3.6579	**0.6599** / 0.0128	-1.436 / 1.128	4.9278	**0.6865** / 0.0044	-1.609 / 0.363	**0.6306** / 0.0519	-5.493 / 0.460	1.0886

Table 2.1 Results from tidal data processing (Meurers pers. Comm.)

The γ amplitude factors, phases and their corresponding σ (γ) errors for the North-South and East-West components, respectively, are shown. After comparing the theoretical and predicted residuals, it can be concluded that the North-South component shows anomalous diurnal γ-factors. This is most likely due to the 'cavity effect', as I already have explained in the introduction. For the East-West component the γ-factors of the iWT are closer to the prediction of the WD model than for the LTS (Wahr-Dehant model is a model of a non-hydrostatic, inelastic Earth implemented in STANDARD ETERNAA. Tidal parameters are affected by unknown transfer function of the tilt sensors. The LTS scale factor for the East-West component is too high (5 – 8 %), so might be wrong at 8%, because there is no calibration done to the instrument. Tidal parameters are also uncorrected for the ocean tides. It is expected that the cavity effect is going to be stronger in the North-South than in the East-West direction as it has been described in the past by Harrison [11].

7) Finally, trend (drift) correction of the tilt residual data is performed by applying low order polynomials. For the iWT-x-tilt there is a drift (+0.2 arcsec/yr., +0.5 arcsec/yr.) and for the LTS it is larger (-2.0 arcsec/yr. for the y-tilt, -1.5 arcsec/yr. for the x-tilt).

2.3 Meteorological data

As described in the previous chapter for the meteorological sensors, meteorological data like the duration, type and amount of precipitation are permanently acquired. The temperature and humidity are as well included in our data. For this interval (29.04.2016 until 01.08.2017) all these information is obtained. The temperature is important in order to check if and when snow melts and secondly for the rain in order to check if evaporation of water is high or low, specifically during warm summer periods. The

SYNOP-code (Table 2.2) provided by the Laser Precipitation Monitor allows for identifying the precipitation type.

No.	Frequency [Hz]	SYNOP (Tab.4680)	Description
0	1	-1	Sensor error
1	5	0	No precipitation
2	10	51	Light drizzle
3	20	52,53	Moderate / heavy drizzle
4	25	41,42	Unknown precipitation
5	33,33	57,61	Light drizzle with rain, Light rain
6	41,66	58,62,63	Moderate / heavy drizzle with rain, moderate / heavy rain
7	50	67	Light rain and / or drizzle with snow
8	62,5	68	Moderate / heavy rain and / or drizzle with snow
9	83,33	77	Snow grains
10	100	71	Light snow fall
11	125	72,73	Moderate / heavy snow fall
12	166,67	74,75,76	Soft hail / ice grains
13	250	89	Hail

Table 2.2. Types of precipitation [34]

3. Comparison of residuals with environmental processes

3.1 Atmospheric effects: The Air pressure-effect

3.1.1 Influence of barometric pressure variations on tilt

There are strong variations appearing in the air-pressure and finding out if that is noise or a physical signal is part of the environmental study of the atmosphere. It is possible to find the admittance factor which is actually a function dependent on frequency and find how strong it is, means how sensitive is to each frequency band.
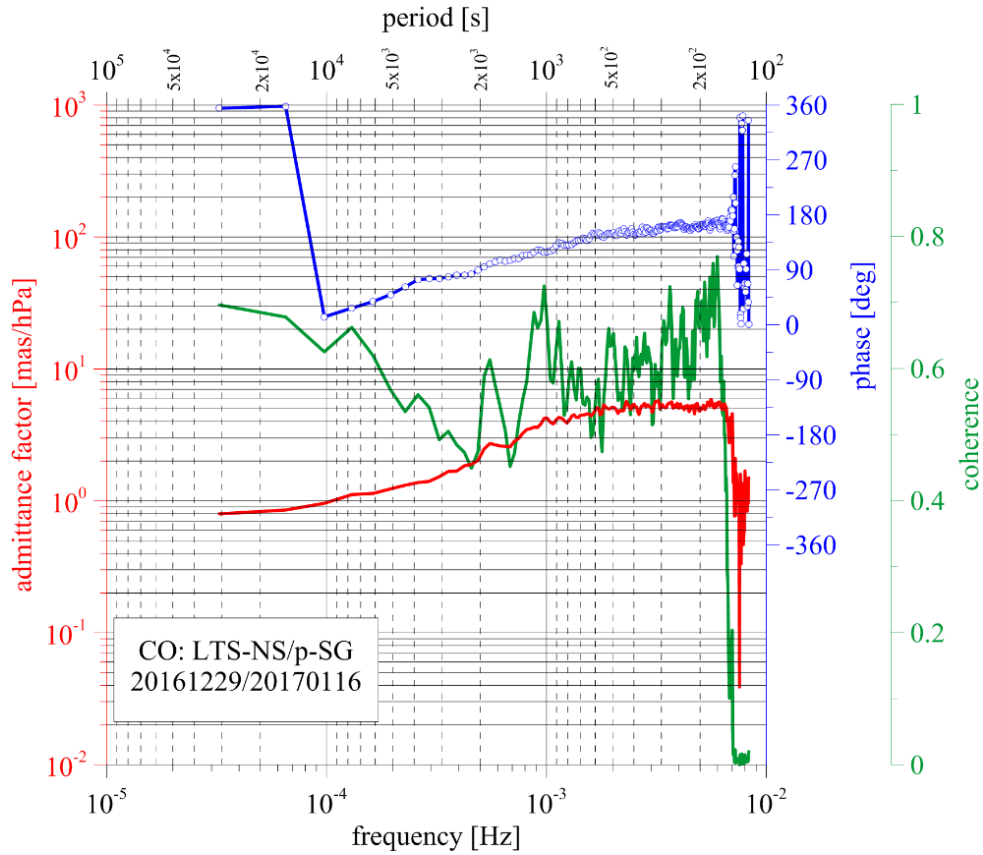

Figure 3.1 Frequency dependent admittance factor for the low period tides. The red line shows the frequency dependent admittance factor [mas/hPa] and the blue line the phase [degrees]. The green line gives the coherence. (Meurers pers. Comm)

After the tidal analysis, as described previously in the paragraph 2.2, it is found that the admittance factor of the y-tilt component of LTS (North-South component) for the low frequency band (periods 1 day to 1 week) is about 0.878 mas/hPa (as it was derived by the ETERNA software, Meurers, pers. Comm). For higher periods (weeks or months) a clear admittance factor cannot be derived, because the tidal analysis filters out all long period part of tides. For the East-West component, the admittance factor is 0.042 mas/hPa (for the x-tilt of the LTS) and -0.195 mas/hPa (for the x-tilt of the iWT). The

following plot (Fig. 3.1) gives an example of the admittance factor of the y-tilt component of the LTS. An interval of 29.12.2016 till 16.01.2017 is chosen in order to obtain a good frequency and also period resolution of the signal. As it is depicted in the figure 3.1, the admittance factor starts to be about 0.8 mas/hPa at the low frequency band and then slowly seems to increase with frequency. Again it has to be remarked, that the transfer function is unknown and the tidal parameters may be affected by this unknown transfer function. Coherence is also depicted in the figure by the green line and shows how the behavior (wave form, phase difference) of the two quantities, air-pressure and y-tilt, are related for each range of frequencies.

3.1.2 Sensor dependent admittance factor for the high frequency band

In my attempt to understand if that's a constant phenomenon or it dependent on the weather system that produces the air-pressure signals, we search for variations of the frequency dependent admittance factor in the high frequency band (periods from 12 to 24 hours). What first is done is the removal of the very strong hydrological events which prevent us from finding the air-pressure effect. The process is performed by using again TSOFT, where the strong variations of the y-tilts due to the precipitation are isolated and erased. The tides are also removed and thus the new tilt residuals are retrieved. Only short time intervals (from 12 to 24 hours) are selected and search follows to how the tilt residuals do react on the air-pressure. After filtering the data, applying low degrees of polynomials, in TSOFT, in order to keep only the high frequencies in this interval, correlations are performed between the air-pressure and the y-tilt residual, only in these short time intervals. A simple correlation process is performed by applying Fourier Transform (Meurers pers. Comm.). Thus, the admittance factor and the phase in respect to frequency, and also the coherence, are derived as an output file. Through this analysis, the frequency dependent admittance for many selected short time intervals is extracted and it is validated that in the higher frequency band the admittance factor is increasing. As an example I present the following plot (Fig. 3.2) which refers to a 24-hour interval, in the date 2016.06.19. As it is also shown in this figure, the coherency ranges from 0.75 to 1 until at 2 mHz, and after this frequency, it starts decreasing. In the higher frequency range $[10^{-3} \, to \, 10^{-2} Hz]$ the coherence is getting very small.
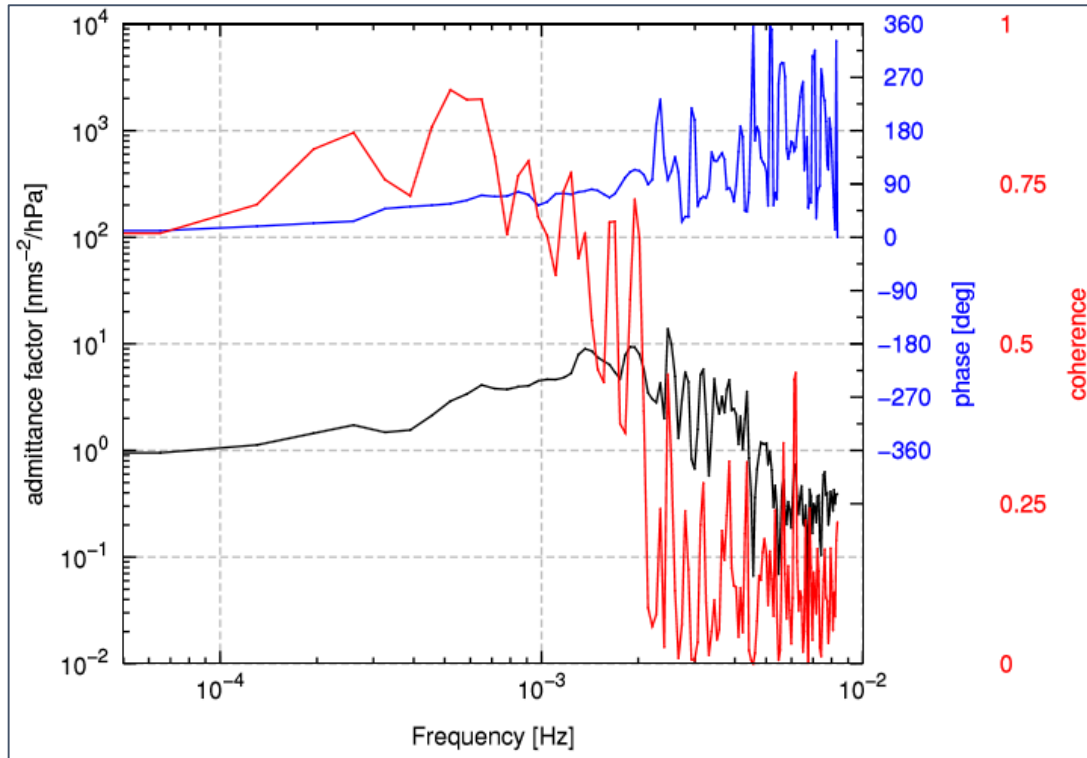
Figure 3.2 Frequency dependent admittance factor for the high frequency band for a 24-hour time interval in the date 2016.06.19. Black line gives the admittance factor, the blue gives the phase. Red line shows the coherence.

3.2 Hydrological effect from precipitation

3.2.1 Observation of the signals

Gravity and tilt residuals, obtained according to paragraphs 2.1 and 2.2, are compared in the following figure (Fig. 3.3) within the period between 26 April 2016 and 31 December 2017. Cumulative rain fall and snow (water equivalent) are shown as well.
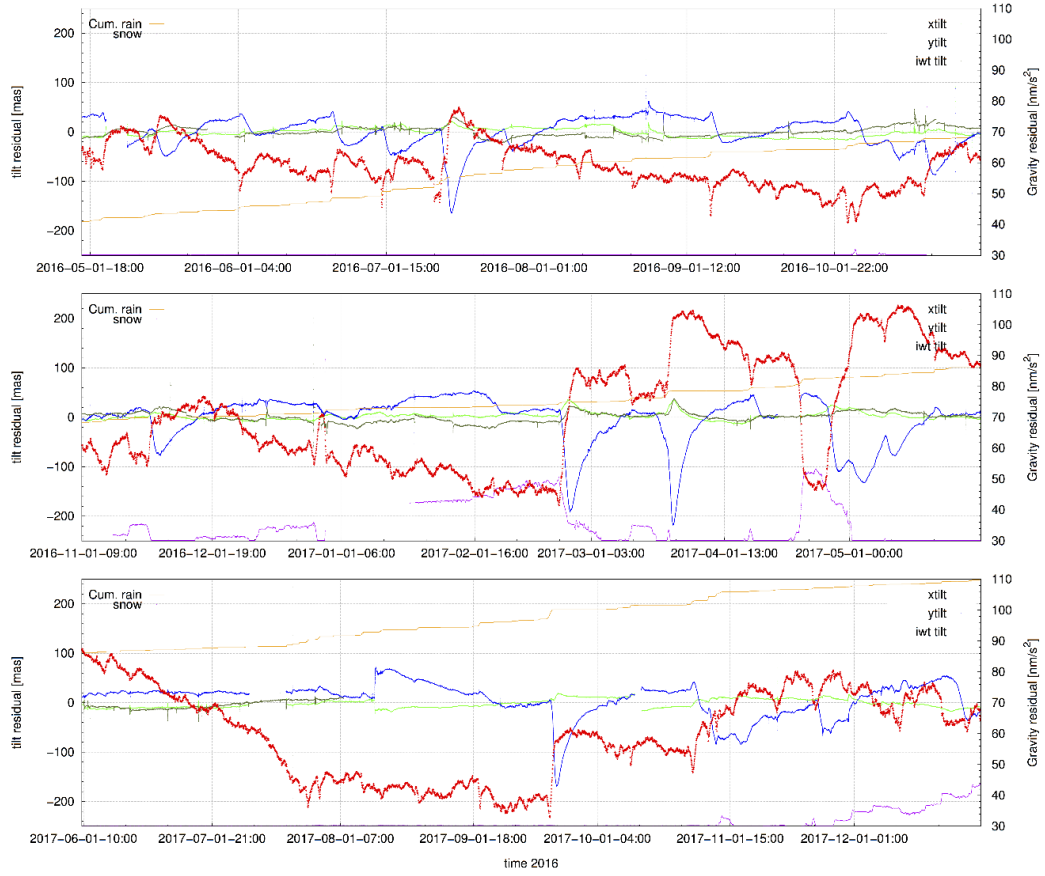
Figure 3.3. Total Figure with residuals and precipitation. Gravity residual is given by the red colour, y-tilt residual by the blue colour. The corresponding units are in [nm/s^2] and [mas] respectively. The light green color indicates the x-tilt residual of the LTS and the dark green the x-tilt residual of the iWT. Precipitation is shown by the orange color (cumulative rain) and the purple color (snow-water equivalent). The units are in [mm].

It can be very clearly noticed from the figure 3.3 that there are 4 big drops (steep reduction) of the y-tilt residual (blue color) and a couple of smaller residual drops always coinciding with a steep increase of the gravity residual (red color). The x-components of both the iWT and LTS sensors seem to have mostly the same behavior after a rain or snow event, but their fluctuations are less intense than these of the y-tilt residuals. All these typical residual signatures are associated with heavy precipitation or quick snow melt events. Heavy rain events are imaged at the beginning by a sharp gravity residual decrease which is due to the fact, that the SG is an underground installation. Later, when sufficient amount of surface water is available, gravity residuals start to increase slowly [43]. A possible interpretation is water mass transport

24

from topography downwards and accumulation below the SG sensor (Fig. 3.4). The gravity increase starts almost at the same time, when the y-tilt residuals begin to decrease. This supports the idea that the tilt residual anomalies are actually triggered by the same hydrological processes. The question is if they are caused either by the same or by different sources.

Figure 3.4 Gravity residual anomalies triggered by hydrological processes under Conrad. The location of the SG sensor inside the observatory is shown.
(Meurers, Dorninger, pers. Comm.)

For revealing similarities of these rain or snow melt events, they are individually inspected separating in total 20 events, where pronounced y-tilt residual drops appear. For identification of the events, the date, when the y-tilt residual starts to decrease, is used. Exemplarily, the figure 3.5 describes the '2016.07.12 event', which shows one of the 4 deepest drops of the y-tilt residual.
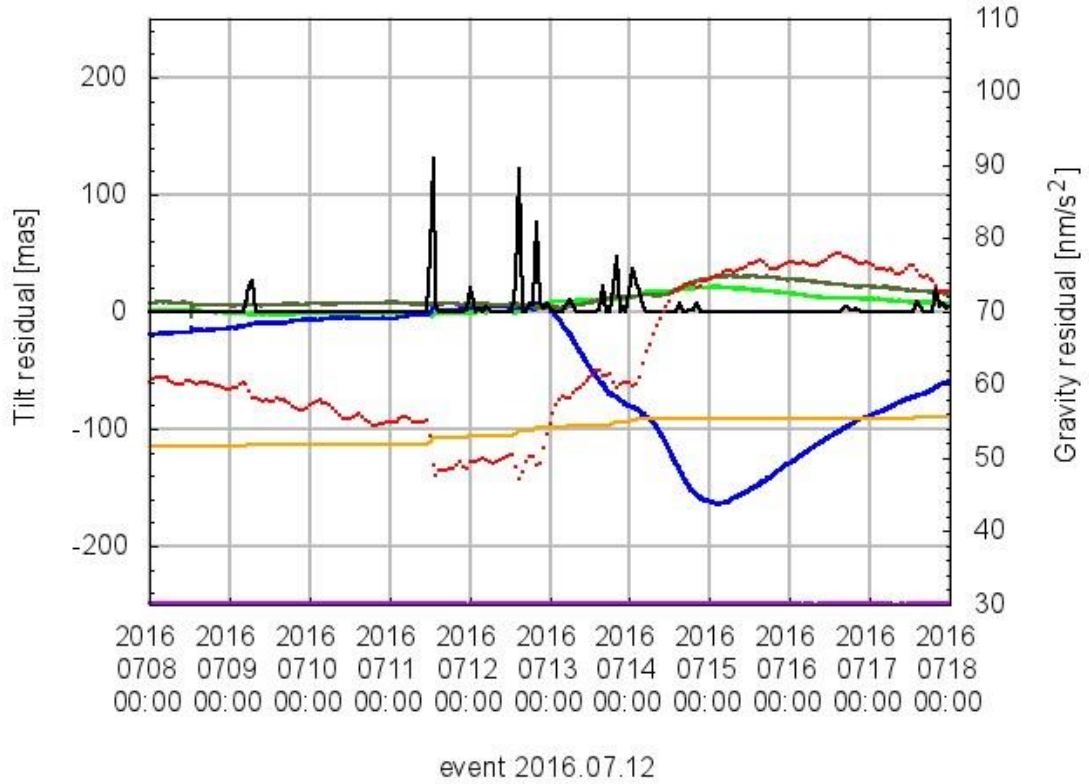
Figure 3.5. The '2016.07.12 event'. After some rain (black color), the increase in the gravity residual is seen (red color) and the corresponding decrease in the y-tilt residual (blue color). Cumulative rain shown by orange color. There is no snow (purple color). Both x-tilt residuals (green colors) appear to have the same behavior. The units for cumulative rain and snow are in [mm].

After carefully observing this event, the following explanation can be given: There is a pure rain event from July 11 to 13 and during this precipitation, the gravity residual decreases. After sufficient rain water has accumulated, the gravity residuals start to increase followed by a time delayed y-tilt decrease. Additional rain appearing from July 13 to 14 obviously increases the gravity residuals and decreases the y-tilt residual further. The latter reaches the minimum value of -164 mas on July 14. The x-tilt residuals (iWT, LTS) have similar fluctuations and appear to increase both in a similar way.

All the other 19 similar events are shown in Appendix I and II. Appendix I summarizes all the 9 pure rain events, Appendix II all the 11 mixed- rain and snow events associated both with the rain and snow.

3.2.2 Analysis of events

An attempt is made to study the events not only in a qualitative but also in a quantitative way. Because the assessment of water which can intrude into the subsurface is more complicated when both rain and snow melt contribute, pure rain events and mixed- rain and snow events are considered separately. The analysis is based on quantifying the amount of water available for mass transport from topography downwards into the subsurface. The following procedure is applied:

For each event,

A) The cumulative rain over 5 days is counted before gravity residuals start to increase
B) The duration of rain is determined during this interval and rain rates are derived
C) The tilt-residual drop associated with the event is quantified
D) The time delay is quantified between gravity residual increase and y-tilt residual decrease by determining the time difference between the zero crossings of the low pass filtered residuals' time derivative (Fig. 3.6). Polynomial filtering (Savitsky-Golay) of degree 3, has been used for that purpose and then the derivative is retrieved.

The process is exemplarily described by the event shown in the figure 3.6: gravity residuals start to increase on July 12, 2016, at 15:00. Y-tilt starts to decrease at 20:00. Duration of rain during the 5-days interval before gravity residuals increase is 11h with cumulative rain of 73 mm, resulting to a rain rate of 6.7mm/h. The total y-tilt decrease is 80 mas. X-tilt increases by 14 mas (LTS) and 8 mas (iWT). Rainfall continues between July 12 and July 14 with cumulative rain of 35 mm, a rain rate of 3.18mm/h, which causes a gravity residuals decrease first until July 14, when they increase again. At the same time, y-tilt decreases further by 84 mas, while the x-tilts continue to increase to 22 mas (LTS) and 32 mas (iWT). This analysis is performed for all the 9 pure rain events. It is remarkable, that the time-shift (time delay) between the gravity residual increase and the y-tilt residual drop is observed in almost all events and its range is from 1 to 6 hours. I try to give an explanation for this phenomenon later, in the following paragraphs, while searching for the true hydrological process occurring under Trafelberg.
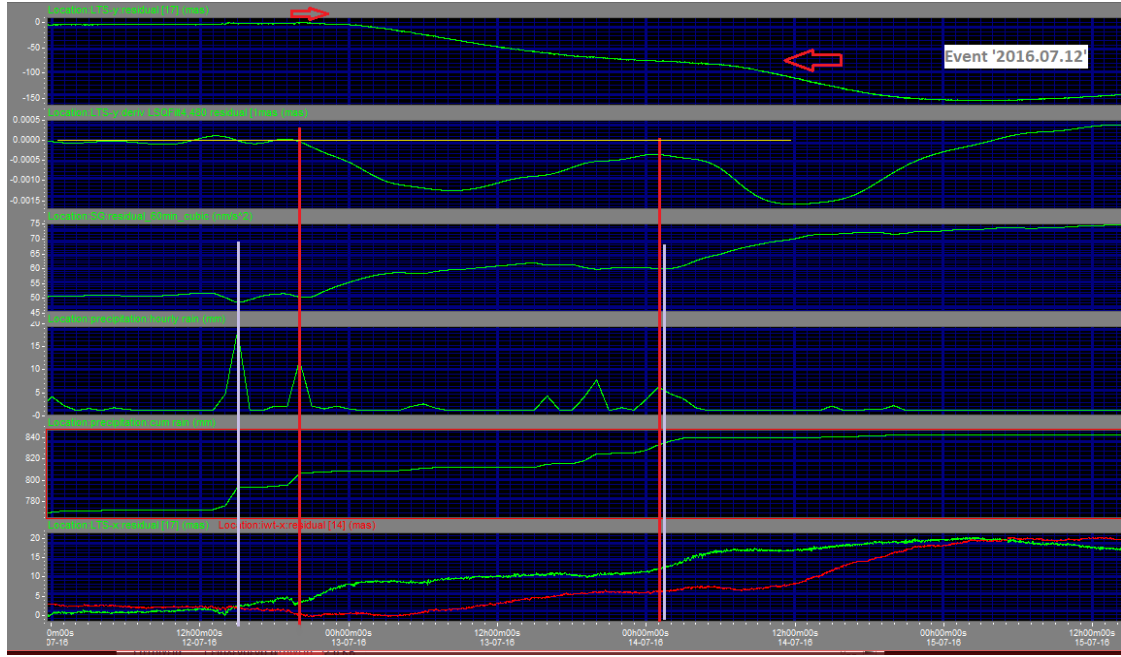
Figure 3.6. Calculation of time shift between the y-tilt and gravity residual for the '2016.07.12' event (TSOFT). First panel depicts the y-tilt residual, second one the time derivative of it. Third panel is the gravity residual. The last panels depict the rain, cumulative rain and both the x-tilt residuals, respectively. The white line depicts when the gravity residual starts to increase and the red line when the y-tilt residual starts to decrease (means where the derivative starts to be negative). The red arrows show the small short-term increase of the y-tilt residuals before their final drop.

Furthermore, looking more carefully on the events, it is revealed that a small short-term increase of the y-tilt residuals can be observed just before their starting route to decrease. This phenomenon occurs at each event and is depicted by red arrows (see also Appendix III). The reason is not clear yet, but maybe it is associated with the accumulation of water somewhere, as it will be discussed also later. Table 3.1 presents all the 9 pure rain events with their corresponding estimates. The table contains also some rain events, which are not associated by big drops of the y-tilt residuals, called as 'rain events with no abnormal tilt or SG residuals'. Those are used later for trying to derive conditions under which a y-tilt residual drop appears.

28

EVENTS DATE	Measured Interval before event	Duration of interval [hours]	RAIN Duration of rain [hours]	RAIN Total cum rain [mm]	RAIN E/D Rate [mm/hour]	Gravity increase starting time	y-tilt decrease starting time	Time shift [hours]	y-tilt min. value TIME	y-tilt min. value [mas]	Δy-tilt decrease [mas]	x-tilt (LTS) max. value [mas]	Δx-tilt (LTS) increase [mas]	x-tilt (iWT) max. value [mas]	Δx-tilt (iWT) increase [mas]
May 2016															
	29.04-4.05	120	20	37	1,85	4.05 at 7.00h	4.05 at 7.00h	0	GAP!	GAP!	20?	GAP!	GAP!	GAP!	GAP!
2016.05.13	8.05-13.05	120	18	28	1,56	13.05 at 22.00h	13.05 at 22.00h	0	17.05 at 8.00h	-50	66	2	9	14	21
June 2016															
	27.05-1.06	120	5	39	7,80	1.06 at 13.00h	1.06 at 15.00h	2	6.06 at 12.00h	-10	48	noisy!	noisy!	noisy!	noisy!
2016.06.20	15.06-20.06	120	18	54	3,00	20.06 at 9.00h	20.06 at 15.00h	6	23.06 at 6.00h	-33	71	12	9	12	13
2016.06.30	25.06-30.06	120	13	64	4,92	30.06 at 18.00h	30.06 at 21.00h	3	3.07 at 00.00h	-46	55	14	8	13	9
July 2016															
2016.07.12	7.07-12.07	120	11	73	6,64	12.07 at 15.00h	12.07 at 20.00h	5	14.07 at 00.00h	-73	80	17	14	13	10
	12-14 addit.	rain	11	35	3,18	14.07 at 1.00h	14.07 at 1.00h	0	15.07 at 3.00h	-164	84	22	5	32	20
2016.07.25	20.07-25.07	120	7	41	5,86	25.07 at 14.00h	25.07 at 19.00h	5	27.07 at 13.00h	-37	41	noisy!	noisy!	noisy!	noisy!
August 2016															
	5.08-10.08	120	14	53	3,79	10.08 at 11.00h	10.08 at 14.00h	3	11.08 at 14.00h	noisy!	_	noisy!	noisy!	noisy!	noisy!
Sept 2016															
2016.09.06	1.09-6.09	120	17	67	3,94	6.09 at 11.00h	6.09 at 11.00h	0	9.09 at 3.00h	-21	60	-7	19	-4	16
Oktob 2016															
2016.10.20	15.10-20.10	120	16	35	2,19	20.10 at 8.00h	20.10 at 9.00h	1	22.10 at 7.00h	-80	69	noisy!	noisy!	noisy!	noisy!
Nov 2016															
	1.11-6.11	120	21	32	1,52	6.11 at 19.00h	6.11 at 22.00h	3	9.11 at 00.00h	no	_	_	_	_	_
July 2017															
	22.07-27.07	120	29	78	2,69	27.07 at 9.00h	27.07 at 12.00h	3	1.08 at 20.00h	9	28	_	_	_	_
Sept 2017															
	29.08-3.09	120	15	49	3,27	3.09 at 9.00h	3.09 at 9.00h	0	8.09 at 3.00h	-3	31	noisy!	noisy!	no info	no info
2017.09.20	14.09-19.09	120	32	82	2,56	19.09 at 23.00h	20.09 at 1.00h	2	21.09 at 13.00h	-169	179	18	13	no info	no info
Okt 2017															
	4.10-9.10	120	23	37	1,61	9.10 at 1.00h	GAP!	_	GAP!	GAP!	_	GAP!	GAP!	no info	no info
	18.10-23.10	120	20	46	2,30	23.10 at 23.00h	24.10 at 00.00h	1	26.10 at 10.00h	-20	62	6	14	no info	no info
2017.10.27	23-28 addit.	rain	6	35	5,83	27.10 at 11.30h	27.10 at 15.00h	3,5	29.10 at 4.00h	-65	76	10	12	no info	no info
Nov 2017															
	7.11-12.11	120	18	12	0,67	12.11 at 17.00h	no	_	_	_	_	_	_	no info	no info

Table 3.1. The total 9 pure rain events & also the rain events with no abnormal tilt/SG residuals are shown. The first 5 columns indicate the measured interval before each event (dates, and duration [hours]) and the total duration [hours], amount [mm] and corresponding rates [mm/hour] of cumulative rain. In the next columns, the times when the gravity and y-tilt residuals start to change, are noted, and the estimated time delay between them [hours]. In the last 7 columns, all the rest estimations are presented: The time when the y-tilt residual reaches its minimum [date], the minimum values and absolute measures of decrease of it [mas], the maximum and absolute measures of increase of the two x-tilt residuals [mas], of the LTS and iWT sensors.

The same calculations are performed for the 11 mixed rain- and snow-events. The corresponding figures are shown in the Appendix III and IV, respectively. However, it is not so easy to follow the same analysis as for the pure rain events. The rain gauge counts all water independent of its aggregate state. Snow water equivalent provides how much molten snow water is available in case of snow melt. Hence, the total amount of water may be biased when snow melt and precipitation happen at the same time. Here, the total water estimate is calculated by adding the amount of cumulative rain water to the snow melt water. It has to be emphasized that in case of snow events the environmental conditions play a very important role. In the attempt to decide if the snow melts and turns into water or not, air temperature has to be considered, however, the uncertainty of the total water estimate is higher than in the pure rain events.

As an example the mixed- rain and snow event '2016.11.16' (Appendix II) is presented. The y-tilt residual starts to decrease at November 11, 19:00 with a total drop of 85mas. Rain falls between November 11 and November 16 over in total 17 h and yields to 21 mm rain. At November 16, 6:00 air temperature is about 6.8 deg. C, which means that the snow has started to melt at that time. The following figure explains in more detail, how the total amount of molten snow is estimated (Fig. 3.7).
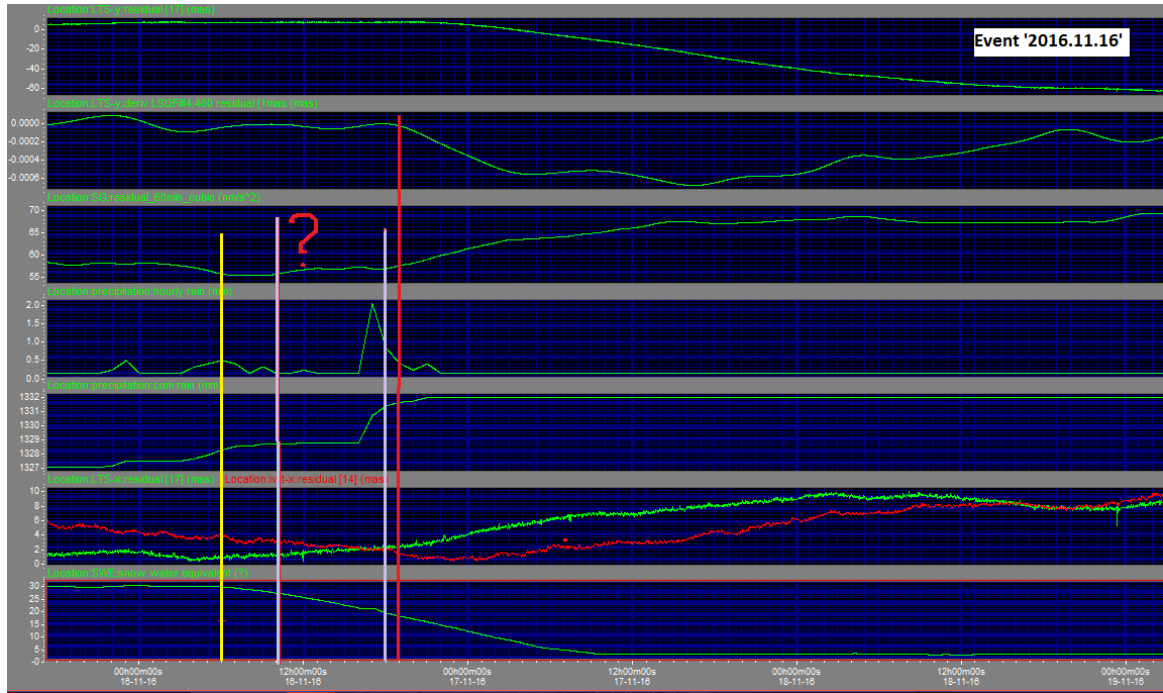
Figure 3.7 Estimation of the amount of the snow water for the event '2016.11.16'. Red question mark indicates that the gravity residual in not clear when it starts to increase for this case event (Picture is printed from TSOFT).

The yellow line in the figure 3.7 marks the time when snow starts to melt. The red line shows the time when y-tilt residuals starts to decrease and the white line the time when the gravity residual starts to increase, which is not so clear for this event. The total amount of snow water is the difference of snow water equivalent between the time when snow starts to melt (November 11, 6:00) and the time when the y-tilt starts to decrease (November 11, 19:00), estimated by about 14mm. Adding this number to the amount of cumulative rain water (21mm) results to a total water amount of 35mm. The other corresponding figures of the 11 mixed- rain and snow events showing the estimation of the total amount of the melted snow water, are displayed in Appendix V.

The next table (Table 3.2) summarizes all the 11 the mixed-rain and snow- events with their corresponding estimates.

31

EVENTS DATE	Measured Interval before event	Duration of interval [hours]	RAIN Duration of rain [hours]	Cum rain [mm]	Average Temper [Celsius]	SNOW Snow melt [starting time]	Snow water [mm]	TOTAL WATER [mm]	Gravity increase [starting time]	y-tilt decrease [starting time]	Time shift [hours]	y-tilt min. value [Time]	y-tilt min. value [mas]	Δy-tilt decrease [mas]	x-tilt (LTS) max. value [mas]	Δx-tilt (LTS) increase [mas]	x-tilt (iWT) max. value [mas]	Δx-tilt (iWT) increase [mas]
Oktob 2016																		
2016.10.06	1.10-6.10	120	26	58	3	6.10 at 4.00h	4	62	6.10 at 8.00h	6.10 at 8.00h	0	9.10 at 9.00h	-27	58	-8	22	12	14
2016.10.12	7.10-12.10	120	18	14	2,4	11.10 at 3.00h	7	21	*not clear*	12.10 at 07.00h	?	15.10 at 6.00h	-49	41	2	10	19	21
Nov 2016																		
2016.11.16	11.11-16.11	120	17	21	6,8	16.11 at 6.00h	14	35	16.11 at 10.00 or 18.00h?	16.11 at 19.00h	9 or 1 ?	19.11 at 5.00h	-68	85	10	10	20	13
Febr 2017																		
2017.02.21	16.02-21.02	120	14	19	4	21.02 at 13.00h	8	27	21.02 at 14.00h	21.02 at 15.00h	1	24.02 at 10.00h	-175	195	17	25	20	31
March 2017																		
2017.03.18	13.03-18.03	120	8	27	6,9	14.03 at 15.00h	29	56	18.03 at 11.30h	18.03 at 12.00h	0,5	20.03 at 12.00h	-212	181	35	27	36	33
April 2017																		
2017.04.25	20.04-25.04	120	11	20	8,1	23.04 at 4.00h	31	51	25.04 at 8.30h	25.04 at 10.00h	1,5	29.04 at 13.00h	-103	137	noisy	noisy	noisy	noisy
2017.04.30	25.04-30.04	120	16	8	8	23.04 at 4.00h	80	88	30.04 at 17.00h	30.04 at 22.00h	5	4.05 at 8.00h	-130	50	noisy	noisy	noisy	noisy
Mai 2017																		
2017.05.09	4.05-9.05	120	15	30	2,7	9.05 at 11.00h	4	34	9.05 at 8.00h	9.05 at 13.00h	5	11.05 at 3.00h	-68	37	9	8	15	8
Nov 2017																		
2017.11.02	28.10-2.11	120	11	49	7,8	30.10 at 12.00h	22	71	2.11 at 9.00h?	2.11 at 17.00h	8?	4.11 at 4.00h	-82	22	14	6	no info	no info
2017.11.21	16.11-21.11	120	17	21	7,6	19.11 at 15.00h 21.11 at 10.00h	4 + 15	40	21.11 at 20.00h	21.11 at 22.00h	2	23.11 at 14.00h	-62	69	15	11	no info	no info
Dec 2017																		
2017.12.24	19.12-24.12	120	10	21	7	21.12 at 22.00h	4	25	*not clear*	24.12 at 3.00h	?	27.12 at 23.00h	-15	53	-10	7	no info	no info

Table 3.2. The total 11 mixed-rain & snow- events are presented. The performed analysis is similar to the analysis fulfilled also for the 9 pure rain events.

3.2.3 Correlations

The following relations have been studied, based on tables 3.1 and 3.2, both for the pure rain events alone and then for the mixed- rain and snow events:

- y-tilt and x-tilt residuals vs. total accumulated water
- total amount of the water vs. observable time delay (time-shift) which exists between the y-tilt and the gravity residuals.

3.2.3.1 Correlation between y-tilt residual (LTS) and precipitation

The first attempt is to correlate the absolute value of the y-tilt residual drop with the amount of cumulative rain (Fig. 3.8). The correlation coefficient is 0.78± 0.21. A t-test distribution calculation is used to assess the probability associated with the test statistics by the P-value. In other words, the t-test provides the probability that the observed (calculated) correlation is a result of a fluctuating zero-correlation hypothesis taking under consideration the statistical error of the correlation coefficient and the degree of freedom (number of events). Here, the P-value (or probability) is found to be P (T ≥ t) = 0.0024 (99.76% significance level that the correlation is not a fluctuation). All calculations are made in an online T-test distribution calculator [44]. More details on this procedure are shown in Appendix VI.
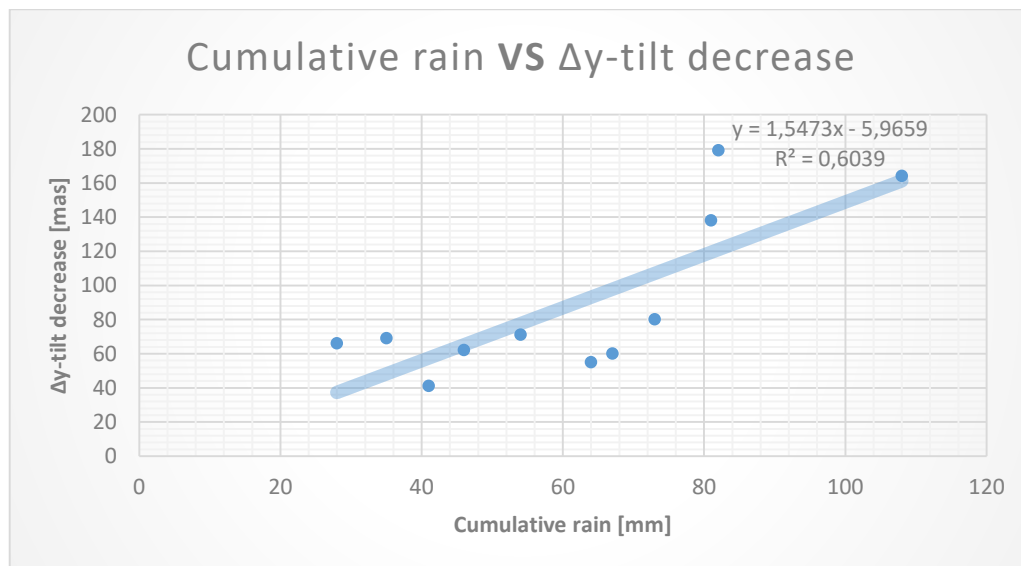
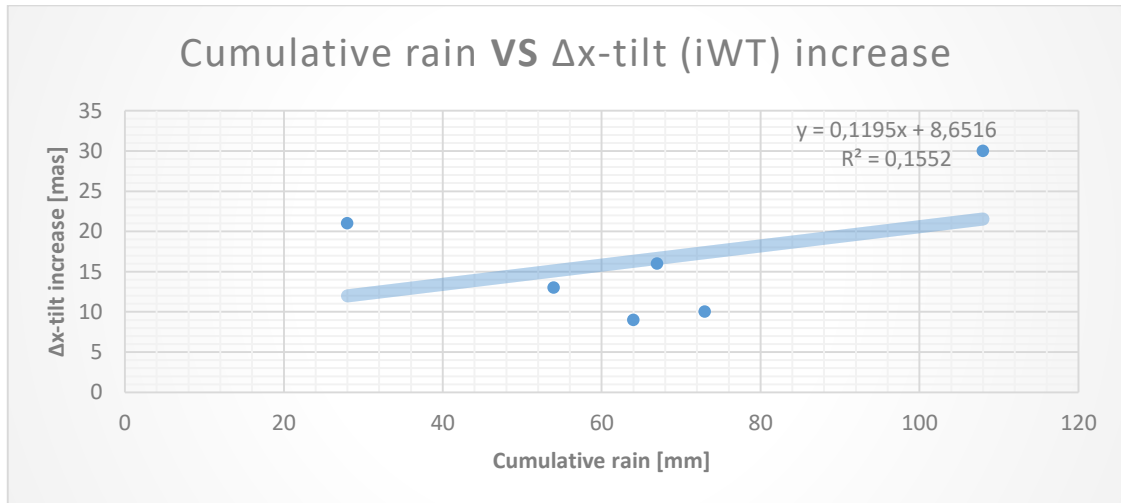*Figure 3.8. Correlation for all the 11 pure rain events, between the cumulative rain*
[mm] and the absolute values of drops of the y-tilt residuals [mas]

For the mixed-rain and snow-events (Fig. 3.9) it is found that a negative correlation of 0.15± 0.33 exists. The t-test finds the probability to be P (T ≥ t) =0.3317. For the correlations that we don't have a significance level above 95% (typical value), I do not

mention the significance. However, if the reader wants to extract it, he can trivially apply the equation in Appendix VI.
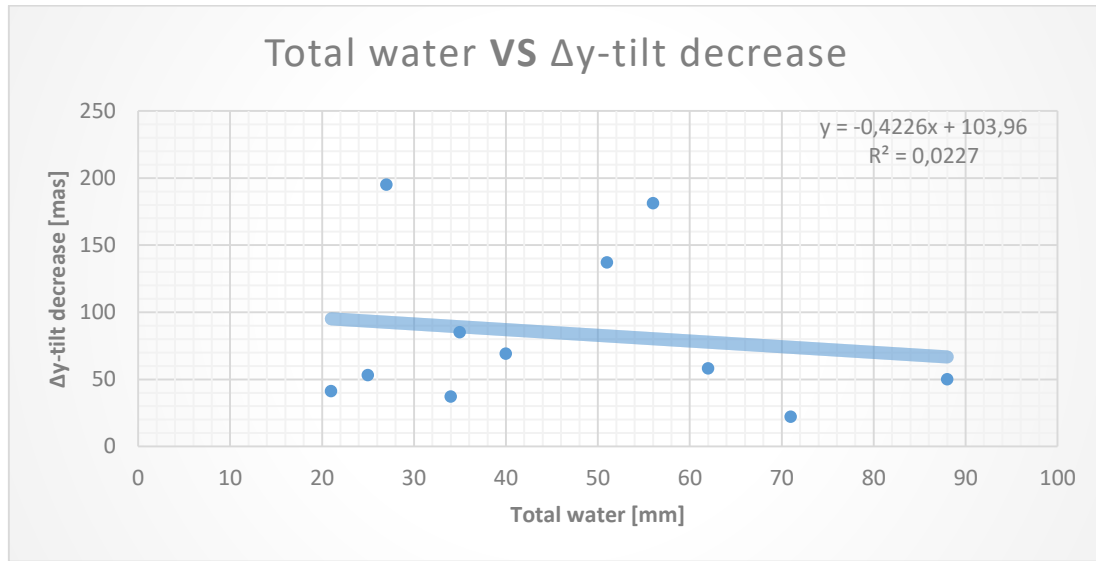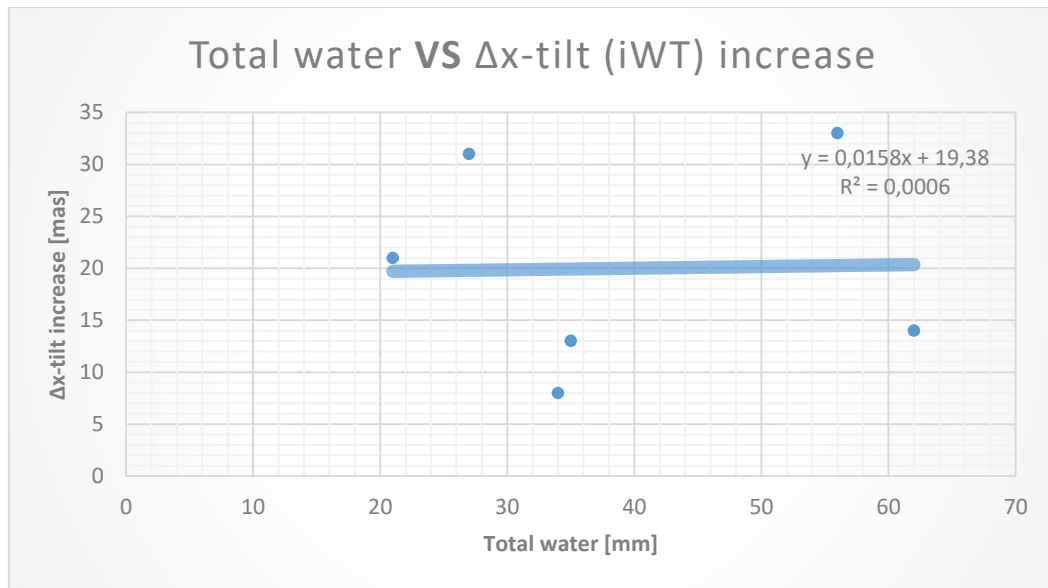

Figure 3.9. Plot shows correlation, for all the studied 11 mixed- rain and snow events, between the total amount of water [mm] and the absolute values of drops of the y-tilt residuals [mas]

3.2.3.2 Correlation between x-tilt (LTS) residual and precipitation
For the pure rain events the correlation is 0.58 ± 0.31 (Fig. 3.10), for the mixed events 0.06 ± 0.38 (Fig. 3.11). The corresponding probabilities are P (T $\geq$ t) = 0.0518, and P (T $\geq$ t) = 0.4387, respectively.
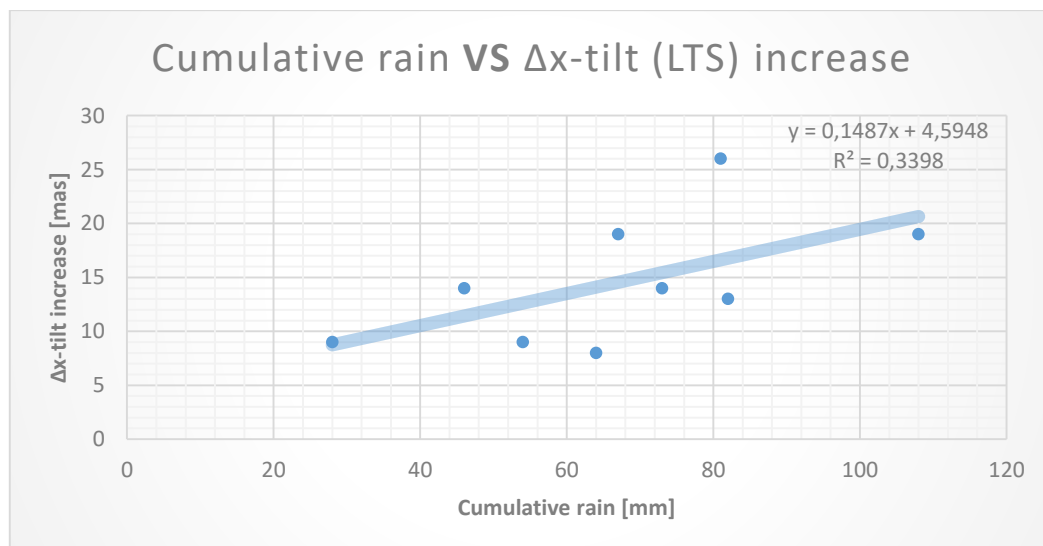
Figure 3.10. Plot shows correlation, for the studied 9 pure rain events, between the cumulative rain [mm] and the absolute values of increase of the x-tilt (LTS) residuals [mas]

34
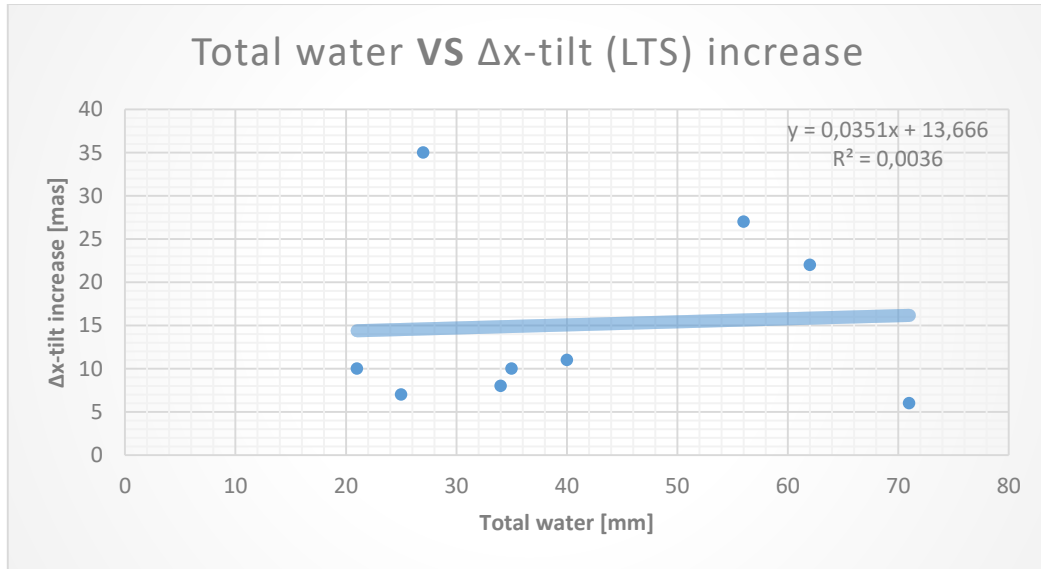
Figure 3.11. Plot shows correlation, for the studied 9 mixed- rain and snow events, between the total amount of water [mm] and the absolute values of increase of the x-tilt (LTS) residuals [mas]

3.2.3.3 Correlation between x-tilt (iWT) residual and precipitation

Finally the same correlations for the x-tilt component of the iWT sensor are performed. For the pure rain events the correlation is 0.39 ± 0.46 (Fig. 3.12) and for the mixed events it is 0.025 ± 0.50 (Fig. 3.13). The corresponding probabilities are P (T ≥ t) = 0.2216, and P (T ≥ t) = 0.4813, respectively.

Figure 3.12. Plot shows correlation, for the studied 6 pure rain events, between the cumulative rain [mm] and the absolute values of increase of the x-tilt (iWT) residuals [mas]

Figure 3.13. Plot shows correlation, for the studied 6 mixed- rain and snow events, between the total amount of water [mm] and the absolute values of increase of the x-tilt (iWT) residuals [mas]

3.2.3.4 Correlations related with the time-shift between the y-tilt and gravity residuals

As described in chapter 3.3 the time delays between the start of gravity residual increase and y-tilt residual decrease have been found. The correlation analysis between time-shifts and the total amount of precipitation as well as between time shifts and rain rates (only in the case of the pure rain events) results to a correlation of 0.26 ± 0.32 with P (T $\geq$ t) = 0.2187 (Fig. 3.14) and 0.63 ± 0.26 with P (T $\geq$ t) =0.0192 (Fig. 3.15), respectively. In the last one the significance level is 98.08% meaning that the correlation is not a fluctuation.
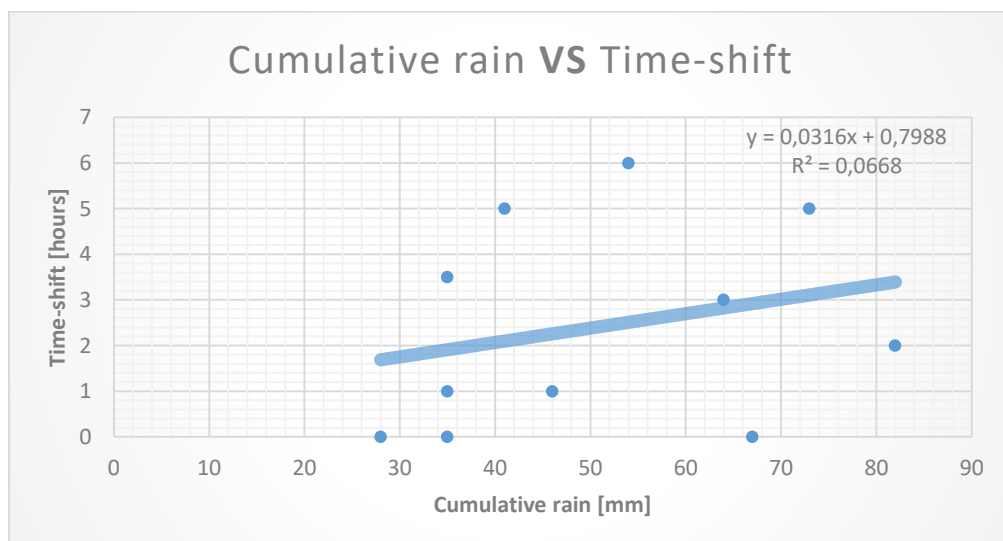
Figure 3.14. Plot shows correlation, for all the studied 11 pure rain events, between the total cumulative rain [mm] and the time-shift between the y-tilt and gravity residuals [hours]
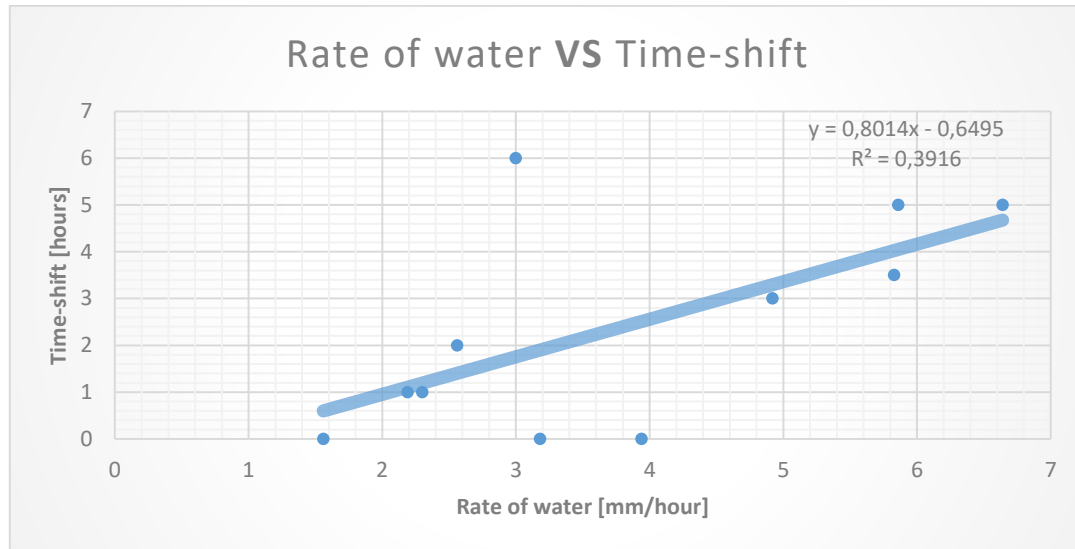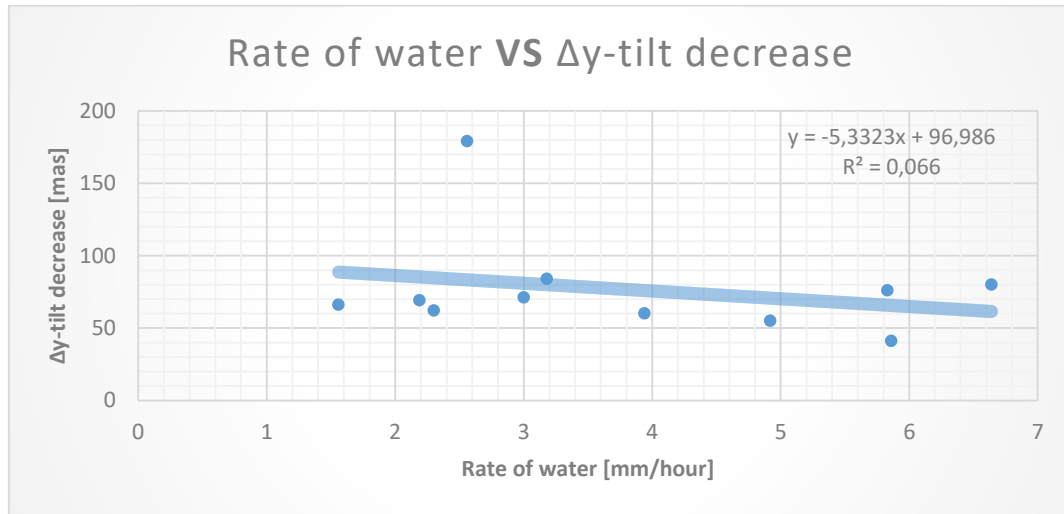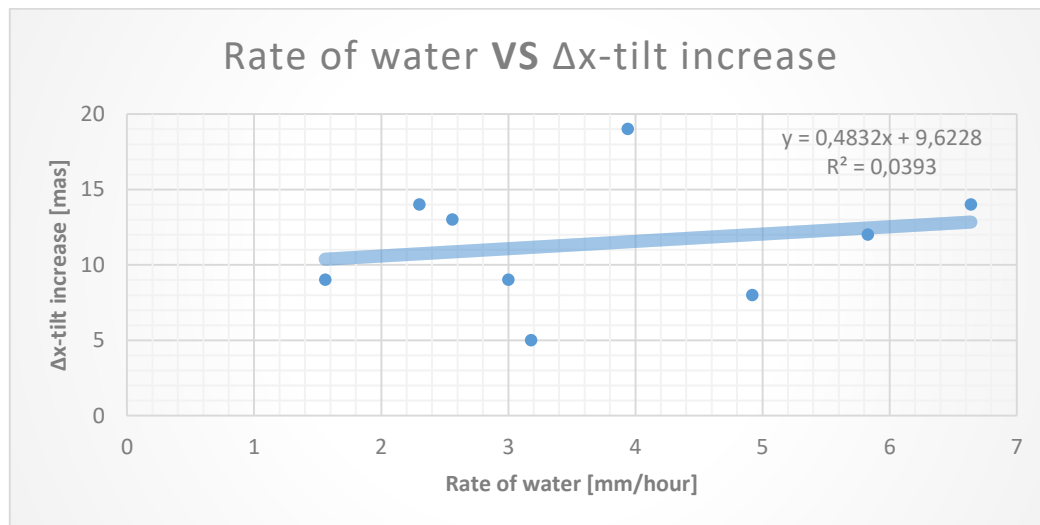

Figure 3.15. Plot shows correlation, for all the studied 11 pure rain events, between the rate of the total water [mm/hour] and the time-shift between the y-tilt and gravity residuals [hours]

For the mixed- rain and snow events, correlation is performed only with the total amount of water, because the rates are not easy to be calculated due to snow's complicated nature, as it was explained again in the previous paragraph. Figure 3.16 shows a correlation of 0.22 ± 0.44 for the mixed events with a corresponding probability of P $(T \geq t)$ =0.3191.
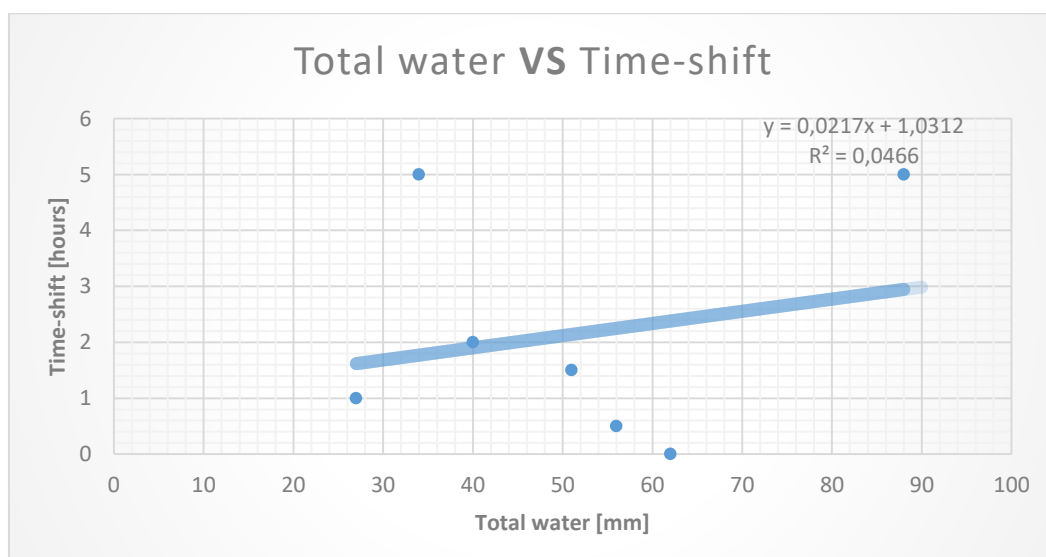
As an alternative check for a possible improvement, I decide to add also the 7 number of events with 'no abnormal tilts and SG residuals' and to recalculate the previous correlation. These events with the corresponding time-shifts are seen in the next Table.

Events with no abnormal tilts DATE	Cum rain [mm]	Rate of water [mm/hour]	Time-shift [hours]	INFO
2016.05.04	37	1,85	0	*GAP*
2016.06.01	39	7,8	2	-10
2016.08.10	53	3,79	3	–
2016.11.06	32	1,52	3	–
2017.07.27	78	2,69	3	–
2017.09.03	49	3,27	0	-3
2017.10.24	46	2,3	1	-20

Table 3.3. Events with 'no abnormal tilt and SG residuals'. The cumulative rain, the rate of water and the time delay are shown.

The results display now that the correlation is 0.28± 0.24 with a corresponding probability of P (T ≥ t) = 0.1315 between the total amount of cumulative rain and the time-shift, and 0.46± 0.22 with a corresponding probability of P (T ≥ t) = 0.0265 between the rate of water and the time-shift (97.35% significance level that the correlation is not a fluctuation). It can be concluded that the resulted correlation coefficients are approximately the same as before.

3.2.3.5 Correlations between the rates of water with the absolute values of the drops of y-tilt

Between the rates of water and the absolute values of y-tilt and x-tilt residuals exists a negative correlation of 0.26± 0.32 with a probability of P (T ≥ t) = 0.2187, and a

positive correlation of 0.20± 0.37 with a probability of P (T ≥ t) = 0.303, respectively (Figs. 3.17 and 3.18). The resulted correlations are insignificant.
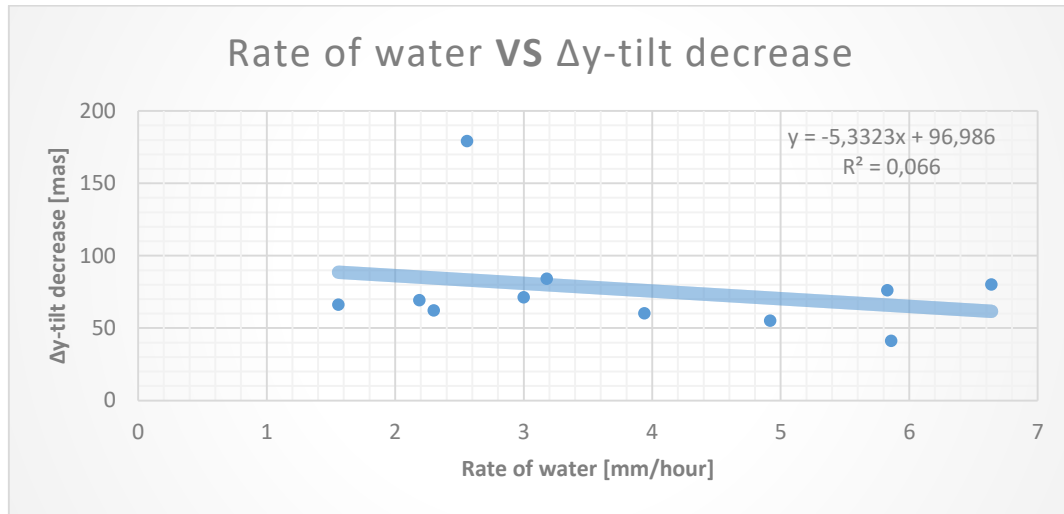

Figure 3.17. Plot shows correlation, for all the studied 11 pure rain events, between the rate of the total water [mm/hour] and the absolute values of drops of the y-tilt residuals [mas]
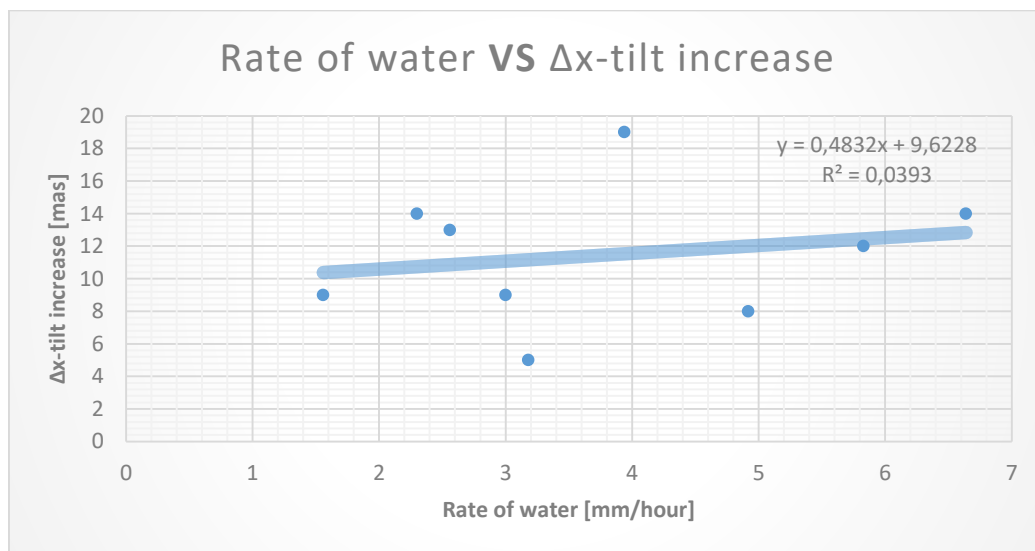

Figure 3.18. Plot shows correlation, for the studied 9 pure rain events, between the rate of the total water [mm/hour] and the absolute values of increase of the x-tilt (LTS) residuals [mas]

After the previous analysis, maybe interesting can be also the correlations between the rates of water with the absolute values of the drops of y-tilt residuals and increase of x-tilt residuals. After performing also that, we find that the correlation coefficients result to be negative 0.26± 0.32 with a corresponding probability of P (T ≥ t) = 0.2187, and

positive 0.20± 0.37 with a corresponding probability of P (T ≥ t) = 0.303, respectively. Results are displayed in the following plots (Figs. 3.19 and 3.20).

Figure 3.19. Plot shows correlation, for all the studied 11 pure rain events, between the rate of the total water [mm/hour] and the absolute values of drops of the y-tilt residuals [mas]

Figure 3.20. Plot shows correlation, for the studied 9 pure rain events, between the rate of the total water [mm/hour] and the absolute values of increase of the x-tilt (LTS) residuals [mas]

3.2.4 Results and physical interpretation

The following table (Table 3.4) summarizes all correlation coefficients between the tilt residuals and the precipitation with the corresponding probabilities, and corresponding figures.

Correlation coefficients (%)	PURERAIN EVENTS		MIXED EVENTS Total water	
	Cum rain	*Figure*	water	*Figure*
LTS				
Δy-tilt	**77.7±21 (0.0024)**	*(3.8)*	-15±33 (0.3317)	*(3.9)*
Δx-tilt	58.3±31 (0.0518)	*(3.10)*	6±38 (0.4387)	*(3.11)*
iWT				
Δx-tilt	39.4±46 (0.2216)	*(3.12)*	2.5±50 (0.4813)	*(3.13)*

Table 3.4 Results from correlation analysis and the t-test distribution. The correlation coefficients with the probabilities are summarized and the corresponding figures. In the corresponding figures one can also see the regression parameters. Coefficients pointed by bold letters show correlations that have a significance level above 95%.

Results show that only for the pure rain events a significant correlation exists between the change in the y-tilt residuals and the amount of water intruding into the ground. For the mixed- rain and snow events the resulted correlations are insignificant. Generally, the correlation is larger for the y-tilt residuals than for the x-tilt residuals both for the pure rain and the mixed events. This may be due to the fact that the x-tilt data are noisier than the y-tilt data where the drop is much better detectable for all the events, while the x-tilt residual increase is not always clearly visible.

Concerning the correlations with the time-shifts, it can be seen that no significant correlation exists between the time shift and total amount of water for both the pure rain and the mixed events. However, the results indicate a significant correlation between the rates of total water and time shifts. The correlation results to be high (62.6%) for the pure rain events, as it is seen in the next table (Table 3.5). This means, the bigger the rate of water is (the more intense the precipitation is), the larger is the delay of the y-tilt residual decease with respect to the gravity residual increase.

Correlation Coefficients (%)	PURE RAIN EVENTS		RAIN & abnormal residuals EVENTS		MIXED EVENTS
	Cum rain	RATE	Cum rain	RATE	Total water
Time-shift	25.9±32 (0.2187)	**62.6±26 (0.0192)**	28.3±24 (0.1315)	**45.8±22 (0.0265)**	21.6±44 (0.3191)
Figures	3.14	3.15			3.16

Table 3.5 Results from correlation analysis between total amount of water and rates of water with time shifts. The correlation coefficients (%) with the corresponding results from the t-test distribution (probabilities) are seen. In the corresponding figures one can also see the regression parameters. Coefficients pointed by bold letters show correlations that have a significance level above 95%.

The question is, is there a possible explanation for that? This result could maybe explained if we turn back to our first observations of the signals where we detected this small increase in the y-tilt residuals before starting their decreasing route. This phenomenon, as previously explained, is maybe associated with some accumulation of water for only a short time interval somewhere in the vicinity of the observatory before intruding rapidly into its final place. The speculation made is the following: The more intense is the water falling (rate), the bigger appears to be this increase and the longer it takes for the y-tilt residual before starting to decrease. That's why the resulted time delays between the two residuals seem to be bigger. If this small increase is indeed responsible for the time delays then this phenomenon is maybe able to support a possible scenario of an underground big downhill cavity. However this scenario is extremely speculative right now and cannot be confirmed, as long as no gravity signal corresponded to this small increase of tilt has been observed. Furthermore, in order to certify the above speculation, a statistically relevant relation between this tilt increase and the water accumulation/rate of water has to be found and approved as well. At the current time, due to the fact that this effect is very small in combination with the low statistics, I do not quantify this assumption, but I mention it as an information for a possible future research.

Having concluded the interpretation of the results, it is important to clarify the following: as mentioned in the captions of Tables 3.4 and 3.5 in the corresponding figures, one can see also the linear regression parameters for the main cases. However the focus on this study is the total correlation rather than the regression. The main reason

for this choice is the lack of a large data sample, which induces low statistics as we can see at the errors on the aforementioned Tables. Another consequence of the low statistics is the fact that we cannot investigate the nature of the possible dependence between the variables (linear, polynomial, etc.). However, in the corresponding figures one can see the simplest choice (linear), keeping always in mind that the large errors of the correlations are translated to large errors of the slope.

3.2.5 Searching for conditions when a tilt event occurs

In my attempt to further investigate under which conditions a tilt event occurs, on top off what is already done we now focus on the 'main' precipitation dates after which a drop of the tilt residuals occurs. I decide to define them as 'main induced events' since I consider only these events that are mainly provoked by these precipitation dates. I have to remind here to the reader that the 5-day interval case study (before a tilt event) is previously analyzed and at this stage I select only the 'main' dates of precipitation within the aforementioned interval, hence the name 'main induced events'. For this analysis I chose 1- to 3-day intervals. Table 3.6 presents all these events with the corresponding dates and the same analysis as before is performed. The time which the gravity residuals start to increase, total amount of water and corresponding rates are already known and set in the table. It is also noted whether a gravity or tilt effect is present. One clear condition derived from this analysis is that, in order a drop of the y-tilt residual to occur, not less than 20mm of water has to be intruded into the ground. The rate of water as well has to be big enough. It is revealed that after each precipitation there is an effect in gravity residuals but, however, not in all tilt residuals. That means that the cumulative water has to be adequate in order to provoke a drop of the y-tilt. In this case it has to be at about 20 mm and less amount of water than that doesn't provoke a drop in the y-tilt residuals. That's an important result which indicates the possible scenario of a cavity which could exist somewhere there, in the vicinity of the observatory and when water of 20mm intrudes into it and fills it, it provokes the strain induced tilt and the deformation of the cavity. But of course, this is just a scenario which cannot exclude the possibility of other scenarios as well. However, I will attempt to get into more details about this and try to find out if such a cavity really exists. The following paragraph gives more insight about that.

EVENTS DATE	DATES	Gravity increase starting time	Duration of rain [hours]	Total cumulative water [mm]	Rate of water [mm/hour]	Gravity effect	Tilt effect
May 2016							
	3.05-4.05	4.05 at 7.00h	15	26	1,73	yes	*GAP*
2016.05.13	12.05-13.05	13.05 at 22.00h	21	27	1,28	yes	yes
June 2016							
	1.06	1.06 at 13.00h	2	25	12,5	yes	*noisy*
2016.06.20	19.06-20.06	20.06 at 9.00h	9	30	3,3	yes	yes
2016.06.30	30.06	30.06 at 18.00h	4	43	10,75	yes	yes
July 2016							
2016.07.12	12.07	12.07 at 15.00h	2	23	1,5	yes	yes
	13.07-14.07	14.07 at 1.00h	6	24	4	yes	yes
2016.07.25	25.07-26.07	25.07 at 14.00h	1	32	32	yes	yes
August 2016							
	9.08-10.08	10.08 at 11.00h	13	27	2,07	yes	yes
Sept 2016							
2016.09.06	6.09-7.09	6.09 at 11.00h	8	35	4,38	yes	yes
Oktob 2016							
2016.10.20	19.10-21.10	20.10 at 8.00h	20	28	1,4	yes	yes
Nov 2016							
	6.11-7.11	6.11 at 19.00h	11	**17**	1,54	yes	**no**
July 2017							
	26.07-28.07	27.07 at 9.00h	12	29	2,41	yes	yes
Sept 2017							
	2.09-4.09	3.09 at 9.00h	13	28	2,15	yes	*noisy*
2017.09.20	19.09-21.09	19.09 at 23.00h	18	50	2,78	yes	yes
Okt 2017							
	8.10-9.10	9.10 at 1.00h	4	19	4,75	yes	GAP
	22.10-24.10	23.10 at 23.00h	21	40	1,9	yes	yes
2017.10.27	27.10-28.10	27.10 at 11.30h	6	35	5,83	yes	yes
Nov 2017							
	11.11-13.11	12.11 at 17.00h	15	**9**	0,6	yes	**no**

Table 3.6. The 'main induced events' are shown. First column presents the 'main' dates of precipitation which induce these events. Second column gives the time that the gravity residuals start to increase. Duration of rain [hours], cumulative rain [mm] and the rate of water [mm/hour] are again estimated. Last columns present if there is a gravity or tilt effect in each of these main events.

3.2.6 The cavity scenario

As mentioned before, in this paragraph, I try to give some explanations about the sources which can affect the tiltmeters, and provoke such big drops in their residuals and one scenario leads to the existence of a possible cavity near the observatory. In such a case, assuming a purely Newtonian source, a unique spherical cavity (one source) is assumed for simplicity and there is a trial to estimate the possible location, size and depth of such a cavity which provokes the great drops in the y-tilt residuals. In my attempt to estimate where the cavity can be located, it is really important to understand the geometry of the area. In the next figure (Fig. 3.21) the tunnel of the Conrad observatory is shown again and the location of the two sensors, SG and LTS-tiltmeter. The defined coordinate system is a (x, y, z) plane with the x-axis denoting the East-West direction, the y-axis the North-South direction and the z-axis pointing to the Earth and defining the gravity vector.
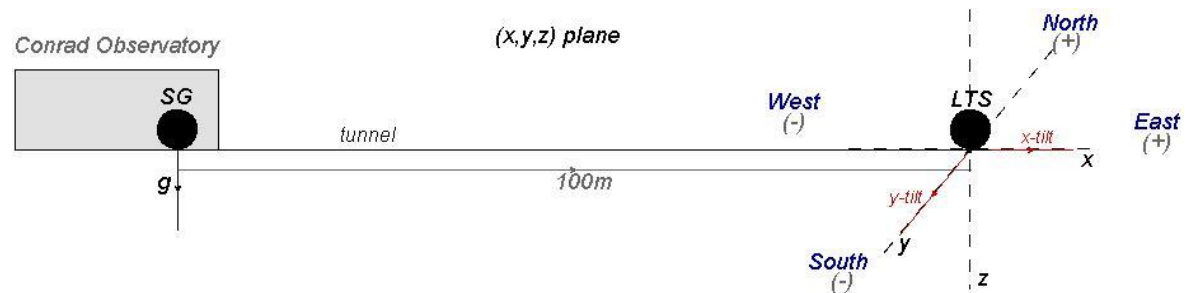
Figure 3.21. The 3D geometry of the Conrad observatory – (x, y, z) plane

If assumed that the cavity exists under the SG sensor, the Newton law can be applied:

$$g = \frac{GM_c}{r^2} \implies M_c = \frac{g\,r^2}{G} \quad (3.1)$$

With the radius of the spherical cavity being,

$$R = \sqrt[3]{\frac{3V}{4\pi}} \qquad (3.2)$$

Thus, a first estimation of the mass of this possible cavity can be made: Given that the gravitational constant is *G=6.67x10^-11 Nkg^-2m^2* and choosing the maximum value of the g of the gravimeter, *g=5 × 10^{-8} m/s^2*, the possible mass of the cavity in respect to some distance can be theoretically estimated. What the results display is that in a possible distance for example of 20 meters from the observatory, the mass of this spherical cavity is 3x10^5 kg and its radius is 4.15 meters. Going to larger distances the mass is going to become bigger and its radius as well. The results are displayed in

Appendix VII (Cavity scenario 1). However, such a scenario (one source under the SG) contradicts the fact that the x-tilt indication after a rain event is towards the East and not towards the SG (West).

As a result, I consider the scenario where the cavity is somewhere from the LTS to the East, as shown in figure 3.22, with coordinates (c_x, c_y, c_z). In the 3D-space geometry it will have a distance r_{LTS} from the LTS and r_{SG} from the SG. Before applying the specific constraints/approximations of the problem I show the more general approach. Wherever this cavity is located, the distance from the SG and the LTS is

$$r_{LTS} = \sqrt{(c_x - LTS_x)^2 + (c_y - LTS_y)^2 + (c_z - LTS_z)^2} ,$$
$$r_{SG} = \sqrt{(c_x - SG_x)^2 + (c_y - SG_y)^2 + (c_z - SG_z)^2} \qquad (3.3)$$

, where the LTS_i, SG_i are the coordinates of the LTS and SG respectively. The gravitational field created by this cavity affects both the LTS and the SG.
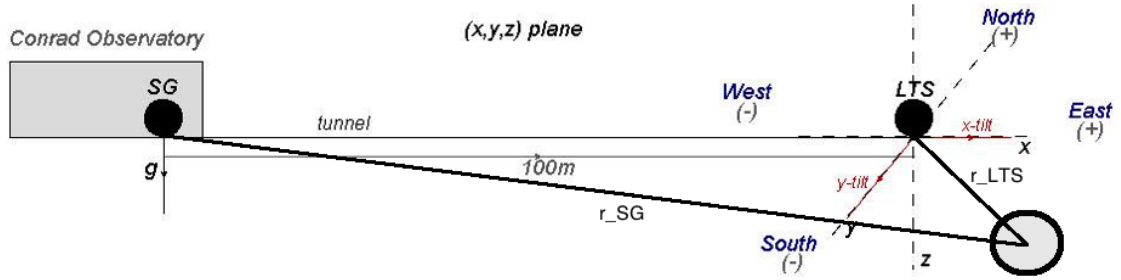
Figure 3.22. The 3D geometry of the Conrad observatory – (x, y, z) plane with the assumed cavity

Keeping in mind that the LTS is sensitive to the (x, y) plane and the SG to the z direction, one can decompose the three components using for the (x, y) ones the gravitational field effect to the LTS and for the z one the effect to the SG. It is

$$g_x = \frac{GM_c(c_x - LTS_x)}{r_{LTS}^3} , \quad g_y = \frac{GM_c(c_y - LTS_y)}{r_{LTS}^3} , \quad g_z = \frac{GM_c(c_z - SG_z)}{r_{SG}^3} \qquad (3.4)$$

As a next step from the tilt indications θ_x, θ_y that correspond to an event one can get a relation between the c_x, c_y coordinates. Once we define the coordinate system, the coordinates LTS_i, SG_i will be known in any case, but for now I keep them as parameters.

Focusing first on the LTS and in order to clarify more the 3D-space geometry of the area I draw it from the horizontal aspect of view ((x, z) plane) setting the y-tilt pointing

46

out of the page to the direction of South. The Earth gravity field g_0 points naturally down to the center of the Earth (Fig. 3.23). The angle of the x-tilt component can be now defined, θx, as:

$$tan\theta_x = \frac{g_x}{(g_0+g_z^{LTS})} \implies g_x = (g_0 + g_z^{LTS})tan\theta_x \qquad (3.5)$$
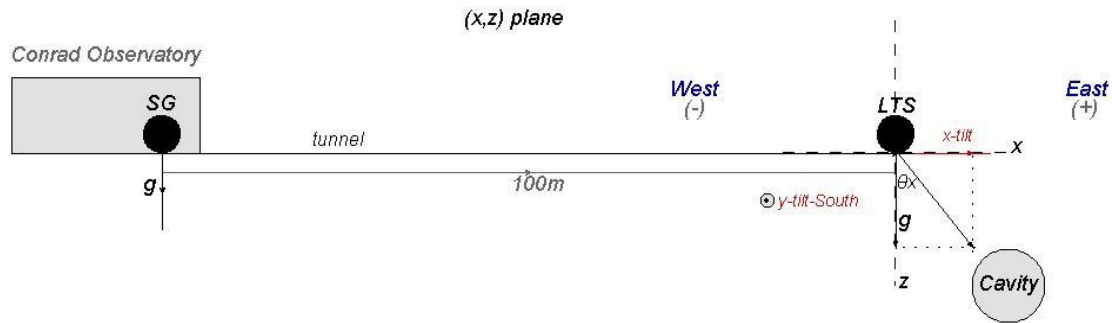
Figure 3.23. Horizontal view of the Conrad observatory – (x, z) plane

Similarly, I do the same for the (y, z) plane in figure 3.24. In this figure we have the angle in the North-South direction (y-tilt).
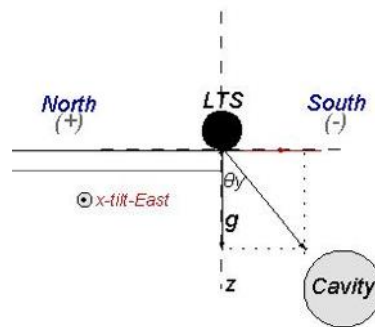
Figure 3.24. View of Conrad observatory in the (y, z) plane

The angle of the y-tilt component can be defined, θy, as:

$$tan\theta_y = \frac{g_y}{(g_0+g_z^{LTS})} \implies g_y = (g_0 + g_z^{LTS})tan\theta_y \qquad (3.6)$$

In both equations 3.5, 3.6, the g_z^{LTS} is the contribution of the cavity field to the LTS in the vertical axis. Keeping the approach general from equations 3.5, 3.6 we can get the relation f between the c_x, c_y coordinates in combination with equation 3.4. It is

$$\frac{(c_x-LTS_x)}{(c_y-LTS_y)} = \frac{g_x}{g_y} = \frac{tan\theta_x}{tan\theta_y} \implies c_y = f c_x \qquad (3.7)$$

I remind to the reader that the LTS_i are known parameters, so the factor f is calculable. Using this equation, the new form of 3.3 becomes

$$r_{LTS} = \sqrt{(c_x - LTS_x)^2 + \left(fc_x - LTS_y\right)^2 + (c_z - LTS_z)^2} \, ,$$

$$r_{SG} = \sqrt{(c_x - SG_x)^2 + (fc_x - SG_y)^2 + (c_z - SG_z)^2} \qquad (3.8)$$

Combining equations 3.8, 3.4 one gets the general form of the set of equations that are necessary to use the three measurements from the gravimeter and the tiltmeters.

Starting from this general point we now focus on our case and approximate in order to do a specific case study. First of all, for convenience and without losing generality, we use a coordinate system [x (East), y (South), z (vertical)] which originates at the LTS $LTS_i = (0,0,0)$. We get

$$g_x = \frac{GM_c c_x}{r_{LTS}^3} \, , \;\; g_y = \frac{GM_c c_y}{r_{LTS}^3} \, , \;\; g_z = \frac{GM_c(c_z - SG_z)}{r_{SG}^3} \qquad (3.9)$$

$$r_{LTS} = \sqrt{(1 + f^2)c_x^2 + c_z^2} \, , r_{SG} = \sqrt{(c_x - SG_x)^2 + (fc_x - SG_y)^2 + (c_z - SG_z)^2}$$
(3.10)

Focusing now on the observatory geometry, we can see the setting in figure 3.25.
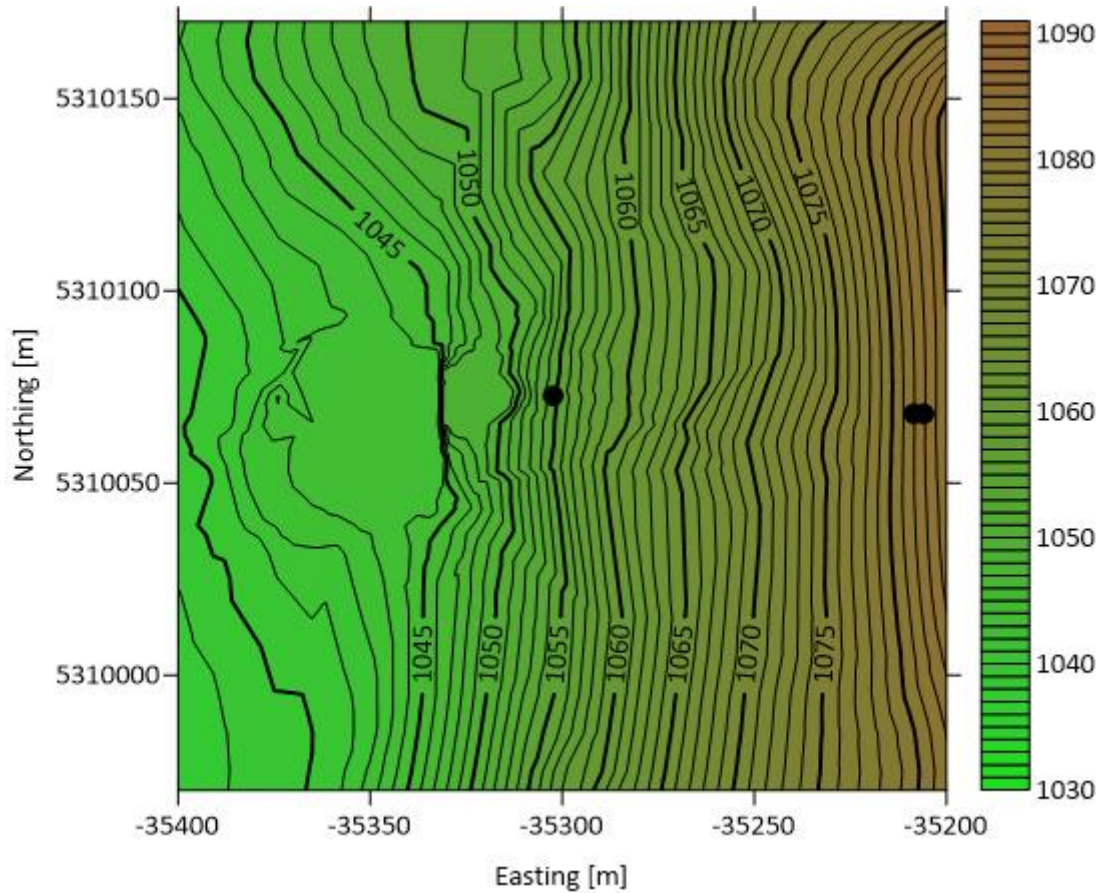
Figure 3.25. Topographic map of the Conrad observatory

In this figure the single dot is the SG and the double dot is the LTS locations. We can see that the direction SG-LTS is almost aligned to the WEST-EAST direction (which is the $+x$) and the NORTH-SOUTH ($+y$) is almost perpendicular to the SG-LTS (as already shown in figures 3.21-3.23). This is the first approximation that we do. As a result the coordinates SG_i become (-100, 0, 0). Furthermore, as mentioned before, after every rain event the x-tilt indication is towards the East and the y-tilt indication is towards the South. So I assume the cavity to be restricted in the $(+x, +y)$ part of the (x, y) plane, as shown in figure 3.26 below.
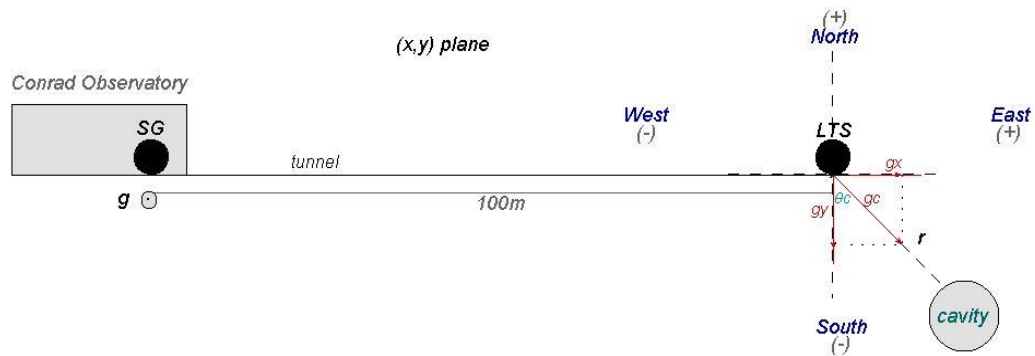
Figure 3.26. Vertical view of the Conrad observatory – (x, y) plane

We consistently chose the event with the maximum indications in all the three instruments (SG, LTS-y, LTS-x) because in this event the maximum amount of water is accumulated within the assumed cavity, so our radius R estimation will be safer. This results to the values $(5 \times 10^{-8}, \sim -200, \sim 20)$ in (m/s^2, mas, mas). Note that the -200 is actually +200 towards the south. Using the equation 3.7 and the specific values we can get the factor f between the c_x, c_y. It is

$$\frac{c_x}{c_y} = \frac{g_x}{g_y} = \frac{tan\theta_x}{tan\theta_y} \approx \frac{\theta_x}{\theta_y} = \frac{1}{10} \rightarrow c_y = 10c_x \qquad (3.11)$$

The aim now is to see whether these equations can be combined in order to constrain this scenario.

Using this result, we can rewrite the third component for the gravitational field effect on the SG. It is

$$g_z = \frac{GM_c c_z}{r_{SG}^3} = \frac{GM_c c_z}{(\sqrt{(c_x+100)^2 + 100c_x^2 + c_z^2}\ )^3} \qquad (3.12)$$

Knowing the value of g_z that corresponds to this event (5×10^{-8} m/s^2) we can calculate the mass M_c of the water in this spherical cavity and then the radius R through

the volume V. Solving this equation for M_c and spanning values $1 \leq c_z \leq 200$ and $1 \leq c_x \leq 20$ ($\rightarrow 10 \leq c_y \leq 200$) I get the plot presented in figure 3.27.
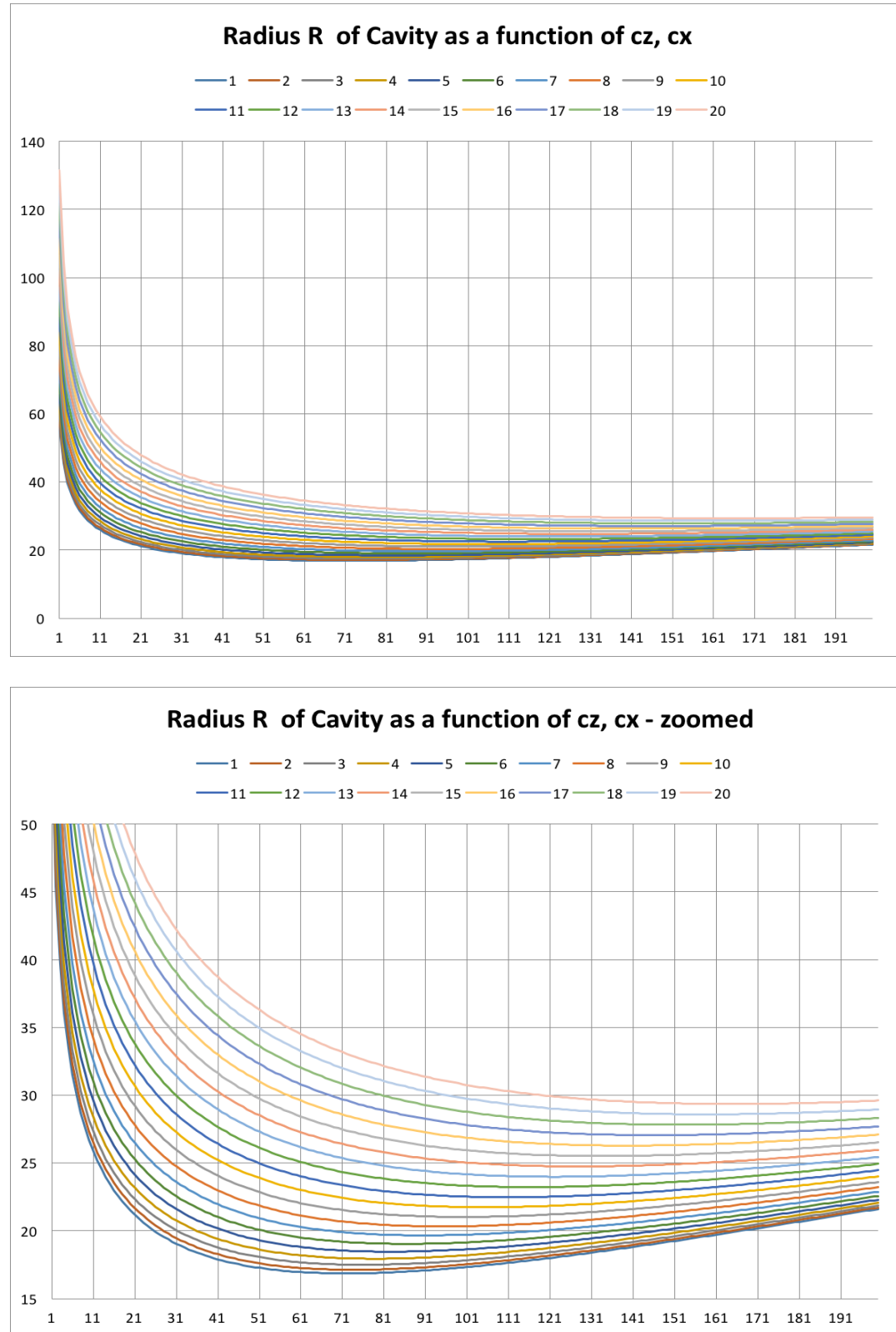
Figure 3.27. Radius R of the cavity. Each color corresponds to a different c_x. In the x axis we see the c_z and in the y axis the radius R. All the units are in meters.

From the above equation the mass M_c is calculated given the c_z, c_x. From the mass M_c the volume V can be calculated given the density of the water ($\rho = 1000$ kg/m^3). Finally, from the volume V, assuming spherical cavity, one can get the radius R. In the above plot in figure 3.27 one can see this dependence of the R from the c_z, c_x.

The criteria to accept or exclude solutions are now analyzed. First of all, now that we have for a given mass M_c the values c_z, c_x we can go back to equations 3.5, 3.6. In all the cases we consider it is $g_0 + g_z^{LTS} \approx g_0$, since the disturbance from the cavity is always very small compared to the g_0 of the Earth. So from the $c_{x,y}$ we can calculate the $g_{x,y}$ since

$$g_x = \frac{GM_c c_x}{r_{LTS}^3} \ , \ g_y = \frac{GM_c c_y}{r_{LTS}^3} \qquad (3.12)$$

From this, using the 3.5, 3.6 we get the

$$\theta_x = \arctan(\frac{g_x}{g_0}), \theta_y = \arctan(\frac{g_y}{g_0}) \qquad (3.13)$$

So now we compare for each case the resulting angles to the values ($\theta_y = 200, \theta_x = 20$). Of course these values are measurement results so we allow some variation of $\pm 25\%$. So the first condition is to accept the resulting M_c only if $150 \leq \theta_y \leq 250$ (the corresponding θ_x condition does not add new information, since they are related). From this condition we get the plot in figure 3.28, which is zoomed to the relevant region.
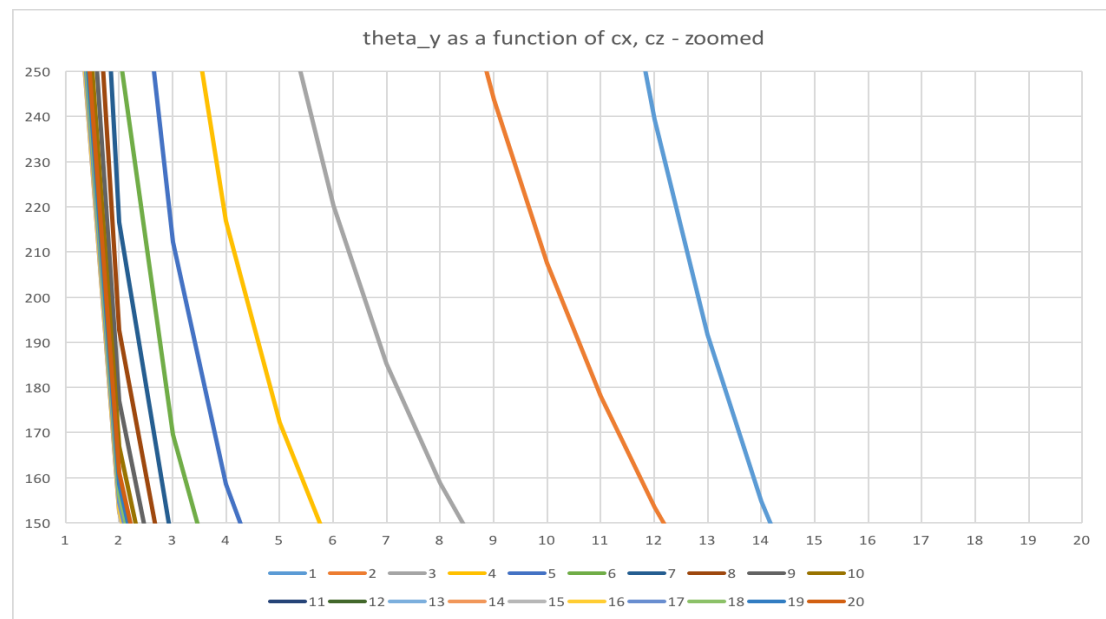
Figure 3.28. Angle $\theta_y(c_x, c_z)$. Each color corresponds to a different c_x. In the x axis we see the c_z and in the y axis the θ_y in mas.

From the above plot we apply constrain $c_z \leq 15$ and can exclude the higher values for c_z, since they would give values of θ_y outside of the allowed region.

The second criterion we can use is the fact that the radius of the cavity must be smaller than its distance from the LTS and the SG. So the LTS and the SG are not within the cavity. Since in our specific case it is always $r_{LTS} < r_{SG}$ it is enough to apply the condition $R < r_{LTS} \Longrightarrow r_{LTS} - R > 0$. Using this condition and showing the $c_z \leq 15$ values the resulting plot is in figure 3.29.
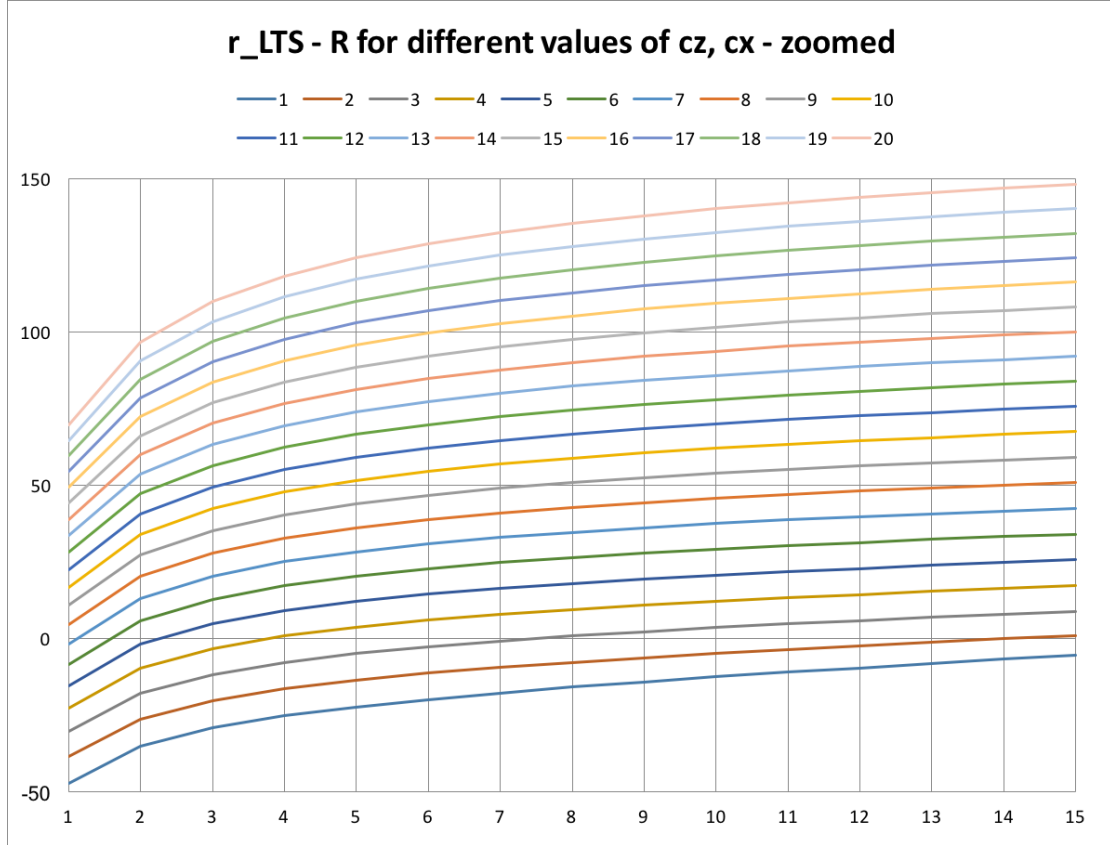
Figure 3.29. Difference $(r_{LTS} - R)$ as a function of c_x, c_z. Each color corresponds to a different c_x. In the x axis we see the c_z and in the y axis the difference.

From figure 3.29 we can see that the allowed values for c_x are $c_x \geq 3$, since the first two values give negative difference for every c_z between 1 and 15. Furthermore for lower than 15 c_z values the constraints for c_x differ. We have $c_z = 1 \rightarrow c_x \geq 8$, $c_z = 2 \rightarrow c_x \geq 6$, $c_z = 3,4 \rightarrow c_x \geq 5$, $c_z = 5,6,7 \rightarrow c_x \geq 4$.

Up to now I have kept the relation $c_y = 10\,c_x$ fixed. However, this factor has also an uncertainty. So I redid the same steps with $f = 8$ and then $f = 12$. This gives an uncertainty on the final estimations which become $c_x \geq 2.5 \pm 1$ and $c_z \leq 15 \pm 1$ and these are the final constraints for this scenario (there are also changes in the c_x lines,

which are shown in the appendix VII (Cavity scenario 2)). For these constraints and their uncertainties I also give the corresponding limits on the radius R of the cavity. The limits are $25\{+1, -1\} < R < 131\{+20, -18\}$ m. In these uncertainties the lower limits come from the $f = 8$ and the maximum from the $f = 12$. The radius R after the constraints is shown in figure 3.30 below.

Radius R of Cavity as a function of cz, cx - after constraints
25 < R < 131 m
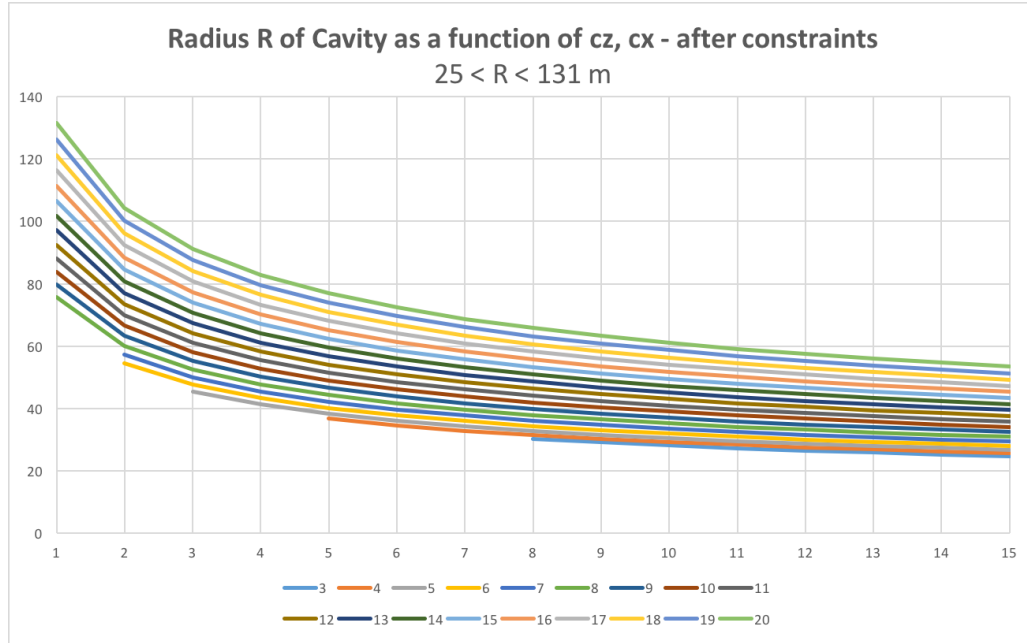
Figure 3.29. Difference $(r_{LTS} - R)$ as a function of c_x, c_z after the final constraints. Each color corresponds to a different c_x. In the x axis we see the c_z and in the y axis the difference.

Before going to the conclusions I summarize the main results of this part: It was shown, that the assumed unique cavity cannot be deeper than ~15 m. It cannot be closer to the LTS than ~2 m to the East direction and than ~20 m to the South direction. The radius of this cavity is found to be between 25 and 131 meters. These results alone do not exclude the one-point source scenario but constrain it. We have established the fact that after each precipitation the y-tilt indications are towards the South direction (negative values of y-tilt), which is perpendicular to the line SG-LTS (East-West). Furthermore, the x-tilt indications are towards the East direction (positive values of x-tilt), which is the opposite of the LTS-SG direction (East). This means that the indication from the LTS as a total (regardless the previous numerical approximations/hypotheses) is that the deformation is not towards the SG.

4. Conclusions – Further research

After completing the analysis of all the available events and before reaching my final conclusions I first would like to outline a summary of the main results in this work. First of all, after the precise observation of the gravity residual, it is noticed that after a precipitation event (either pure rain or mixed-rain and snow) the former increases, something which indicates that some amount of water is accumulated under the SG sensor. Thus, it is verified that there is a correlation between the gravity and the hydrological processes around the Conrad observatory, meaning that gravity residuals clearly reflect the hydrological mass transport around the area of Trafelberg. Given this already established result in this thesis I focused in searching for similar occurrences in the tilt meters. In what follows, I report my main results of this research.

1. The pure rain from the mixed- rain and snow events were separated and independent correlation analyses were carried out: first for the pure rain and secondly for the mixed events. The results show that there is a significant correlation for the pure rain events resulting to a correlation coefficient of 77.7±21% with a confidence level at 99.76%.

2. It is found during the analysis of events that a time-shift (time delay) between the gravity and tilt residuals exists. Gravity residuals first start increasing and after a delay of about 1 to 6 hours, the tilt residuals start decreasing.

3. There is a high significant resulted correlation between the rate of water and the time-shift [Table 3.5]**,** which was found to be 62.6±26% (98.08% significance level that the correlation is not a fluctuation). This correlation implies that the more intense is the water falling (rate), the longer it takes for the y-tilt residual before starting to decrease until reaching its minimal value, or in other words the bigger the time delay between the gravity and tilt residuals.

4. One other important result found while searching for the conditions under which a drop of a tilt residual can occur (paragraph 3.2.5) is that accumulated water less than 20mm doesn't provoke a tilt-event. That's a clear condition which has to be satisfied in order to observe a drop of a tilt residual**:** at least 20mm of water has to be accumulated in top of topography and then absorbed into the ground.

5. After setting some approximate values of our data sample, for the two angles, angle of the x-tilt, θx, and angle of the y-tilt, θy, it is true in a first approximation that,

$$\theta_y \gg \theta_\chi \rightarrow \theta_y \approx 10\theta_x$$

, which means that the y-tilt is bigger at about 10 times than the x-tilt. This result is important, because it gives a clear hint, that something affects the y-tilt (in the North-South direction) more than it does for the x-tilt (East-West direction). This angular decomposition is done within the cavity scenario, but the y-tilt (towards South) and x-tilt (towards East) indications are model independent results.

6. As already described in the paragraph 3.2.2 (Analysis of events), it has been also observed that small increases in the y-tilt residuals exist during precipitation and before their final drops. This could maybe indicate that the water maybe is firstly accumulated somewhere else in the vicinity of North and after the end of precipitation is following its final route to the South.

7. In my attempt to 'catch' sight of a possible hidden cavity in the vicinity of the observatory, I tried to estimate the possible location, size and mass of such a cavity. For simplicity I assume that the cavity is spherical. After each precipitation event the change in the tilt residuals indicates that the amount of water is accumulated somewhere in between the South and East direction and, being more specific, more oriented to the South. After constraining this scenario, the assumed cavity cannot be deeper than ~15 m, cannot be closer to the LTS than ~2 m to the East direction and than ~20 m to the South direction. Moreover, the radius results to be between 25 and 131 meters.

After the above results it can be claimed with certainty that the hydrological processes are related to the gravity and tilt residuals. Given the aforementioned correlation (Result 1) it can be concluded that the tilt residual anomalies are triggered by the same hydrological processes around Trafelberg. In my attempt to find and understand which are these true physical processes occurring in the vicinity of the Conrad observatory, I can now start defending or rejecting the already mentioned, during this thesis, possible scenarios.

My first scenario focuses on the idea of the base plate model which is in accordance with the gravity residuals: water is accumulated under the building of the observatory after precipitation and this triggers the gravity residual anomalies. This scenario, however, cannot explain the triggered tilt residual anomalies. I remind to the reader, that the tiltmeters are located 100m far away from the SG sensor, so, if the base plate model holds for the SG-residuals, it cannot be supported as well for the LTS and iWT-

residuals. Moreover, there is a second clue which can confirm the above evidence. If the residuals changed at the same time, then it could be claimed that the signals are purely Newtonian, which would further support the base plate model. But the found result with the time delays between the gravity and y-tilt residuals (Result 2) complicates the picture and strongly indicates that something else occurs under the sensors and triggers this specific behavior of the tilt signatures.

The second scenario focuses on the idea of a possible cavity existed in the surroundings of the observatory, as in detail described in the last paragraph (Paragraph 3.2.6). This assumed cavity is more oriented to the South (Result 5), and its location and size are restricted (Result 7). With this analysis this scenario is not excluded. However, the time delay in the response between the SG and the LTS (Result 2) strongly discourages this scenario, unless it can be explained otherwise.

The above scenario is based on the assumption that the tilts are purely gravitational. However, the previous modelling constrains/discourages a purely Newtonian source of the observed tilts. This means that there could be local deformation somewhere in the tunnel, or else strain-induced tilt, and thus, the 'cavity effect' comes up. The tilt signals are stronger in the North-South than in the East-West direction (Result 5) which is a strong indication for the 'cavity effect'. I remind to the reader, that the North-South direction is perpendicular to the SG-LTS along-tunnel direction, which strongly supports this effect. Such a conclusion would be in very good agreement with the paper [11], which focuses on this effect as explained in the introduction. Moreover, the result about the time delays (Result 2) supports the non-purely Newtonian source. Water needs a little time to get accumulated under the SG, that's why we observe a spontaneous increase in the SG residuals. That's not, however, the case for the LTS, which is located inside the tunnel, 100 meters apart from the SG, which means that water needs much more time to travel from the top of topography until getting accumulated into the ground.

From all the above, it is understood that one possible scenario may be the 'cavity effect'. On the other hand, the possibility of existence of a unique cavity cannot be excluded, as well. More complicated scenarios like multiple sources scenario (more than one cavity) or combinations of cavity and induced strain effects may exist and are able to explain the phenomenon. For future investigation in order to find the true hydrological processes in Trafelberg and to further explore the results 3, 4, 6, it is necessary to proceed to other methods. The problem of the 'cavity effect' can be answered by applying the Finite Element Modelling method or the Boundary Element Method.

56

Under the light of these methods, the important features of the cavity can be illustrated and the topographic effects around Trafelberg can be better studied. Other geophysical methods like the Electrical Resistivity Tomography (ERT) or GPS measurements could be applied, as well. The results and conclusions of the current thesis can be used as a basis for the aforementioned further research.

Finally, the current motivation to find a clear residual signal, free of tides and additional hydrological effects, is expected to encourage the following researchers, who will deal with the specific topic. This will lead to revealing some very interesting geodynamical phenomena, which previously were 'hidden', and to find out the true geophysical and tectonic processes occurring under the Conrad Observatory, in Trafelberg of Vienna.

Bibliography

[1] P. Krause, M. Naujoks, M. Fink and C. Kroner, "The impact of soil moisture changes on gravity residuals obtained with a superconducting gravimeter," *Journal of Hydrology,* vol. 373, no. 1-2, pp. 151-163, 2009.

[2] L. Longuevergne, J. Boy, N. Florsch, D. Viville, D. Ferhat, P. Ulrich, B. Luck and J. Hinderer, "Local and global hydrological contributions to gravity variations observed in Strasbourg," *Journal of Geodynamics,* vol. 48, no. 3-5, pp. 189-194, 2009.

[3] B. Creutzfeldt, A. Güntner, H. Thoss, B. Merz and H. Wziontek, "Measuring the effect of local water storage changes on in situ gravity observations: Case study of the Geodetic observatory Wettzell, Germany," *Water Resources Research,* vol. 46, no. 8, p. 15, 2010.

[4] B. Creutzfeldt, A. Güntner, T. Klügel and H. Wziontek, "Simulating the influence of water storage changes on the superconducting gravimeter of the Geodetic Observatory Wettzell, Germany," *Geophysics,* vol. 73, no. 6, p. 10, 2008.

[5] M. Zadro and C. Braitenberg, "Measurements and interpretations of tilt-strain gauges in seismically active areas," *Earth-Science Reviews,* vol. 47, no. 3-4, pp. 151-187, 1999.

[6] G. Dal Moro and M. Zadro, "Subsurface deformations induced by rainfall and atmospheric pressure: Tilt and strain measurements in the NE-Italy seismic area," *Earth and Planetary Science Letters,* vol. 164, no. 1-2, pp. 193-203, 1998.

[7] D. C. Agnew, "Before PBO: An overview of continuous strain and tilt measurements in the United States," *Journal of the Geodetic Society of Japan,* vol. 53, no. 2, pp. 157-182, 2007.

[8] L. Longuevergne, N. Florsch, F. Boudin, T. Vincent and M. Kammenthaler, "Inclinometry and geodesy: an hydrological perspective," *GGP Workshop, Jena, Germany,* p. 12, 2006.

[9] L. Brimich, M. Bednarik, V. Bezak, I. Kohut, D. Ban, I. Eper-Papai and G. Mentes, "Extensometric observation of Earth tides and local tectonic processes at the Vyhne Station, Slovakia," *Contributions to Geophysics and Geodesy,* vol. 46, no. 2, pp. 75-90, 2016.

[10] M. Queitsch, G. Jentzsch, A. Weise, H. Ishii and Y. Asai, "Pumping Induced Pore Pressure Changes in Tilt Measurements Near a Fault Zone in Mizunami, Japan," *International Association of Geodesy Symposia,* vol. 139, pp. 113-118, 2014.

[11] J. C. Harrison, "Cavity and topographic effects in tilt and strain measurement," *Journal of Geophysical Research,* vol. 81, no. 2, pp. 319-328, 1976.

[12] G. C. P. King and R. G. Bilham, "Tidal Tilt Measurement in Europe," *Letters to Nature,* vol. 243, no. 5402, pp. 74-75, 1973.

[13] V. Dehant, P. Defraigne and J. Wahr, "Tides for a convective Earth," *Journal of Geophysical Research B1,* vol. 104, pp. 1035-1058, 1999.

[14] U. J. Itsueli, R. G. Bilham, N. R. Goulty and G. C. P. King, "Tidal Strain Enhancement Observed Across a Tunnel.," *Geophysical Journal of the Royal Astronomical Society,* vol. 42, no. 2, pp. 555-564, 1975.

[15] P. Kostecky and I. Kohut, "Modelling of the rock structure stress field near the cavities and estimation of the cavity effect influence on the tidal measurements," *Mathematics and Computers in Simulation,* vol. 50, no. 1-4, pp. 205-214, 1999.

[16] L. Brimich and M. Hvozdara, "The boundary integral calculation of tidal displacements of trapezoidal gallery," *Contributions of the Slovak Academy of Sciences, Geophysical Institute,* vol. 27, pp. 68-80, 1997.

[17] T. Jacob, J. Chéry, F. Boudin and R. Bayer, "Monitoring deformation from hydrologic processes in a karst aquifer using long-baseline tiltmeters," *Water Resoures Research,* vol. 46, no. 9, p. 18, 2010.

[18] N. Lesparre, F. Boudin, C. Champollion, J. Chery, C. Danquigny, H. Cheng Seat, M. Cattoen, F. Lizion and L. Longuevergne, "New insights on fracture deformation from tiltmeter data measured inside the Fontaine de Vaucluse karst

system," *Geophysical Journal International,* vol. 208, no. 3, pp. 1389-1402, 2017.

[19] C. Champollion, S. Deville, J. Chéry, E. Doerflinger, N. Le Moigne, R. Bayer, P. Vernant and N. Mazzilli, "Estimating epikarst water storage by time-lapse surface-to-depth gravity measurements," *Hydrology and Earth System Sciences,* vol. 22, no. 7, pp. 3825-3839, 2018.

[20] A. Watlet, O. Kaufmann, A. Triantafyllou, A. Poulain, J. Chambers, P. Meldrum, P. Wilkinson, V. Hallet, Y. Quinif, M. Van Ruymbeke and M. Van Camp, "Imaging groundwater infiltration dynamics in the karst vadose zone with long- term ERT monitoring," *Hydrology and Earth System Sciences,* vol. 22, no. 2, pp. 1563-1592, 2018.

[21] P. W. Williams, "The role of the epikarst in karst and cave hydrogeology: a review," *International Journal of Speleology,* vol. 37, no. 1, pp. 1-10, 2008.

[22] N. Goldscheider and D. Drew, Methods in karst hydrogeology, London, UK: Taylor & Francis group, 2007.

[23] T. Hermann, C. Kroner and T. Jahr, "Geoelectrical, strain and tilt investigations of hydrological processes at the broadband geodynamical observatory Moxa, Germany," *Journal of Applied Geophysics,* vol. 98, pp. 90-99, 2013.

[24] E. Serpelloni, F. Pintori, A. Gualandi, E. Scoccimarro, A. Cavaliere, L. Anderlini, M. Belardinelli and M. Todesco, "Hydrologically-induced karst deformation, insights from GPS measurements in the Adria-Eurasia plate boundary zone," *Journal of Geophysical Research: Solid Earth,* vol. 123, no. 5, pp. 4413-4430, 2017.

[25] E. Gilli, F. Boudin, L. Longuevergne, N. Florsch, J. Walch, A. Gomez, J. Depeyre and J. Marie, "Neotectonics and current hydrologically-induced karst deformation. Case study of the Plateau de Calern (Alpes-Maritimes, France)," *Geodinamica Acta,* vol. 23, no. 1-3, pp. 49-64, 2010.

[26] "Conrad Observatory," in *COBS Journal*, ZAMG: Central Institute for Meteorology and Geodynamics, Vienna, Austria, 2010, p. 20.

[27] Web source-1, "Wikipedia: The Conrad Observatory," 2019. [Online]. Available: https://en.wikipedia.org/wiki/Conrad_Observatory. [Accessed 29 05 2019].

[28] F. Blauensteiner, "Geodetic and Astronomic Measurements at the GMO," in *COBS journal Nr.4*, ZAMG: Central Institute for Meteorology and Geodynamics, Vienna, Austria, 2016.

[29] "Geophysical research for possible underground water reservoirs," in *ZAMG: Central Institute for Meteorology and Geodynamics*, Vienna, Austria, 2012, pp. 39-41.

[30] J. Hinderer, D. Crossley and R. J. Warburton, "Gravimetric Methods-Superconducting Gravity Meters," *Treatise on Geophysics,* vol. 3, pp. 65-122, 2007.

[31] N. Blaumoser, "20 years GWR tide gravimeter ZAMG 1995-2015," in *COBs Journal*, ZAMG: Central Institute for Meteorology and Geodynamics, Vienna, Austria, 2014-2015, p. 32.

[32] H. Ruotsalainen, D. Ban, G. Papp, R. Leonhardt and J. Benedek, "Interferometric Water Level Tilt meter at Conrad Observatory.," in *COBs Journal Nr.4*, ZAMG: Central Institute for Meteorology and Geodynamics, Vienna, Austria, 2016, p. 11.

[33] H. Ruotsalainen, "Interferometric Water Level Tilt Meter Development in Finland and Comparison with Combined Earth Tide and Ocean Loading Models," *Pure and Applied Geophysics,* vol. 175, no. 5, pp. 1659-1667, 2018.

[34] "The Laser Precipitation Monitor: Instructions for use," Göttingen, Germany, Adolf Thies GmbH & Co. KG, 2001, p. 66.

[35] Web source-2, "How does a rain gauge work?," attemptNwin, 31 05 2019. [Online]. Available: http://attemptnwin.com/answers/rain-gauge-work/. [Accessed 2019].

[36] B. Habel and B. Meurers, "A new tidal analysis of superonducting gravity observations in Western and Central Europe.," *Contributions to Geophysics and Geodesy,* vol. 44, no. 1, pp. 1-24, 2014.

[37] B. Meurers, "10 years SG gravity time series at Conrad observatory," Station report: 1st Workshop on the International Geodynamics and Earth Tide Service (IGETS), Potsdam (Germany), 2018.

[38] H. G. Wenzel, "The nanogal software. Earth tide data processing package ETERNA 3.30," *Bulletin d'Informations Marees Terrestres,* vol. 124, pp. 9425-9439, 1996.

[39] T. Klügel and H. Wziontek, "Correcting Gravimeters and Tiltmeters for Atmospheric Mass Attraction using Operational Weather Models," *Journal of Geodynamics,* vol. 48, p. 204, 2008.

[40] B. Meurers, "Gravity Monitoring with a superconducting gravimeter in Vienna," Institute of Meteorology and Geophysics, University of Vienna, 2001, p. 10.

[41] Web source-3, "International Earth Rotation and Reference Systems Service," 29 05 2013. [Online]. Available: https://www.iers.org/IERS/EN/Home/home_node.html. [Accessed 2019].

[42] M. Van Camp and P. Vauterin, "Tsoft: graphical and interactive software for the analysis of time series and Earth tides," *Computers & Geosciences,* vol. 31, no. 5, pp. 631-640, 2005.

[43] B. Meurers, "Environmental effects on gravity at Conrad Observatory, Austria," in *EGU General Assembly 2010: Geophysical Research Abstracts*, 2010.

[44] Web source-4, "T Distribution Calculator," 2019. [Online]. Available: https://stattrek.com/online-calculator/t-distribution.aspx. [Accessed 2019].

APPENDIX I

The pure rain events

event 2016.05.13

event 2016.06.20

event 2016.06.30

event 2016.07.12

event 2016.07.25

event 2016.09.06

event 2016.10.20

event 2017.09.20

event 2017.10.27

The mixed- rain and snow events

event 2016.10.06

event 2016.10.12

event 2016.11.16

event 2017.02.21

event 2017.03.18

event 2017.04.25

event 2017.04.30

event 2017.05.09

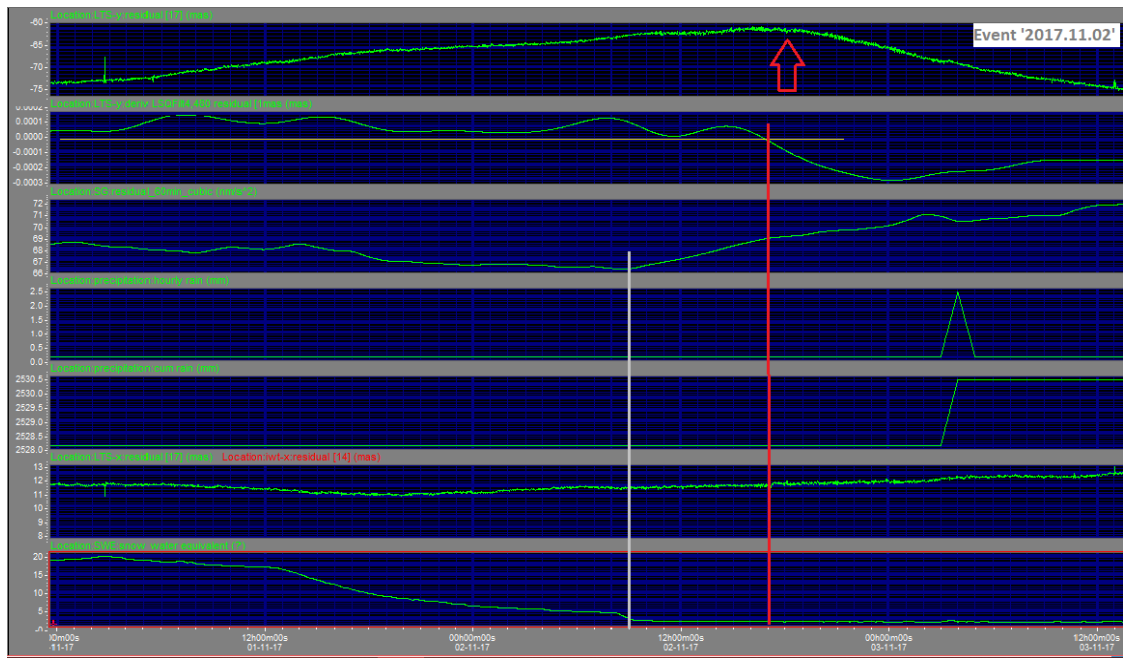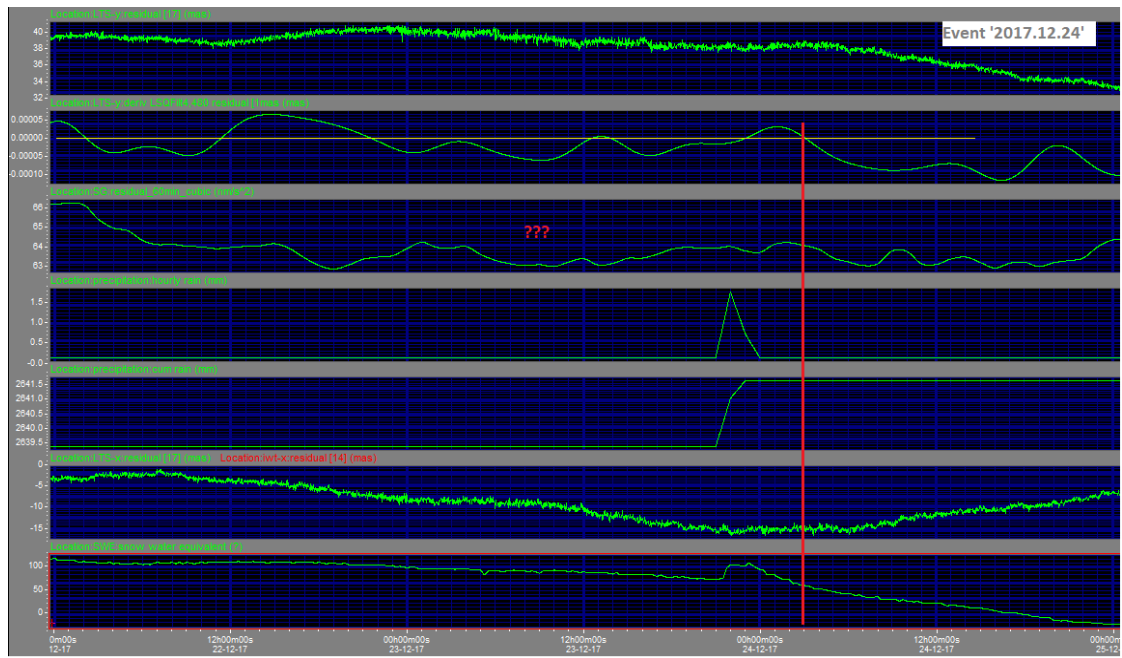event 2017.11.02

event 2017.11.21

event 2017.12.24
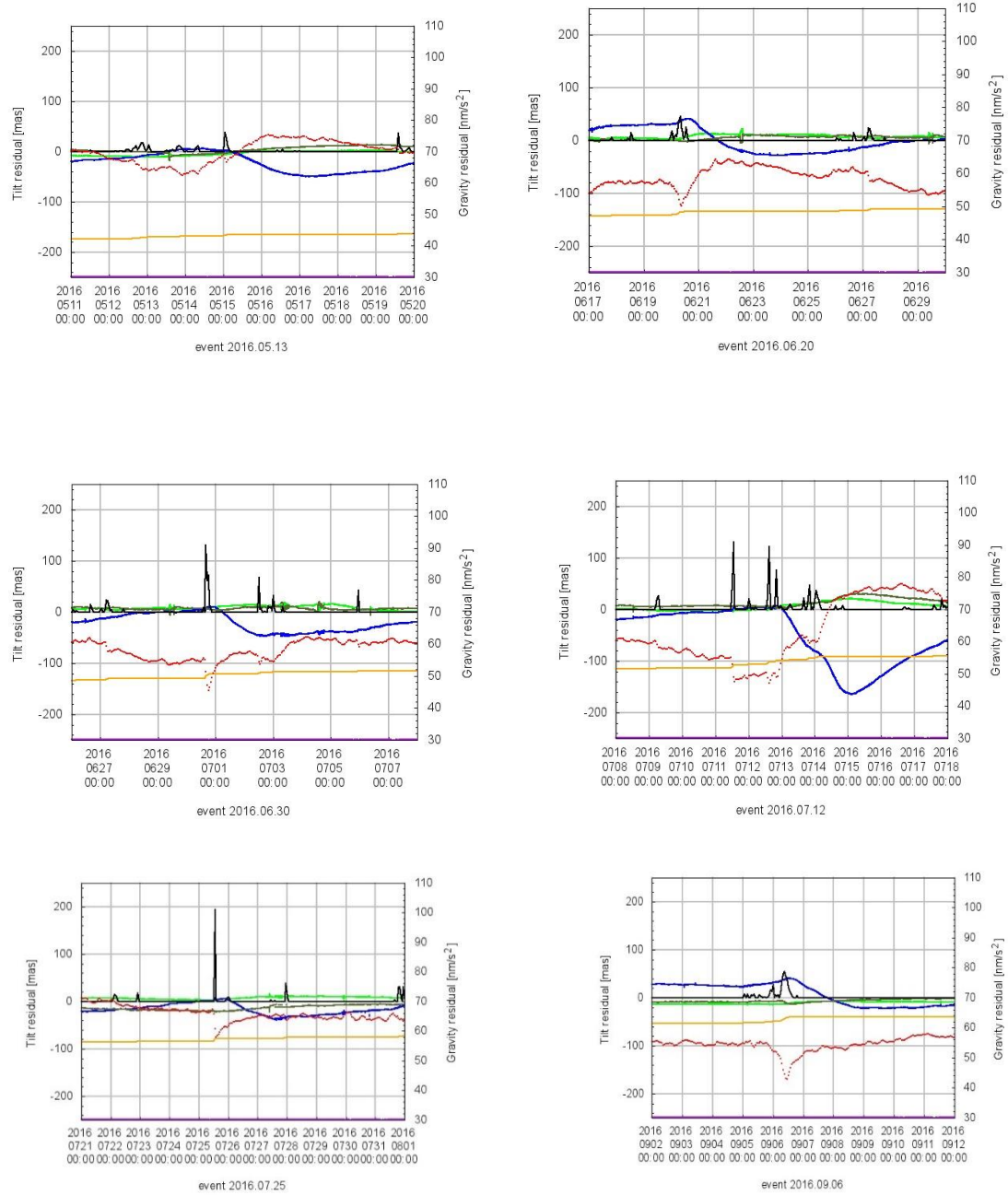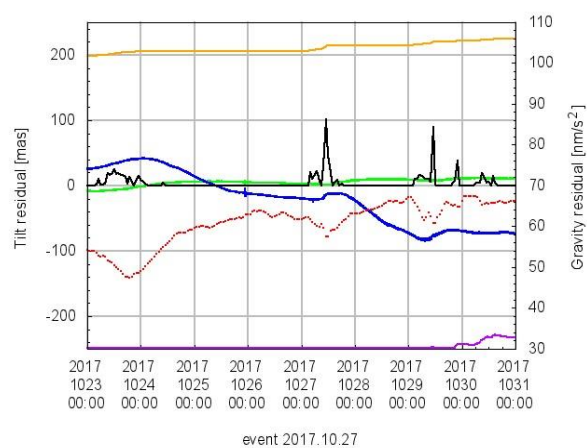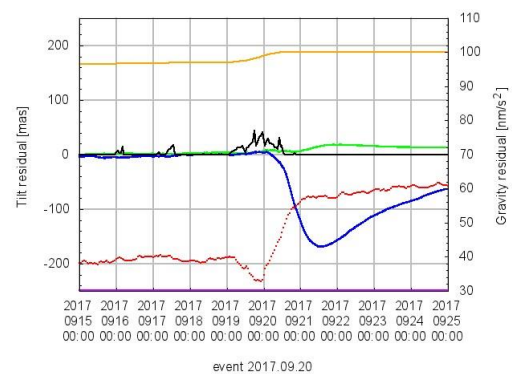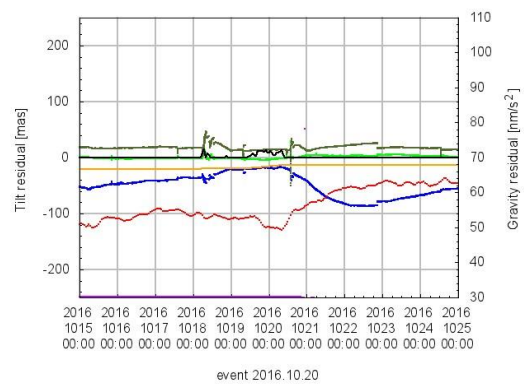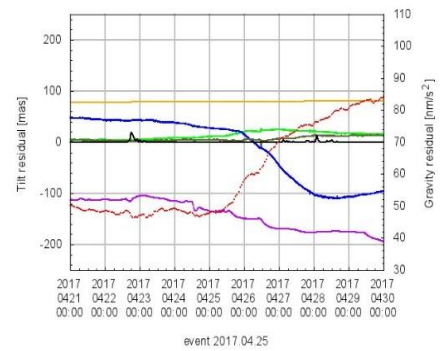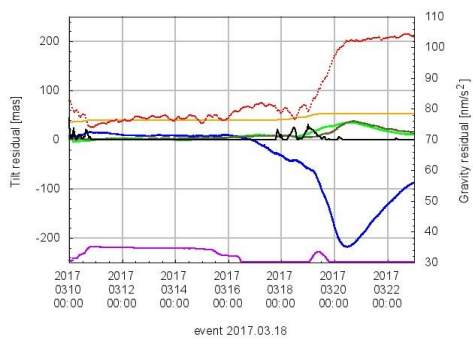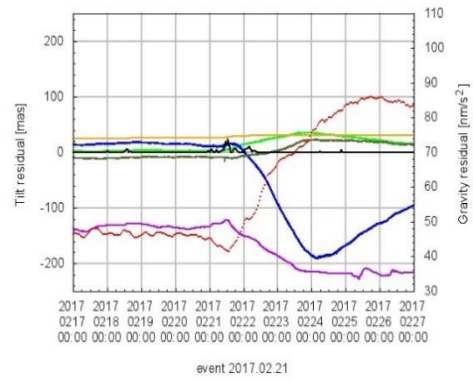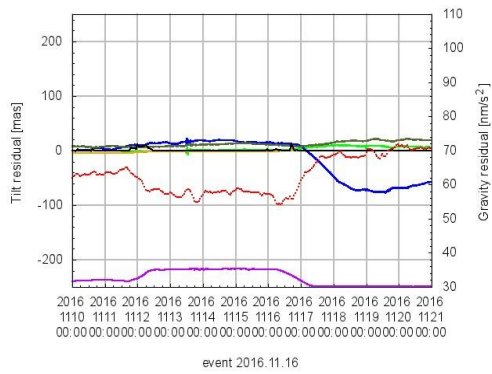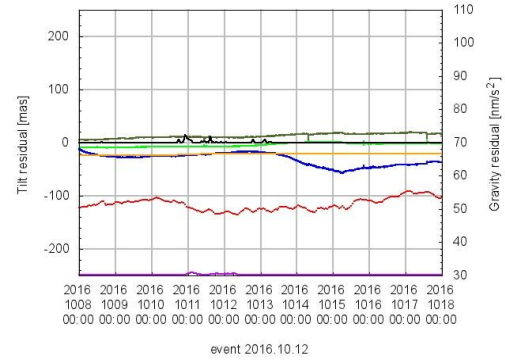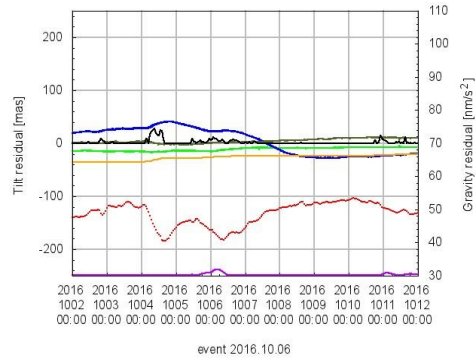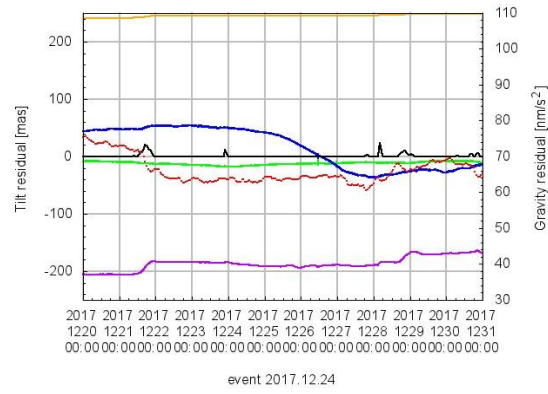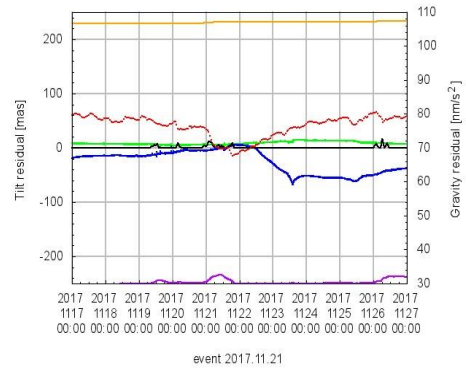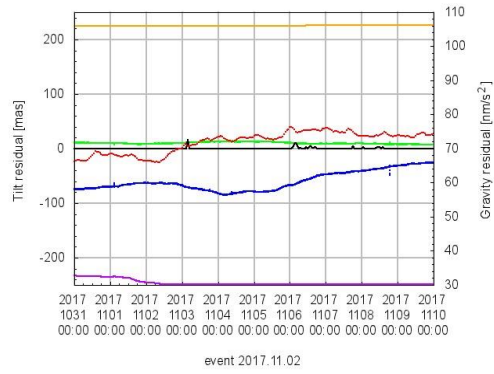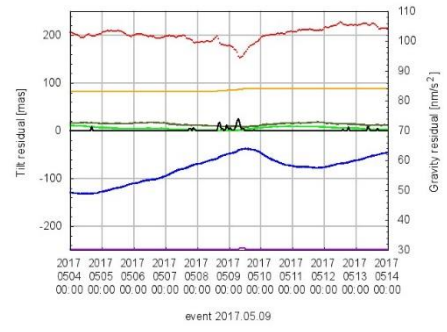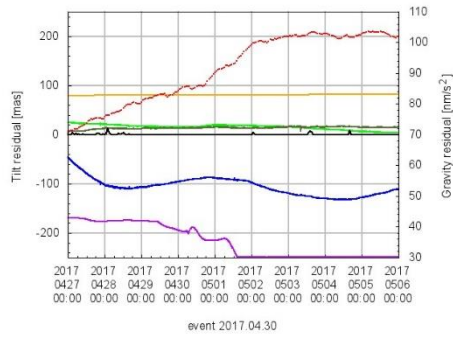
APPENDIX III

Calculation of time shifts for the rain events

Event '2016.06.30'

Event '2016.07.25'

Event '2016.09.06'

Event '2016.10.20'

Event '2017.09.20'

Event '2017.10.27'
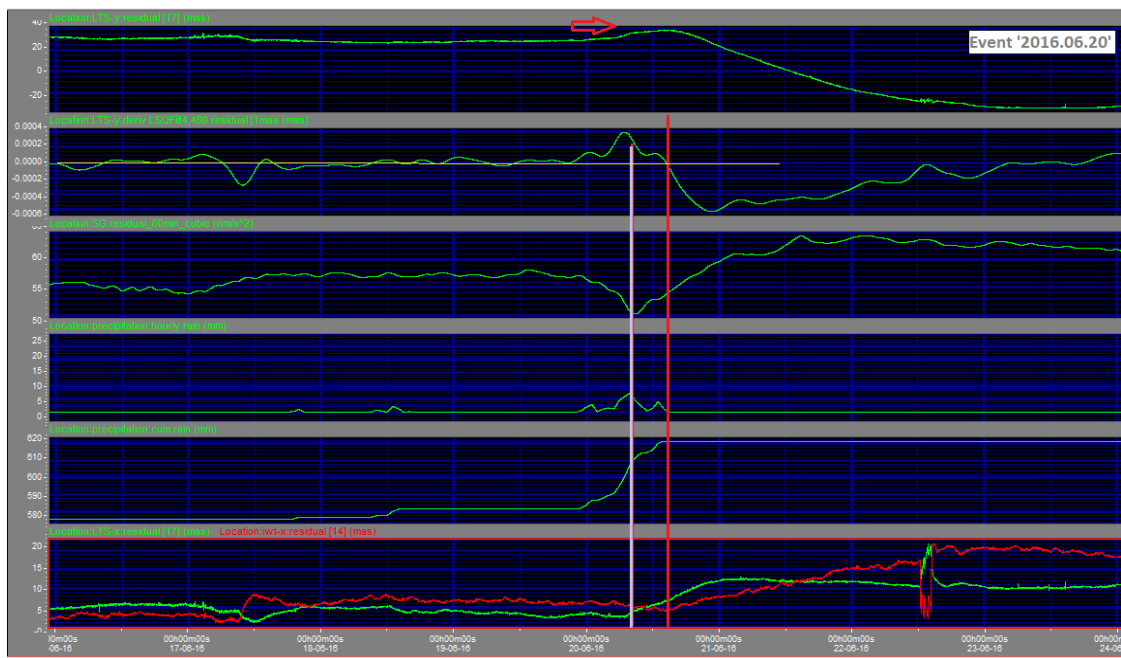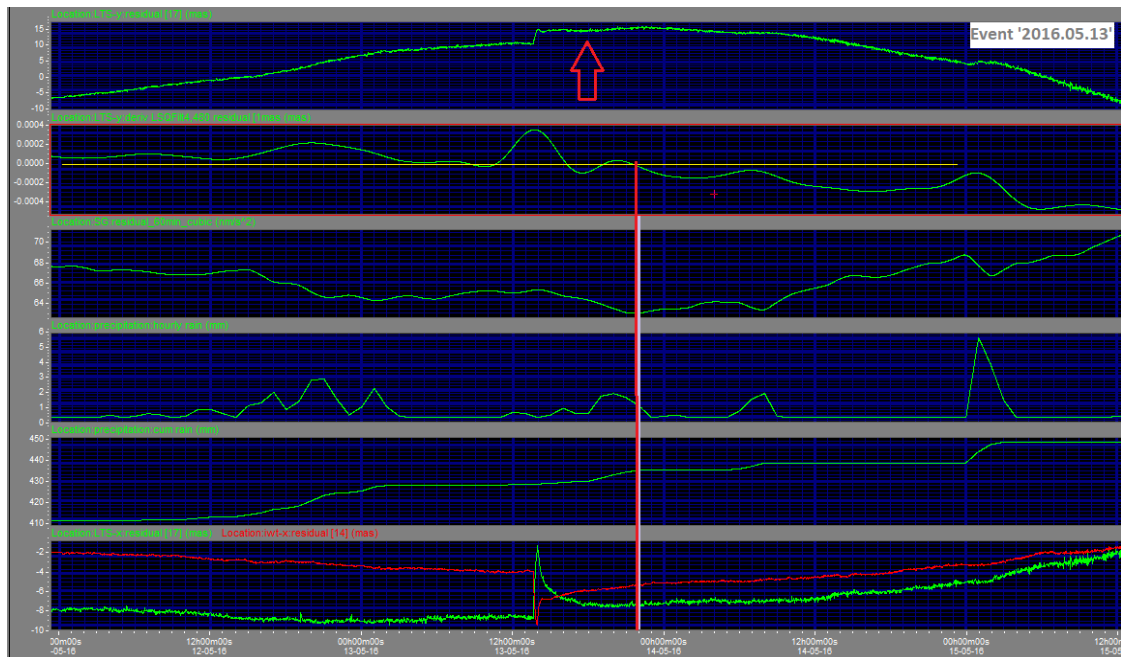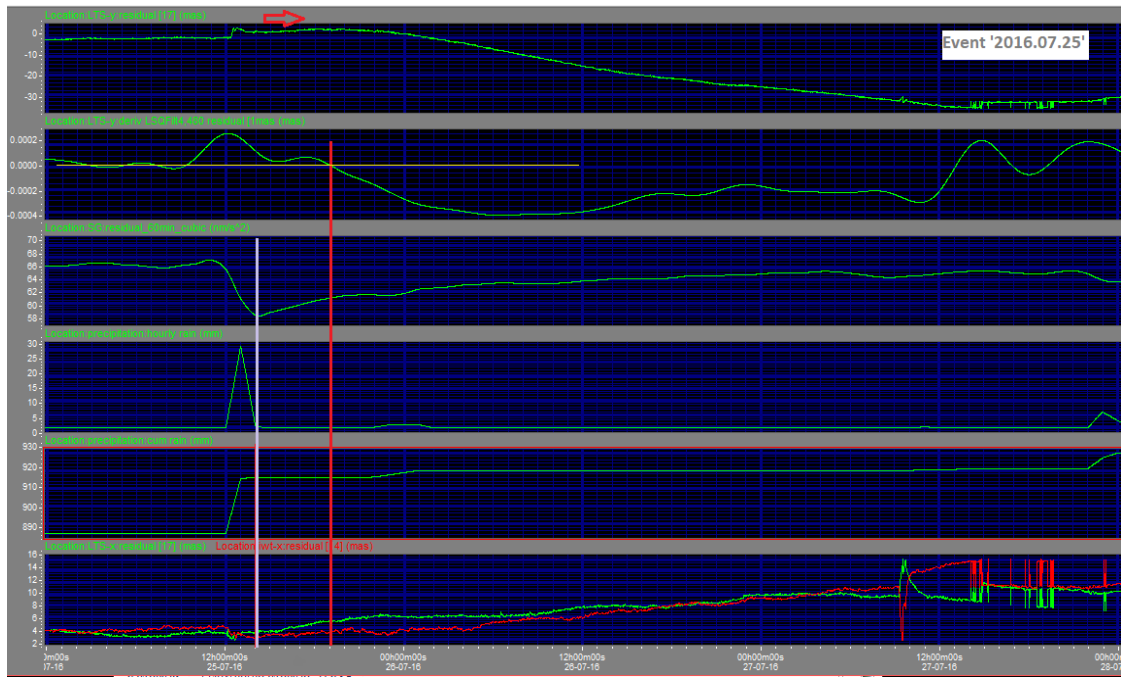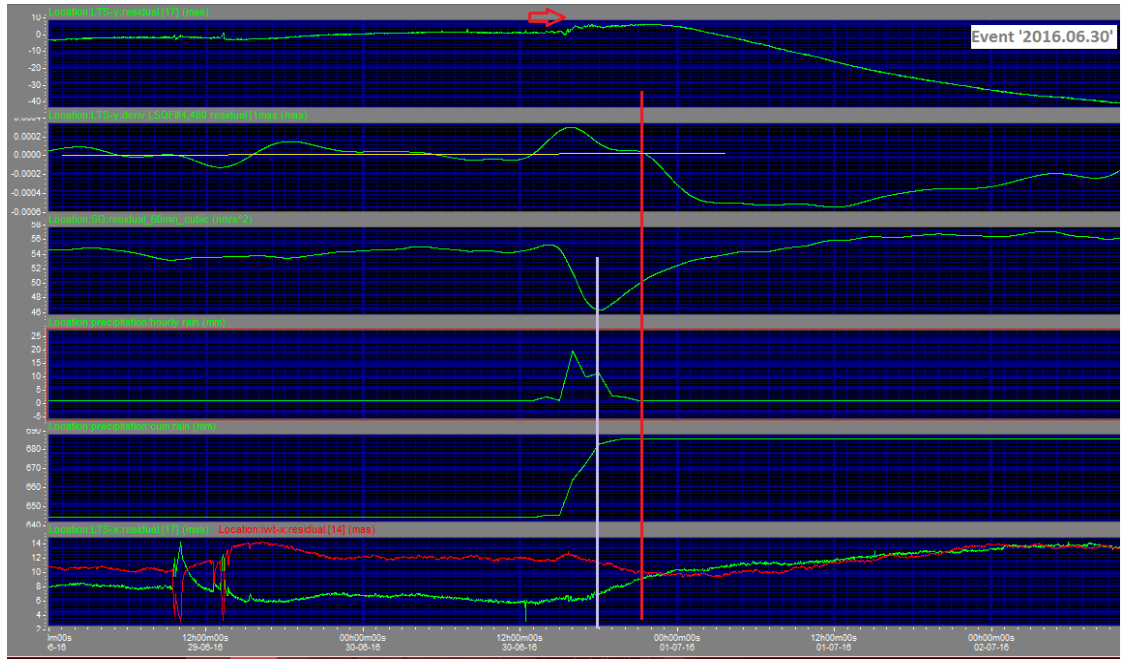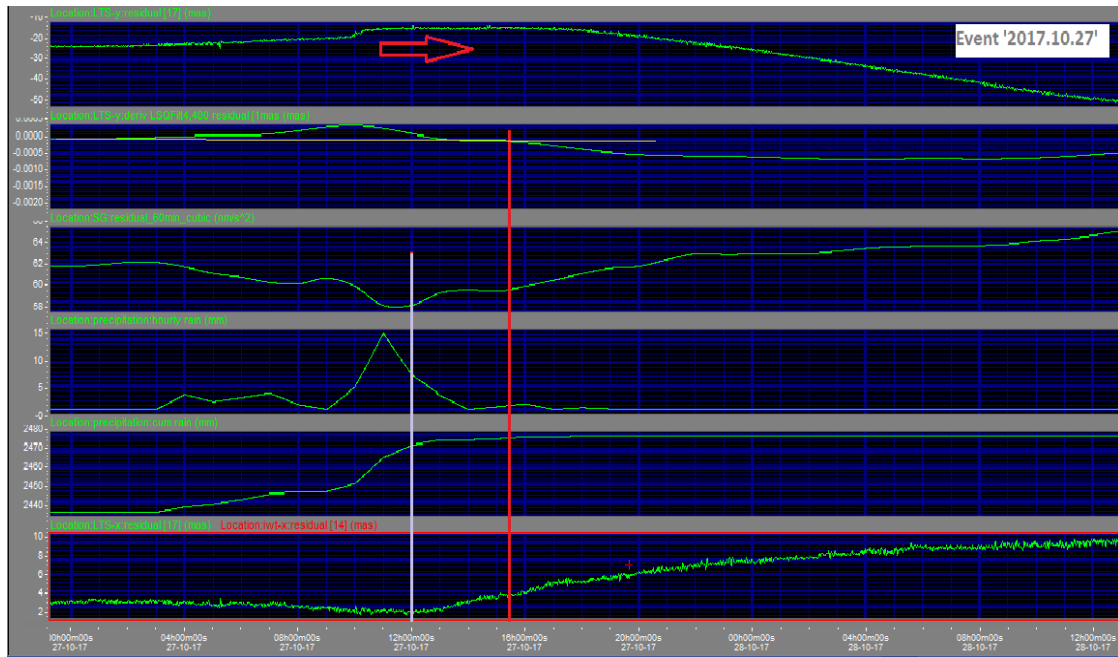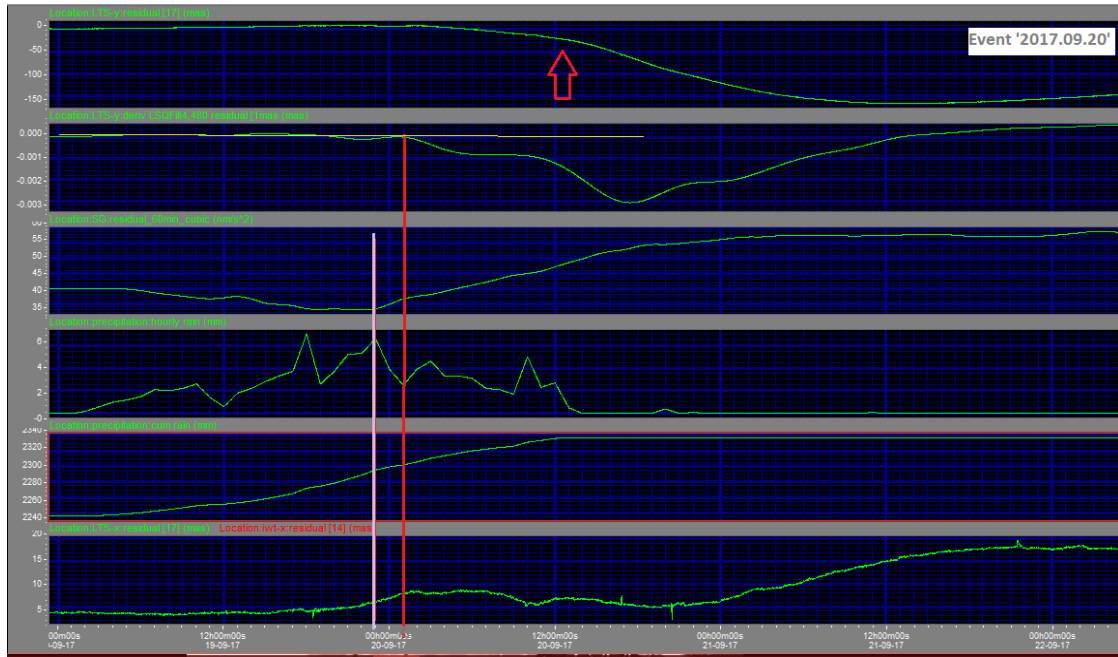
APPENDIX IV

Calculation of time shifts for the mixed events

Event '2016.11.16'

Event '2017.02.21'
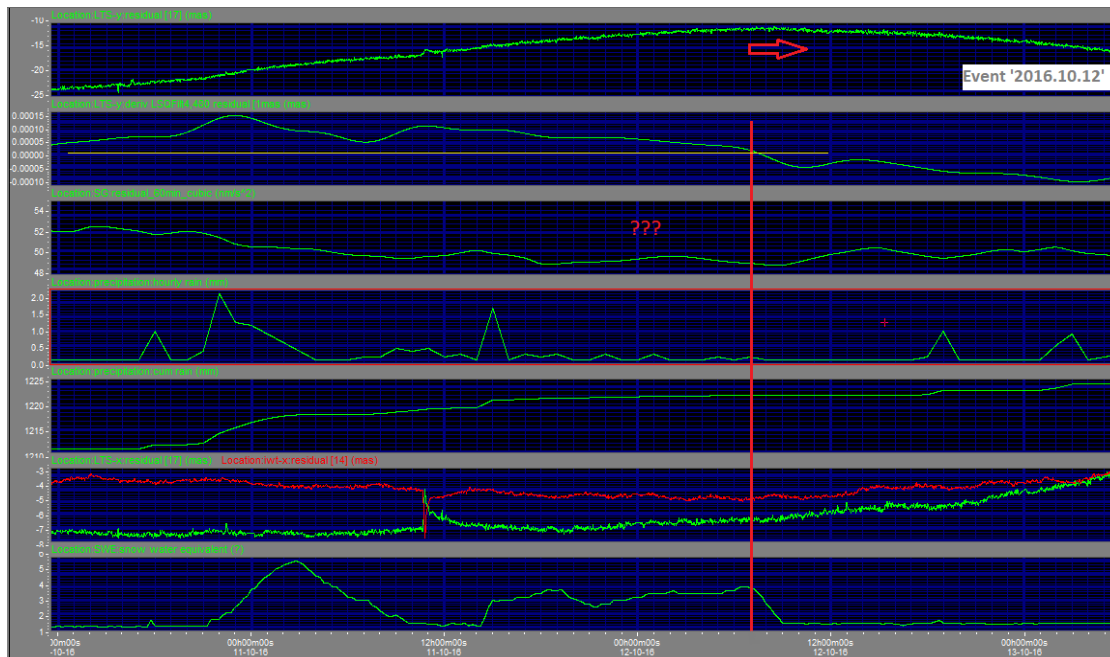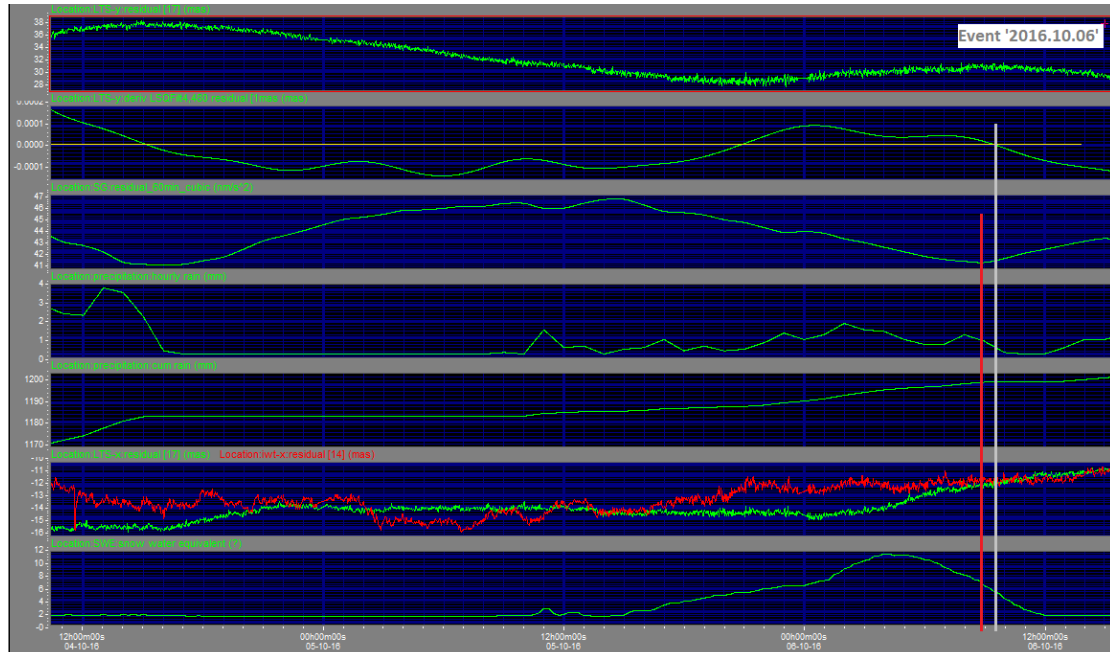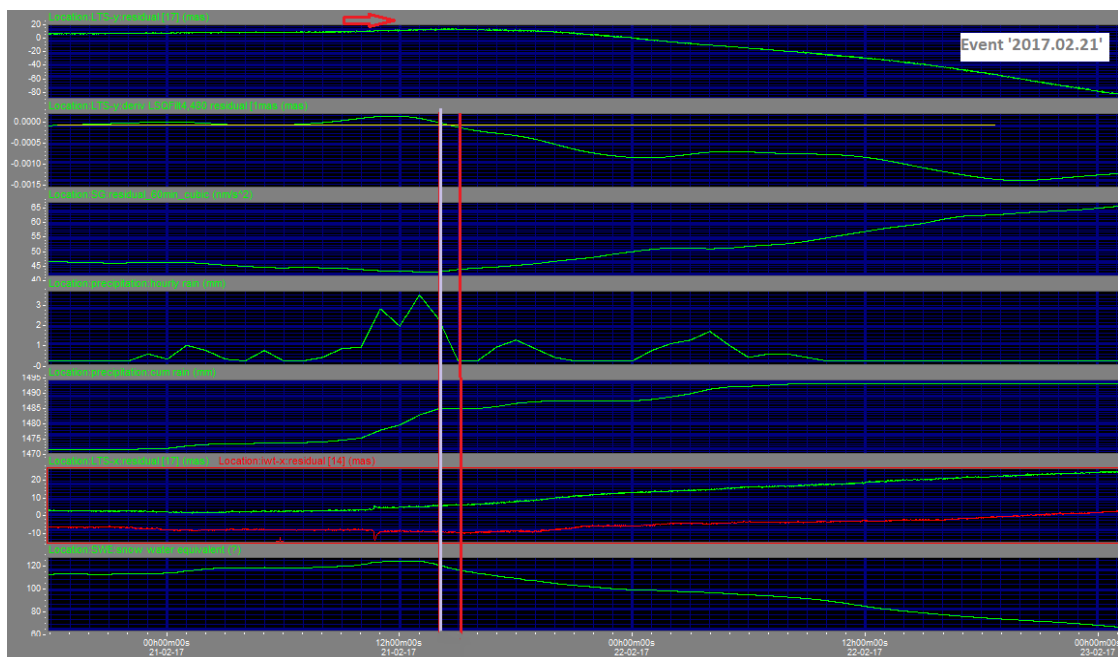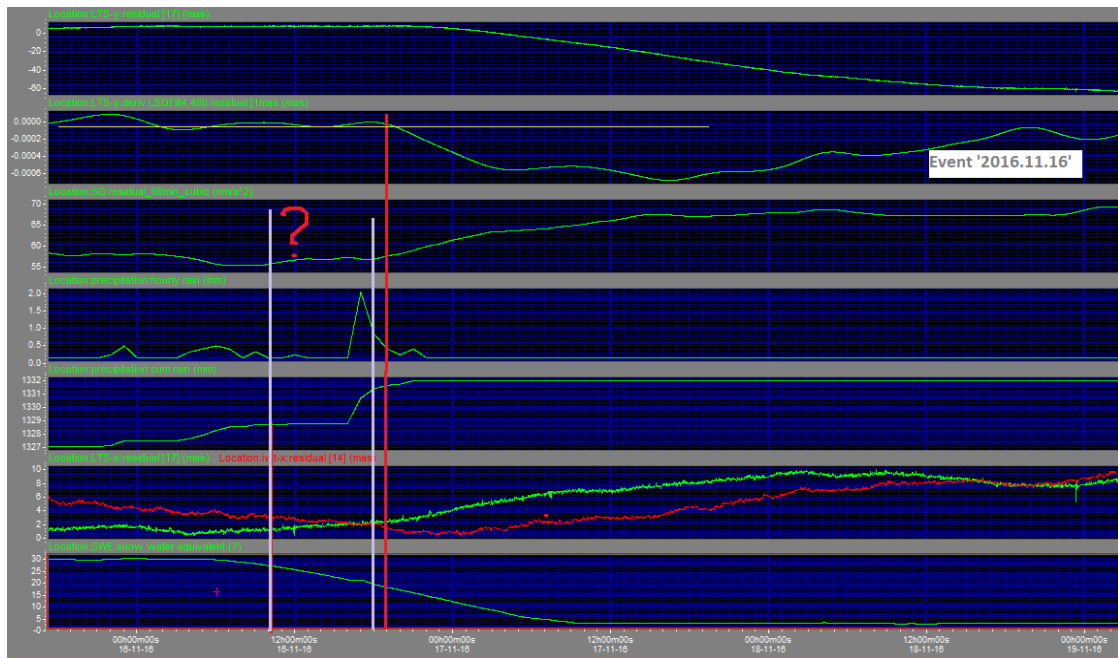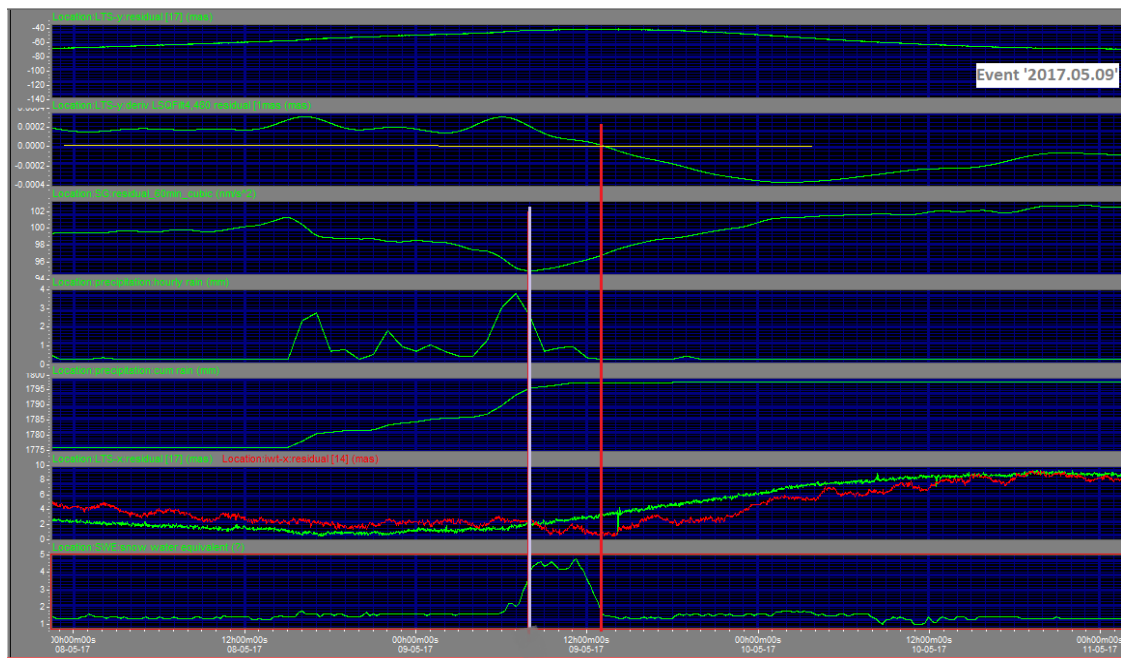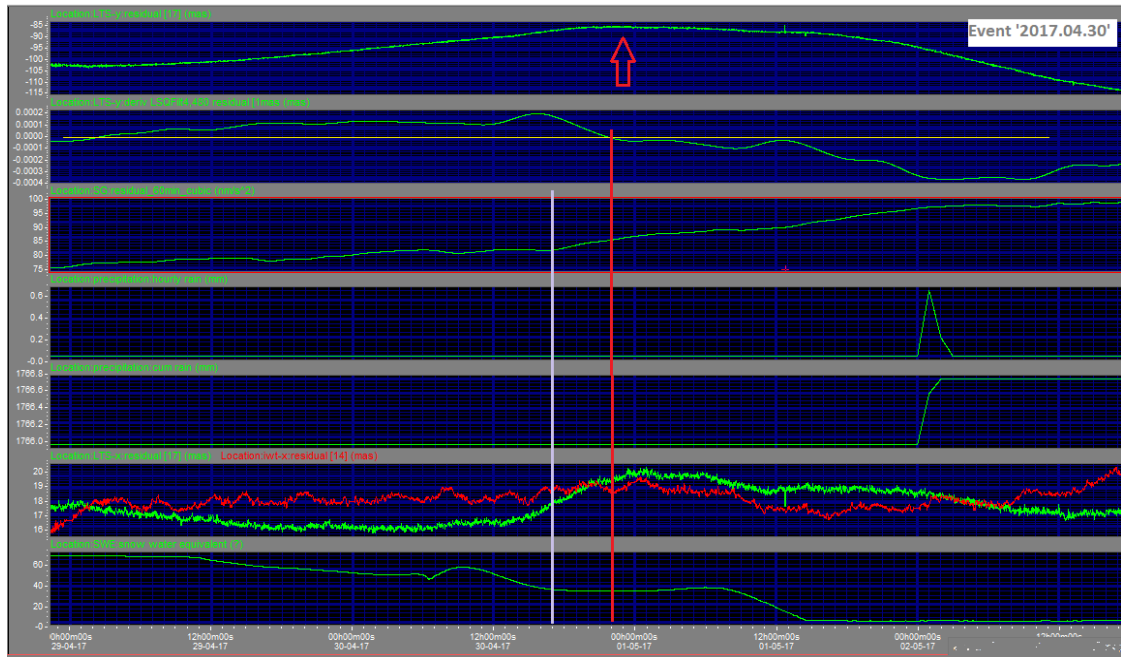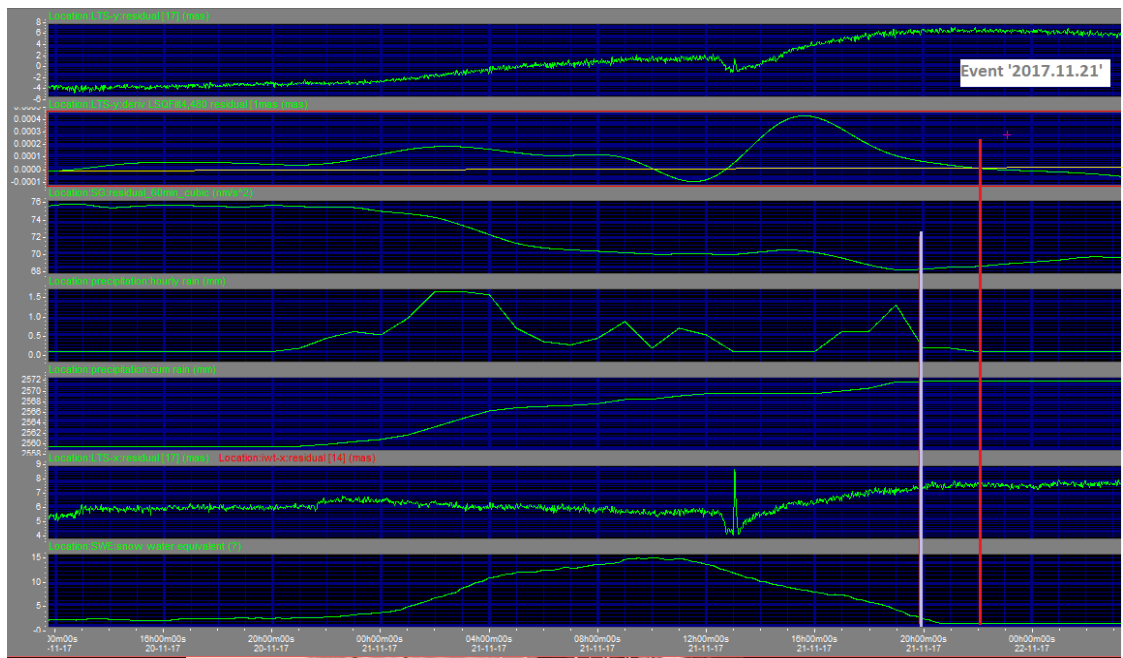
APPENDIX V

Estimation of the total amount of the melted snow water

Event '2016.11.16'

Event '2017.02.21'
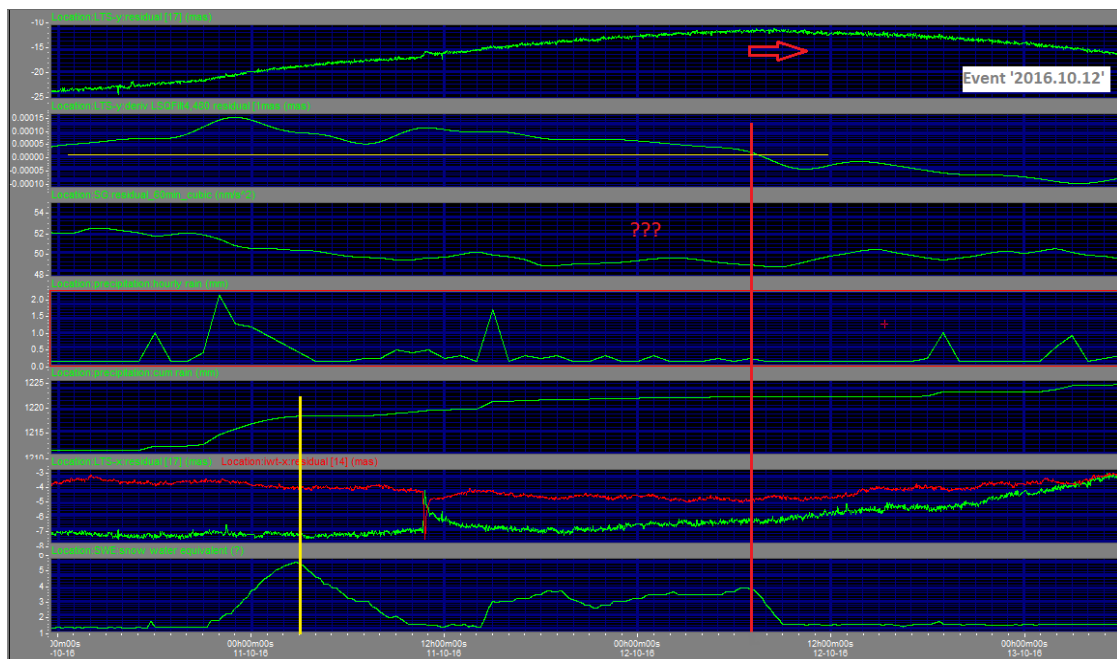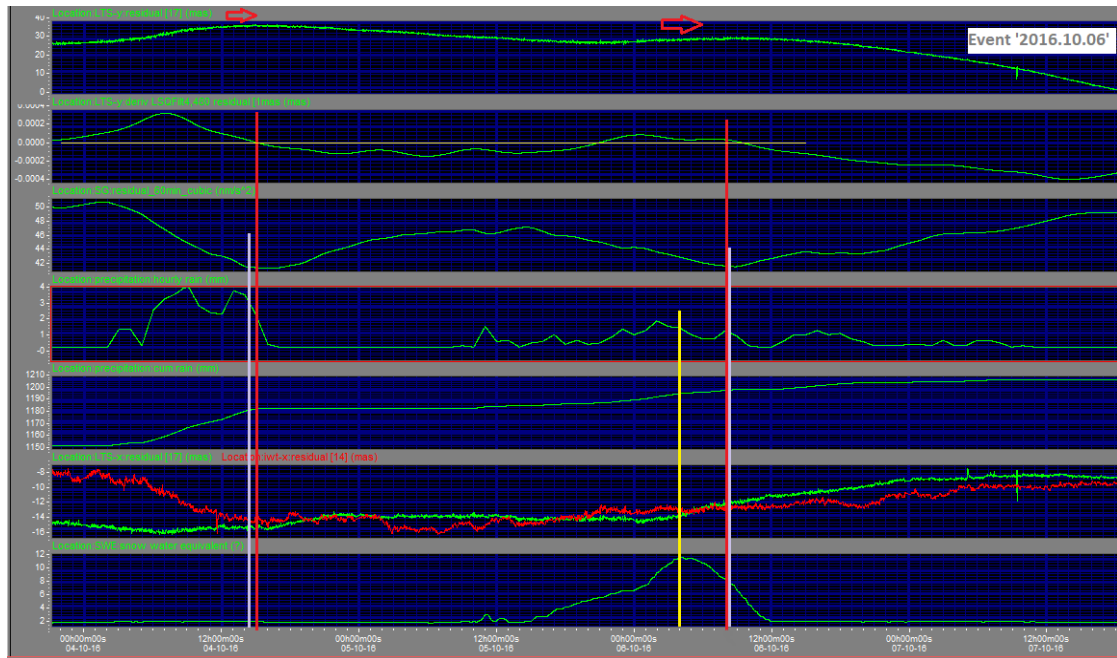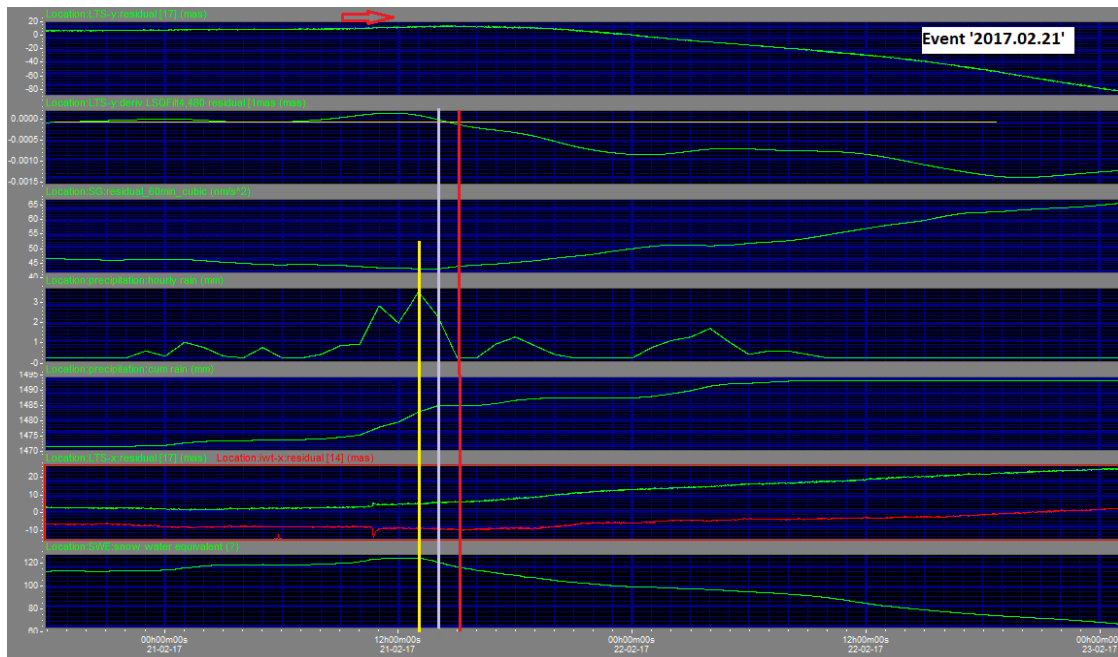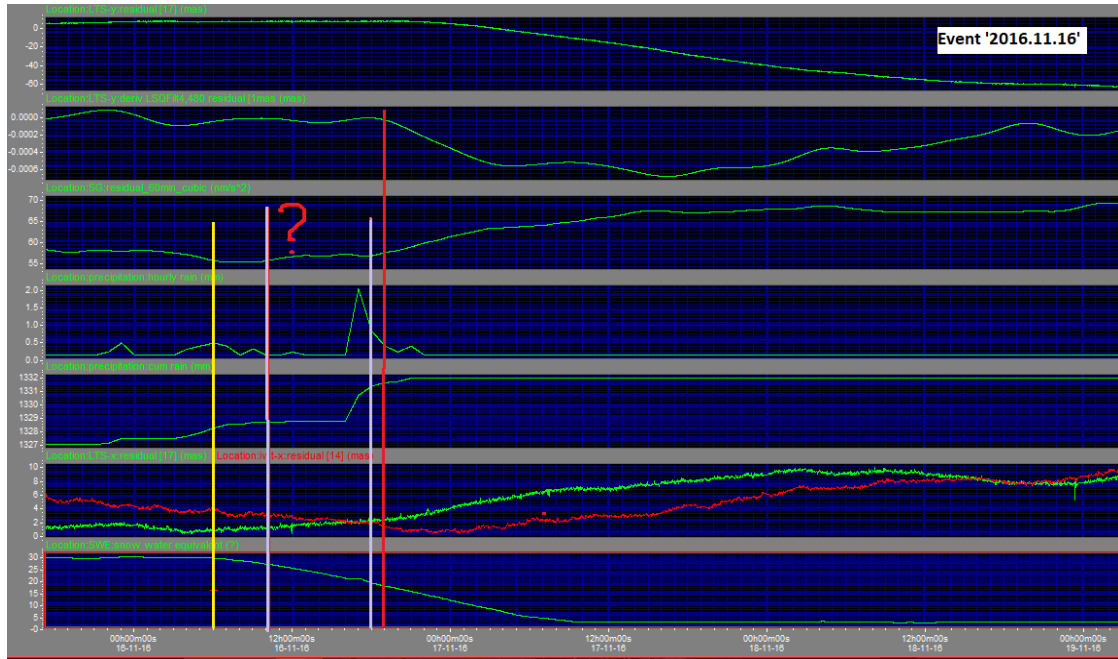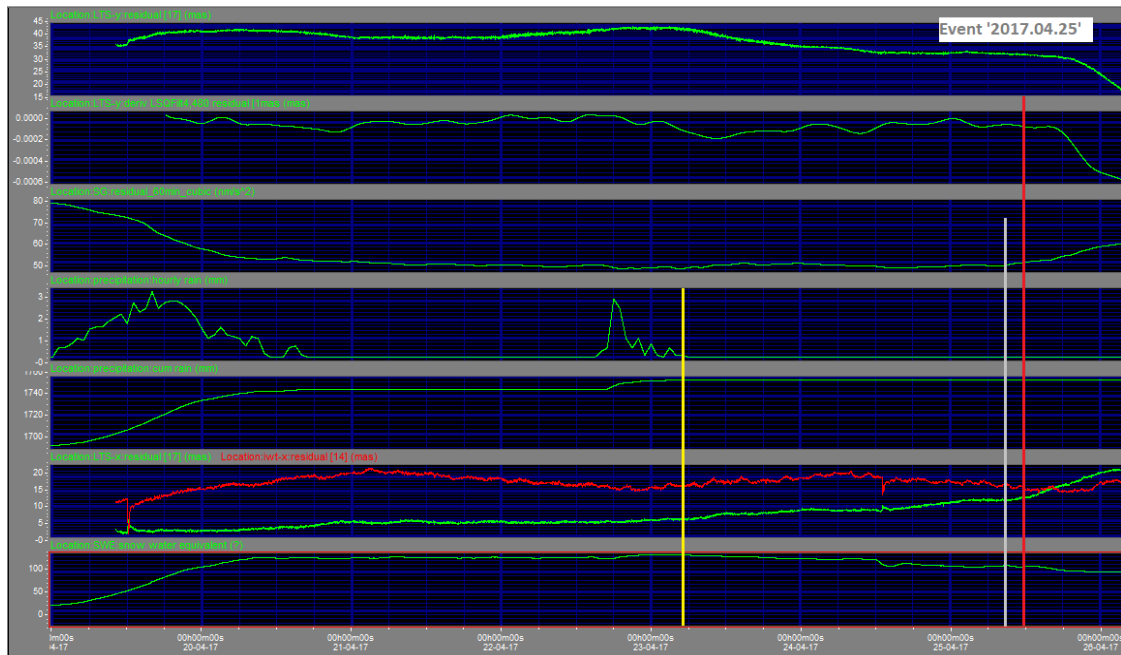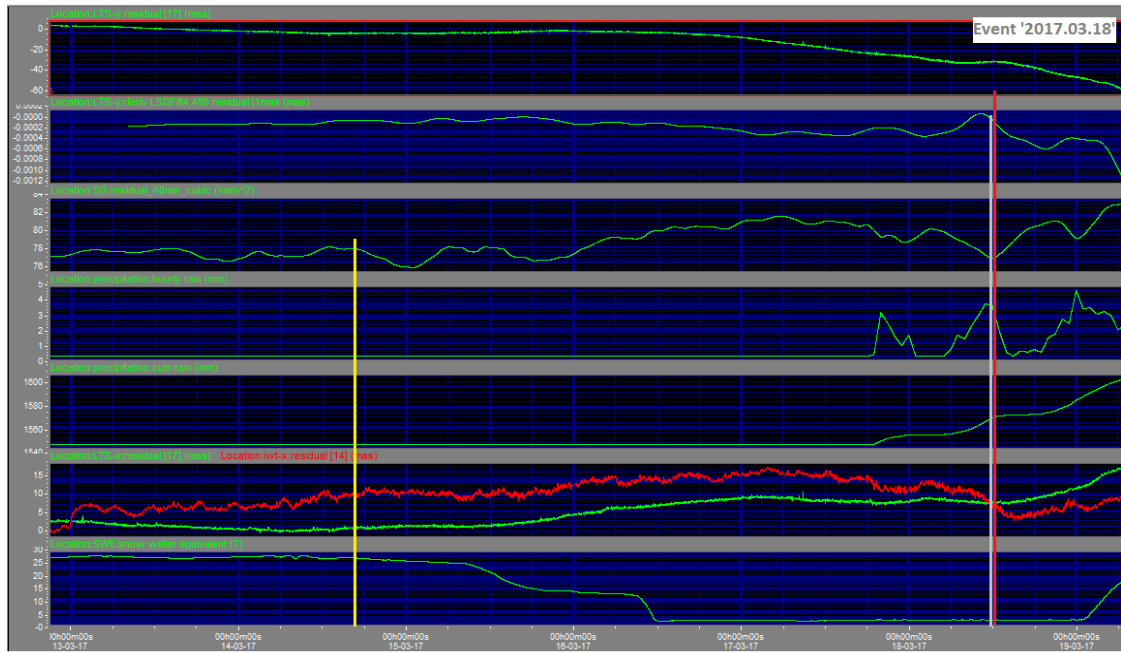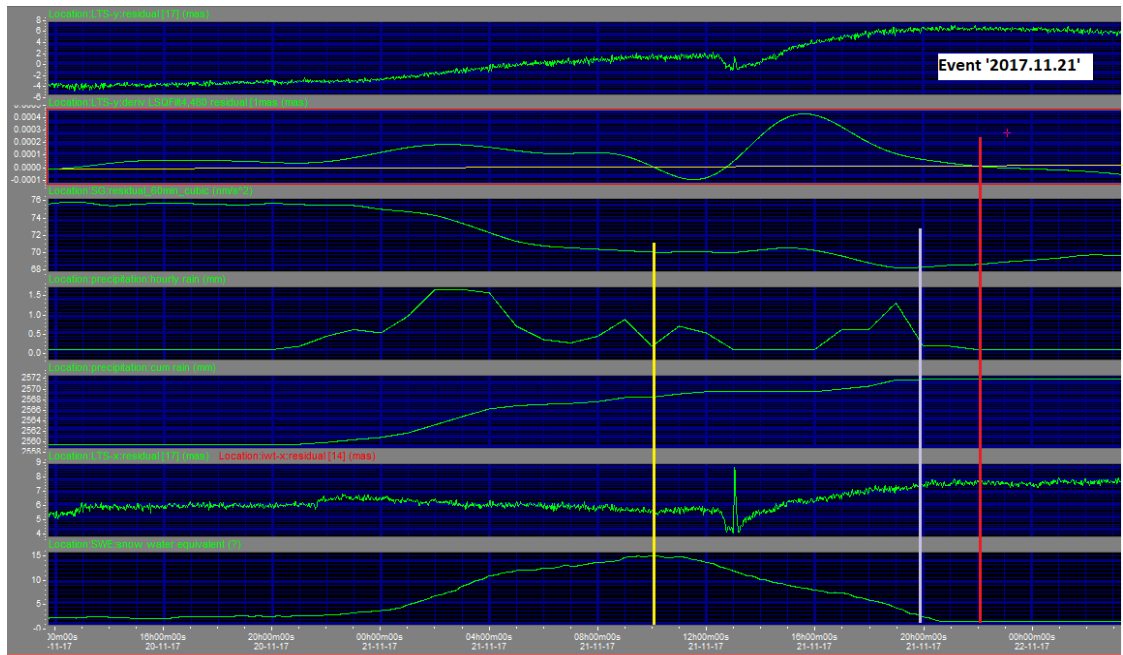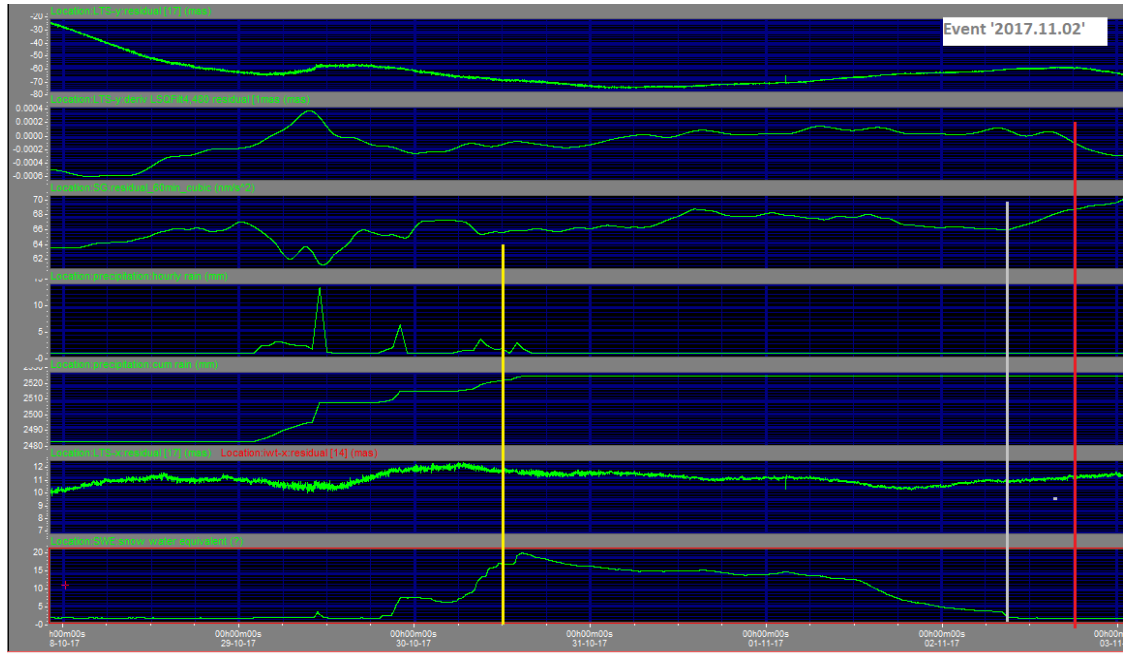
APPENDIX VI

Correlation and t-test

The concept of correlation and t-test is explored further in this appendix in order that the flow of the results is not interrupted in the main text. The correlation is the quantitative description of the 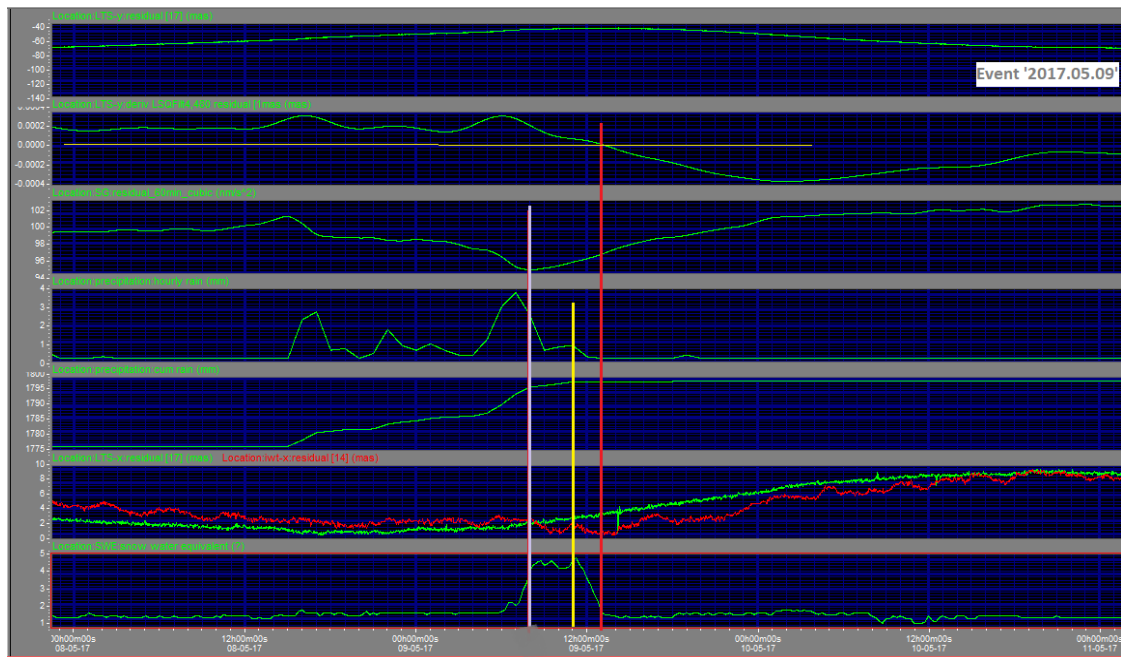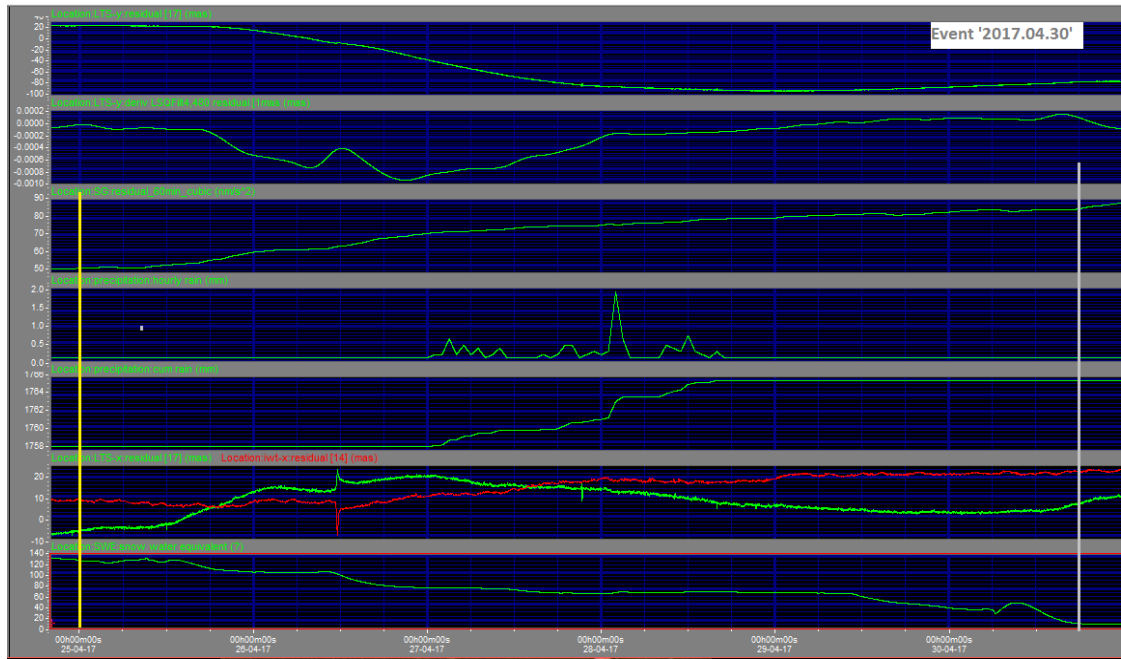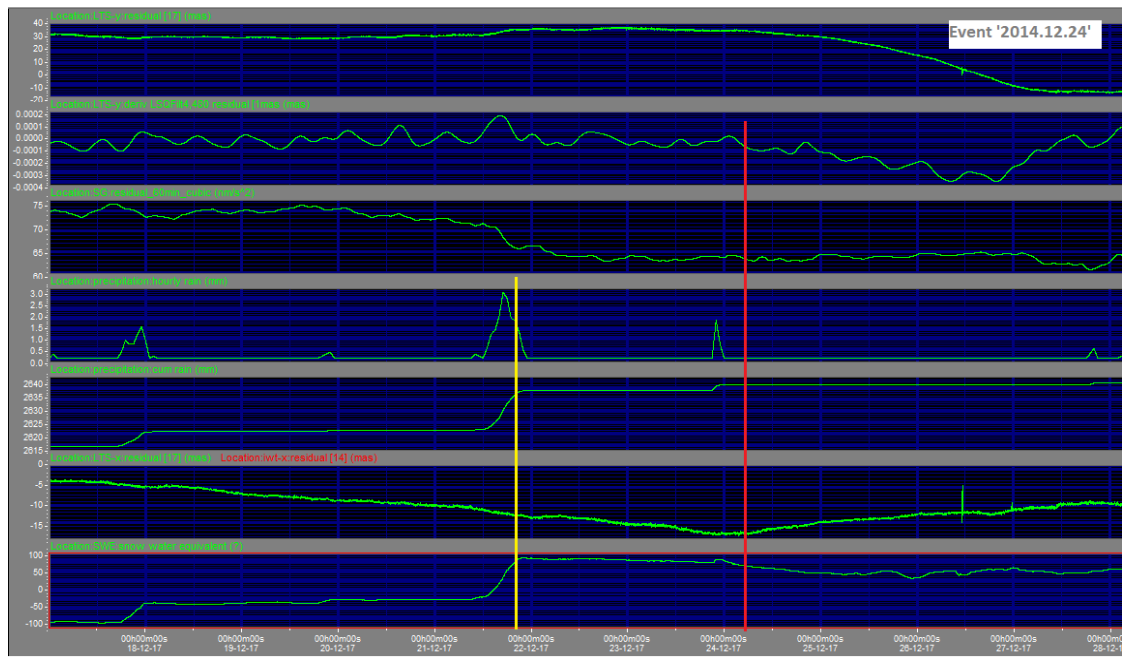relation between two variables. It varies from -1 to 1, which correspond to fully anti-correlated and correlated relation respectively. The value of 0 means no correlation between the variables. The correlation coefficient comes along with the standard error, which is also shown in the tables 3.4, 3.5. For a correlation coefficient r of n-2 degrees of freedom (i.e. n pairs of data minus two) we have:

$$\delta r = SE = \sqrt{\frac{1-r^2}{n-2}} \quad .$$

Having the result $r \pm \delta r$ for a correlation coefficient is not enough in order to make statistical statements. One needs to examine the significance of the result. This is done by performing the so called t-test. The t-test quantifies the answer to the question how confident one can be that the conclusion of the correlation of the two variables (hypothesis H1) is not just a statistical fluctuation and the variables are actually not correlated (null hypothesis H0, $r=0$).

The first step of the t-test is to calculate the statistic t, which is the relative error of the result, i.e.

$$t = \frac{r}{\delta r} = r\sqrt{\frac{n-2}{1-r^2}} \quad .$$

From the above equation it is obvious that the statistic t already includes the statistical information of the sample (with n being the number of the data pairs). Given the degrees of freedom and the statistic t one can calculate the probability P that the outcome is a fluctuation of a non-correlated result. From this point there are two ways to proceed.

A. One can, for a given P (typical choice 0.05) and $d.o.f.= n$-2, get the corresponding critical value T from public shared tables (see table) and compare with the statistic t. If $|t| \geq |T|$, then at a confidence level $CL = (1 - P) * 100$ % (typical choice 95%), the correlation is not a fluctuation of the null hypothesis.

B. **What is done in this thesis:** Instead of looking for the critical value T for a given P one can directly calculate the probability $P_{d.o.f}^{t}$ that corresponds to the actual

statistic t with the specific $d.o.f.$. Similarly to the public shared tables, there are available tools for this calculation online. So for a given pair of values of the statistic t and the $d.o.f$ one can state the confidence level $CL = \left(1 - P_{d.o.f}^t\right) * 100\ \%$, that the specific correlation $r \pm \delta r$ is not a fluctuation.

Since the correlation is sign sensitive rather than a symmetric result, I adopted the one-tailed t-test. If the reader is interested the translation of the results to the two-tailed t-test is trivial $(P_{d.o.f}^t \rightarrow 2P_{d.o.f}^t)$.

t Distribution: Critical Values of t

		Significance level (P)					
Degrees of freedom	*Two-tailed test:* *One-tailed test:*	10% 5%	5% 2.5%	2% 1%	1% 0.5%	0.2% 0.1%	0.1% 0.05%
1		6.314	12.706	31.821	63.657	318.309	636.619
2		2.920	4.303	6.965	9.925	22.327	31.599
3		2.353	3.182	4.541	5.841	10.215	12.924
4		2.132	2.776	3.747	4.604	7.173	8.610
5		2.015	2.571	3.365	4.032	5.893	6.869
6		1.943	2.447	3.143	3.707	5.208	5.959
7		1.894	2.365	2.998	3.499	4.785	5.408
8		1.860	2.306	2.896	3.355	4.501	5.041
9		1.833	2.262	2.821	3.250	4.297	4.781
10		1.812	2.228	2.764	3.169	4.144	4.587
11		1.796	2.201	2.718	3.106	4.025	4.437
12		1.782	2.179	2.681	3.055	3.930	4.318
13		1.771	2.160	2.650	3.012	3.852	4.221
14		1.761	2.145	2.624	2.977	3.787	4.140
15		1.753	2.131	2.602	2.947	3.733	4.073
16		1.746	2.120	2.583	2.921	3.686	4.015
17		1.740	2.110	2.567	2.898	3.646	3.965
18		1.734	2.101	2.552	2.878	3.610	3.922
19		1.729	2.093	2.539	2.861	3.579	3.883
20		1.725	2.086	2.528	2.845	3.552	3.850

APPENDIX VII

The cavity scenario (1)

Estimation of the mass of the possible Cavity from gravimeter						
Input parameters						
Gravity constant			Use of the Delta g of gravimeter			
G =	6,67E-11	m^3*kg^{-1}*s^{-2}		g=	5,00E-08	m*s^{-2}
Formula for the mass estimation						
M =	g*r^2/G		Kg			
Data for plot and plot						

Distance r [m]	Mass M [Kg]
0	0,00E+00
1	7,49E+02
2	3,00E+03
3	6,74E+03
4	1,20E+04
5	1,87E+04
6	2,70E+04
7	3,67E+04
8	4,79E+04
9	6,07E+04
10	7,49E+04
11	9,07E+04
12	1,08E+05
13	1,27E+05
14	1,47E+05
15	1,69E+05
16	1,92E+05
17	2,17E+05
18	2,43E+05
19	2,70E+05
20	3,00E+05
21	3,30E+05
22	3,63E+05
23	3,96E+05
24	4,32E+05
25	4,68E+05
26	5,06E+05
27	5,46E+05
28	5,87E+05
29	6,30E+05
30	6,74E+05

Mass M [Kg] vs distance r [m]

M =	3,00E+05 Kg
rho =	1000 Kg/m^3
Radius of spherical cavity	
R =	4,152011 [m]

The cavity scenario (2)

R-r_LTS for different values of cz, cx - zoomed, f=8

Legend: 1, 2, 3, 4, 5, 6, 7, 8, 9, 10, 11, 12, 13, 14, 15, 16, 17, 18, 19, 20

R-r_LTS for different values of cz, cx - zoomed, f=12

Legend: 1, 2, 3, 4, 5, 6, 7, 8, 9, 10, 11, 12, 13, 14, 15, 16, 17, 18, 19, 20
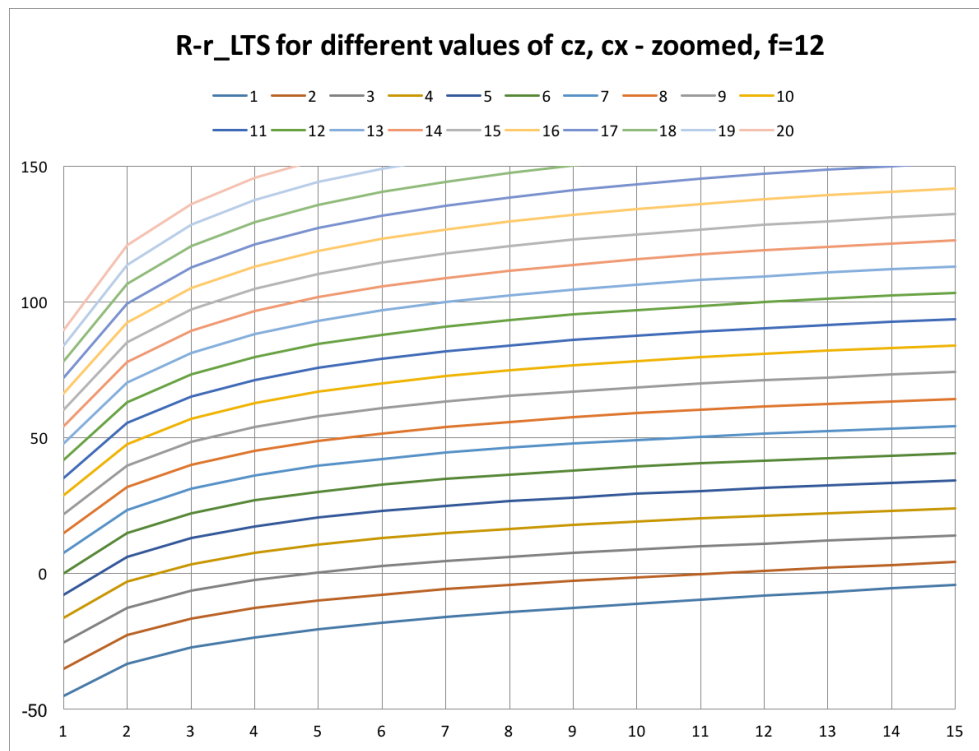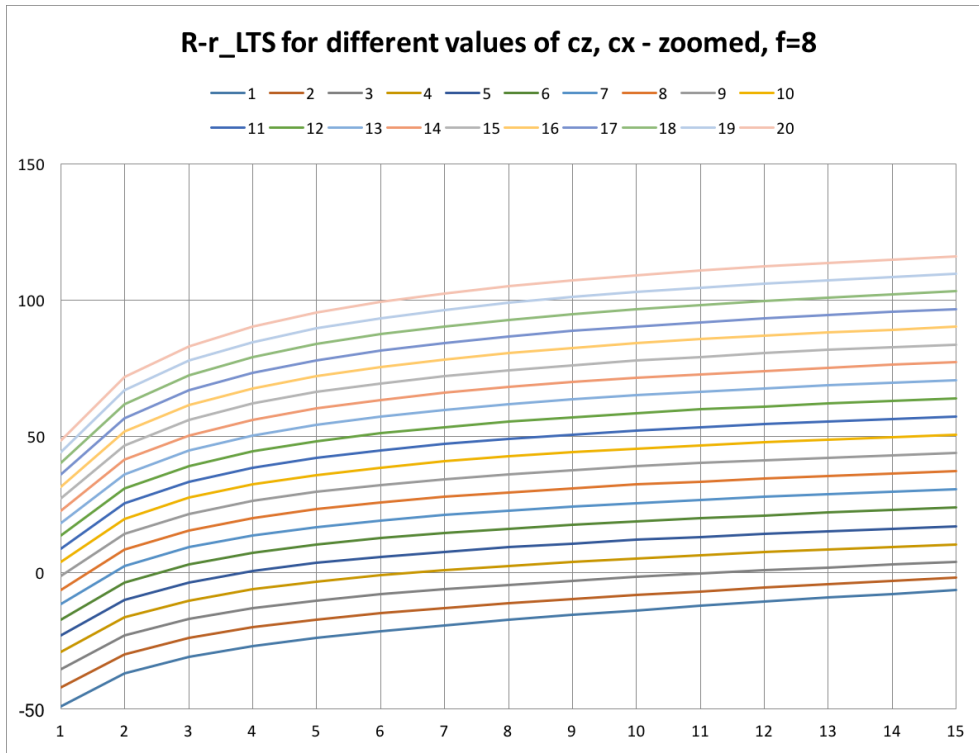
Abstract

Serafeia Mangou: Response of tilt and gravity on environmental processes at Conrad observatory, Austria.
[Master´s thesis]. University of Vienna. Faculty of Earth Sciences, Geography and Astronomy, Department of Meteorology and Geophysics.

Supervisor: Univ.-Prof. Dr. Bruno Meurers Vienna 2019. 89 pgs. Degree of qualification: Master.

We investigate the contribution of the atmospheric and hydrological effects to two tilt meters and a superconducting gravimeter which are operating since April 2016 in the Conrad Observatory, in Austria. Not only the Earth tides but also mass transports can lead to variations of the gravity field of the Earth. While a gravimeter is sensitive only to the Newtonian signal of time variable mass transport, tilt meters are affected by secondary effects as well which can dominate the long-term variations in tilt. Continuous measurements of gravity and tilt, therefore, can provide us with information about a variety of geophysical processes. We need to find a model in order to remove local and global hydrological effects, as long as the local influences are very strong, distort our residuals and prevent us from 'catching' signals of geodynamical significance. In this thesis, the tidal signals will be removed and the residuals will be compared and related to atmospheric and hydrological processes at the site.

Abstrakt

Serafeia Mangou: Signalantwort von Neigung und Schwerkraft auf Umweltprozesse am Conrad-Observatorium, Österreich.

[Master-Arbeit]. Universität Wien. Fakultät für Geowissenschaften, Geographie und Astrnomie, Institut für Meteorologie und Geophysik.

Betreuer: Univ.-Prof. Dr. Bruno Meurers, Wien 2019. 89 Stn. Qualifikationsgrad: Master.

Wir untersuchen den Beitrag der atmosphärischen und hydrologischen Effekte auf zwei Neigungsmesser, die seit April 2016 im Conrad-Observatorium in Austria in Betrieb sind, und einem supraleitenden Gravimeter. Nicht nur die Erdgezeiten, sondern auch Massentransporte können zu Variationen des Gravitationsfeldes der Erde führen. Während ein Gravimeter für das Newtonsche Signal des zeitvariablen Massentransports empfindlich ist, werden Neigungsmesser auch durch Sekundäreffekte beeinflusst, die die langfristigen Neigungsschwankungen dominieren können. Kontinuierliche Messungen von Schwerkraft und Neigung können uns daher Informationen über eine Vielzahl geophysikalischer Prozesse liefern. Eine Korrektur lokaler und globaler hydrologischer Effekte ist notwendig, solange lokale Einflüsse sehr stark sind, die Residuen verzerren und so die Separation geodynamischer Signale erschweren. In dieser Masterarbeit werden die von Gezeitensignalen befreiten Zeitreihen verglichen und mit atmosphärischen und hydrologischen Prozessen am Standort in Verbindung gebracht.

CURRICULUM VITAE

Personal information

Date of birth:	23.03.1990
Address:	Schwendergasse 59/3, 1150 Wien
Mobile:	004368110883907
E-mail:	a01576980@unet.univie.ac.at

Education

2016 -

Comenius University in Bratislava

Faculty of Mathematics, Physics and Informatics

University of Vienna

Branch of study: Joint Master Study Programme

Physics of the Earth, degree: MSc.

2007 - 2013

Aristotle University of Thessaloniki, Greece

Department of Physics

Branch of study: Physics, degree: Metapt.